University of Alberta

Development of an Efficient Quasi-3D Microfluidic Flow Model and Fabrication and Characterization of an All-PDMS Opto-Microfluidic Flow Cytometer

by

Md Zahurul Islam

A thesis submitted to the Faculty of Graduate Studies and Research
in partial fulfillment of the requirements for the degree of

Doctor of Philosophy

in

Microsystems and Nanodevices

Department of Electrical and Computer Engineering

To

My parents

My wife and two sons

and

The late Professor James Neil McMullin

Abstract

In this thesis, development of a novel microfluidic flow model, and, fabrication and testing of microfluidic cytometer for potential cell detection and sorting applications are described. The model is formulated by decomposing the flow profile along the height of microfluidic device into a Fourier series that converts the 3D flow equations into a series of coupled 2D equations and is applicable to planar microfluidic devices only. It is validated against the analytical solution for flow in a straight rectangular channel and the full 3D solution of a commercial Navier-Stokes solver for flow in a T-channel. Comparable accuracy to the full 3D numerical solution is achieved by using only three Fourier terms with significant decrease in computation time. The model is also extended to the problems with time-varying boundary conditions.

We fabricated two first generation miniaturized cytometer prototypes and used them for preliminary proof-of-concepts experiments. They were built by cutting fluidic channels into two different polymer materials and bonding them between two standard glass slides with epoxy and fusion bonding.

We fabricated a second generation of flow cytometer chip consisting of an integrated 2D hydrodynamic focusing system, solid-core optical waveguides and a hydrodynamic side-flow switching system on an all-PDMS platform.

Optical propagation losses of the integrated waveguides and signal-to-noise ratio (SNR) of its detection system were characterized. The propagation

losses were found to be 1.6 and 1.5 dB/cm for the green and red light, respectively. Detection of fluorescent signal through the waveguide yielded improved SNR than the conventional method of under-chip detection.

Fluid flow speeds were estimated from volumetric flow measurements and fluorescent particle tracking experiments and the width of the hydrodynamically focused stream was extracted from microscope flow images. The results were compared to the simulation values obtained from the Q3D model and reasonable agreement was observed. Detection and sorting of microparticles were demonstrated using this device and initial results are presented.

The numerical model, the fabrication techniques, and the experimental methods developed in this thesis may be applied to many biomedical engineering applications that use devices utilizing microfluidic flow and optical interrogation.

Acknowledgement

Table of Contents

List of Tables

List of Figures

List of Symbols, Abbreviations and Nomenclature

1D	One-dimensional
2D	Two-dimensional
3D	Three-dimensional
α	Aspect ratio of microchannel
CCD	Charge-coupled device
CFD	Computational fluid dynamics
cm	centimeter
CNC	Computer numeric controlled
CW	Continuous wave
^oC	Degree Celsius
dB	Decibel
DI	De-ionized
DNA	Deoxyribonucleic acid
DRIE	Deep reactive ion etching
E. coli	*Escherichia coli*
FACS	Fluorescence-activated cell sorting
FDM	Finite difference method
FDTD	Finite difference time domain
FEM	Finite element method
FVM	Finite volume method
FWHM	Full width at half maximum
h	hour
h, H	Channel height
He-Ne	Helium-Neon
HIV	Human immunodeficiency virus
ICP	Inductively coupled plasma
ID	Internal diameter
KHz	Kilohertz
L	Characteristic channel length

LED	Light emitting diode
LIF	Laser induced fluorescence
LOC	Lab-on-a-chip
LOD	Limit of detection
μ	Fluid dynamic viscosity
μm	Micrometer
m	Meter
$mbar$	Millibar
MEMS	Micro-electro-mechanical system
MFCS	Microfluidic control system
mm	Millimeter
ms	millisecond
mW	milliWatt
NA	Numerical aperture
NIR	Near-infra red
nm	Nanometer
P	Fluid pressure
Pa	Pascal
PC	Personal computer
PCB	Printed circuit board
PCR	Polymerase chain reaction
PD	Photodiode
PDE	Partial differential equation
PDMS	Polydimethylsiloxane
PEA	Polyepoxyacrylate
PMMA	poly methyl methacrylate
PMT	Photomultiplier tube
Q3D	Quasi-three-dimensional
ρ	Fluid mass density
RBC	Red blood cells
RIE	Reactive ion etching
RMS	Root mean square

RNA	Ribonucleic acid
s	Second
SBR	Signal-to-baseline ratio
SEM	Scanning electron microscope
SNR	Signal-to-noise ratio
t	time
u, v, w	Fluid velocity component
u_A	Analytical velocity
u_{Q3D}	Q3D velocity
UV	Ultra-violet
V	Volt
$\mathbf{V}$	Fluid velocity vector
VSEL SC	Very small embryonic-like stem cell
w, W	Channel width
WBC	White blood cells

Chapter 1

Introduction

1.1 Introduction

Lab-on-a-chip (LOC) systems employing microfluidics have been drawing tremendous interest of researchers over the past decade due to an increasing number of potential applications in many areas, including but not limited to, chemistry, biology, environment and biomedical diagnosis and analyses [[1] [2] [3] [4] [5] [6] [7] [8] [9] [10] [11] [12] [13] [14]]. An LOC system can be thought of as a miniaturized chemical or biological laboratory that integrates many functions (e.g. sample preparation, sample transportation, particle focusing, detection and sorting) typically performed in analytical laboratories. LOC systems offer many advantages beyond conventional biochemical and clinical laboratories, such as reduced sample and reagent volumes, system cost, size and power requirements, possibility of point-of-care diagnostics and disposable use, etc. Most importantly, miniaturization drastically improves analysis characteristics

(e.g., shorter analysis time and higher separation performance) and even achieves innovative applications that are not achievable otherwise. Within the last ten years, a dramatic increase in research activities into these devices has taken place and microfluidics remains a 'hot' research topic. While important technological progress has been made in materials, fabrication and fluid handling and diagnostic methods, advances in microfluidics modeling are not as dramatic. A theoretical understanding of microfluidic flow is essential for predicting the behavior of flows inside chips and to optimize chip design. However, unlike the microelectronics chip design, a number of issues associated with the numerical modeling and simulation of microfluidic system still prevent it from being employed as an effective tool for LOC design.

One application for LOC is flow cytometry. Flow cytometry is a kind of cytometry in which counting, examining and sorting of cells or microscopic particles suspended in a stream of fluid are carried out. They are routinely used in clinical settings for everything from simple blood counts to the monitoring of HIV patients. They are also used in biological labs for cellomics and in different biochemical industries for determining the content of micro-particles, e.g. bacteria. In a typical flow cytometer, cells or micro-particles are arranged to flow sequentially through a monochromatic incident light beam in a sensing region and some characteristic parameters of the samples, for example, scattered light and fluorescence property, are measured to provide information about the cells or particles of interest [15]. Advances in the field of micro-electro-mechanical

2

systems in recent years have made it much more plausible to develop a micro-flow cytometer with all the advantages that an LOC system can offer in addition to those achievable through a bench-top cytometer. So currently, researchers are looking to miniaturize the flow cytometer to a smaller scale in order to reduce the capital and operational cost and to make it a portable one for fast point-of-care diagnostic.

Although there is enormous potential for LOC technologies, its promise in delivering the low-cost, low-volume and application-specific integrated systems has not yet been fulfilled, primarily because of the technical difficulties in the integration of all the functional blocks in a single chip and the lack of an efficient computer simulator that can be used to optimize the design before it actually goes for fabrication. This issue becomes even more acute for large scale integration and automation of microfluidics which is considered the trend for the next generation of LOC systems.

Currently two approaches are mainly used for the realization of a microfluidic chip or any other chip containing microfluidic elements in it. They are: experimental approach and numerical approach. In the experimental approach, the designer starts with rough conceptual schematic of the design and uses fundamental equations to ensure the design feasibility. This rough design is then sent for fabrication. Because no prior verification of functionalities is carried out by computer simulation, this approach often results in non-functional chips.

Any errors detected during the characterization of the fabricated chip are used to redesign the chip. Thus, this design methodology is based on a fabrication-design-fabrication loop, which is extremely expensive and time-consuming. In the second approach the design is first verified through numerical simulation and then sent to for fabrication. This simulation-based verification results in a much cheaper and effective iterative simulation-design loop. However, a number of serious issues associated with the numerical simulation of microfluidics still prevent it from being applied with ease. The most serious issue of numerical approach arises from its very high demand of computational overhead, e.g., memory requirements, CPU time and expertise. As this approach solves the discretized transport equations, fine meshes and time steps and expert knowledge of numerical algorithms are necessary to ensure the solution convergence and accuracy. For complex three-dimensional (3D) flow geometries and systems, numerical finite difference, finite volume and finite element methods have been used for many years [16] [17], and a number of commercial software packages are currently available. However, these packages are designed to handle general and arbitrary boundary conditions and therefore require extensive computing resources and time for solving realistic problems. Due to small computational cell sizes, they are typically used to model the flow in limited regions of a complicated structure but are not suited to larger scale problems. This restriction may be alleviated by using two-dimensional (2D) simulations but these ignore important effects, such as drag caused by the upper and lower walls of the channels, which may significantly affect the solution.

Considering all these limitations and constraints of the currently available numerical approaches, we are motivated to develop a quasi-3D numerical model of microfluidic devices which are fabricated using planar fabrication technology, which is practically the technology followed by almost all the microfabrication foundry. In developing this new numerical method we must address the following needs of the future generations of the LOC devices: high-speed simulation and adequate accuracy.

1.2   Motivation

In recent years, stem cells have been recognized as potentially very important for medical research [18]. They are building blocks for tissues and bones. They play an important role in regenerative medicine. One of the stem cell types, very small embryonic like (VSEL) stem cells, is present (apart from bone marrow) in cord blood and mobilized peripheral blood (mobilization is the forced migration of stem cells from bone marrow to peripheral blood [19]) in very low concentration along with the white blood cells (WBCs), red blood cells (RBCs) and platelets [20] [21]. WBCs and RBCs in principle can be removed from the blood by centrifugation but a recent study [22] indicates that could lead to considerable loss (about 60%) of VSEL stem cells. The current methods [22] [23] [24] [25] to isolate the very rare VSEL Stem cells from bloods require the use of many expensive fluorescent markers and thus the procedures are very expensive and time consuming. It is known that the light scattering of a biological cell, and also of a micro-particle, is a complex function of its size, shape and structure, as well

5

as their refractive index and absorption of its constituents. For example, scattering patterns of human blood cells and cell lines have been studied both numerically and experimentally, and have demonstrated dependence on the internal structure of cells and distribution of internal organelles [26] [27] [28] [29]. Thus the scattering pattern of each cell can be very distinct and can be used as a fingerprint to identify a cell or to determine a cell condition. For example, it was shown that the side-scattered light intensity from a VSEL stem cell is approximately an order of magnitude higher than that of a platelet cell [30]. This property can be exploited to differentiate stem cells from platelets so that they can be separated from each other. Our goal is to develop a low cost micro-flow cytometer fabricated using the microfabrication technologies for label-free/labeled enrichment/sorting of VSEL stem cells from cord blood samples. As alternative application areas, sorting or detection of very rare circulating tumor cells in the early stage of breast cancer [31] or other types of cancers, very low pathogen concentration for water quality monitoring [32], etc. can be performed by using fluorescent tags with the developed micro-flow cytometer.

1.3   Goals of the PhD thesis

In general terms, the foci of my PhD research work presented here are two fold: development of a computationally efficient (resource, time and accuracy) numerical quasi-three-dimensional (Q3D) microfluidics model for microfluidic devices fabricated using planar microfabrication topology (almost all of the microfluidic devices fall into this category), and, development and evaluation of

an opto-microfluidic chip for flow cytometric application, e.g., detection and sorting of micro-particles/biological cells. We have selected this particular application because of its current importance to the scientific and clinical communities and its suitability for the experimental verification of our numerical model as it requires fluidic manipulation of very small amount of samples. The main premise in these investigations is that the inherent advantages associated with numerical modeling and microfabrication technologies such as photolithographic patterning, PDMS technology and built-in alignment, and bulk anisotropic etching of the substrate, can be exploited to predict the behaviour and increase the capabilities of this type of instrumentation.

More specifically, the thesis will explore the following points:

1. Development of an efficient numerical model of laminar flows in planar microfluidic devices
2. Design, fabrication and characterization of an all-PDMS opto-microfluidic device for flow cytometric applications (detection and sorting of biological cells/micro-particles)
3. Proof-of-concept of the numerical model and the micro-flow cytometer

The Q3D numerical model for microfluidic devices developed in my PhD thesis is valid only for the devices fabricated using planar fabrication topology that results in the flow channels with reasonably rectangular cross-section. Also the model is valid for laminar flows and incompressible fluids only, which are

7

normally valid for LOC system. The model is implemented for pressure driven flow only.

1.4   Thesis Outline

As stated earlier, this thesis has two foci. One is the development and verification of an efficient numerical model of laminar flows in planar microfluidic devices. And the second is the fabrication and characterization of an all-PDMS opto-microfluidic flow cytometer for cell sorting applications. The motivation, goals and the project scope are presented here in this very first introductory chapter. An overview of the background/state-of-the-art of this project is presented in Chapter 2. The mathematical formulation and numerical verification of the planar microfluidic flow model is presented in Chapter 3. Chapter 4 describes the details of miniaturized flow cytometer prototyping and experimentation with them. The details of design and fabrication of a state-of-the-art micro-flow cell sorter are presented in Chapter 5. The optical characterization of the microfabricated cell sorter chip is presented in Chapter 6. Chapter 7 presents the characterization of the flow, sample focusing and sorting characteristics of the chip. This chapter also describes the comparison of the experimental results with the planar microfluidic flow model and simplified circuit model. Finally in Chapter 8, a summary of this thesis is presented and future work has been suggested.

Chapter 2

Literature Review

2.1. Introduction

As mentioned in chapter 1 our ultimate goal is to develop a low cost miniature micro-flow cytometer which is capable of sorting VSEL stem cells from cord blood. The complete understanding of the micro-flow cytometry requires the knowledge on the subjects of micro-flow dynamics, photonics, microfabrication, optics, electronics etc. One of the major steps in realizing a cytometry system is the design and optimization of the components that make up the whole system. A complete understanding of the microfluidic transport mechanism is necessary to understand and design the channel network of the microfluidic chip that controls the sample activity. As mentioned in the introductory chapter, some characteristic parameters of the samples (micro-particle/biological cells), e.g. scattered light and/or fluorescence property, are used to identify the micro-particles or cells of interest. The light scattering of a biological cell, and also of a micro-particle, is a

complex function of its size, shape and structure, as well as the refractive index and absorption of its constituents. The relative contributions of these parameters to the total scattering depend on the relative direction of observation with reference to the incident light, i.e. their contributions vary with the scattering angle. The study of light scattering off cells/micro-particles has itself grown to a big field of research. Among all the related disciplines of studies of micro-cytometry, microfabrication, which is the actual tool for the realization of the chip/device, has become one of the hottest topics in the recent years. Thus, for systematic review of micro-flow cytometry, I have divided it into a number of subgroups that have individually emerged as very important fields of research. These are the following: (1) theoretical microfluidics, (2) fluorescent labelling and light scattering characterization of blood cells, (3) microfabrication and integrated opto-microfluidic chips and (4) micro-particle/cell sorting. The state-of-the-art research in these areas is reviewed below.

2.2. Theoretical microfluidics

Fluid flows in the micron and submicron size range have viscous forces dominate over inertial forces. These micro-flows typically have small Reynolds numbers [33]. For the optimization of the design of a microfluidic chip, a theoretical study of the flow behavior inside the chip is essential. Some of the very good reference books that can help build the basics of theoretical microfluidics are texts from H. Bruss (2008) [34], D. Li (2004) [35] and Tabeling (2005) [36]. Navier-Stokes equations are typically used to model fluid flows. Although the Navier-Stokes

equations are simplified at this low Reynolds number regime, an analytical solution for general flow channel structures is still not available. So, for a complete understanding of flow behaviour in these channels one must resort to numerical solutions of the simplified Navier-Stoke's equations. However, a complete 3D numerical analysis is still very expensive, both in terms of computational resources and time requirements.

Most of the microfluidic systems use one of two mechanisms of fluid transport: pressure-driven flow and electrokinetically-driven flow. Electrokinetic flow refers to the combination of electroosmotic and electrophoretic flow. In this thesis, pressure-driven flow was chosen to generate the fluid flow in the chip.

Most work on microfluidic systems incorporates fluid mechanics modeling as a design tool or as a way to interpret experimental results. However, there are very few cases in which the geometries are simple enough that analytic expressions for the velocity field can be obtained. Even in the case of a straight rectangular channel, the solution can only be expressed as an infinite series. So, early researchers in this field used simplified geometries and simple analytical models well-known from macroscopic fluid mechanics [37] [38] [39] [40].

There are simplified methods for simulating a chip-scale fluid network. One such method is to use the similarity between hydraulic resistance in a channel and ohmic resistance in a branch of an electrical network and to carry out the analysis with an electrical simulation tool such as PSPICE [41] [42] [43]. This

technique is termed as Electrical Circuit Equivalency Model of Microfluidics. In this approach, pressure replaces voltage and volume flow replaces current. The main limitation of this simplified flow model is that it does not provide the details of the velocity field as a function of the position in the channels but only the approximate average flow rates through the channels. There are many microfluidic applications (e.g. micro-mixer, microfluidic drug discovery platform and flow focusing in cell sorter) that require the knowledge of details flow profile as a function of position in the channels for the betterment of the design of the channel network. Also parameterizing the channel dimensions and geometries in the simulation process can provide optimized design results for chips for many microfluidic applications. But parameterizing the channel geometries is very difficult, if not impossible, in this simplified microfluidic circuit model, as the calculation of resistances is complicated, if not impossible, for general flow structures.

Prior to the work presented in this thesis, the detailed numerical simulation of microfluidic systems using finite difference method (FDM), or finite volume method (FVM), or finite element method (FEM) was the only available way to obtain accurate solutions. For complex three-dimensional (3D) flow geometries and systems, these methods have been used for many years [16] [44] [17], and a number of commercial software packages based on these methods are currently available to the LOC design community. They include COMSOL [45] [46], CoventorWare [47], Fluent [48], ANSYS [49] and CFD-ACE+ [50] [51]. In these

commercial packages, a user first generally needs to construct the geometric model of the microfluidic device and properly mesh the geometry, then, set up appropriate physics model, boundary and initial conditions. Finally the resultant system of equations is solved by using direct or iterative solver. However, these packages are designed to handle general and arbitrary boundary conditions and therefore require extensive computing resources and time for solving realistic problems. Due to small computational cell sizes, they are typically used to model the flow in limited regions of a complicated structure but are not well suited for larger scale problems. This restriction may be alleviated by using two-dimensional (2D) simulations but these ignore important effects, such as drag caused by the upper and lower walls of the channels, which may significantly affect the solution.

In this thesis, we have presented an efficient quasi 3D microfluidic model for laminar flows which can be used for the design optimization of chip-scale fluid network. It provides the complete velocity and pressure profiles as a function of the position in the channels much faster so that the model can be run repeatedly by parameterizing it to obtain the optimized values for the critical design parameters (e.g, channel dimensions, geometries and working pressure/velocity values).

2.3. Optical identification of blood cells

2.3.1. Fluorescent labelling of blood cells

Fluorescent labelling is generally used in the life sciences as a way of tracking or analysing biological molecules or cells by means of fluorescence emission. Currently, blood cells are identified and isolated using mainly the flow cytometric technologies including fluorescence-activated cell sorting. The very small embryonic-like stem cells (VSEL SCs) are not an exception. Moreover, as VSEL SCs are found in a very small concentration along with other blood cells and as none of them can be isolated efficiently by centrifugation, identification and isolation of VSEL SCs requiring many fluorescent markers. For example, in a recent publication the isolation protocol [22] the researchers used required 12 markers to isolate VSEL SCs from umbilical cord blood samples.

2.3.1 Light scattering patterns of blood cells

Light scattering pattern can potentially be used as a fingerprint for the identification of a blood cell. Our research group has measured and numerically simulated light scattering pattern from several blood cells and cell lines including Lymphoid Raji cells [26], platelets and hematopoietic stem progenitor cells (CD34+) [27]. There are also some results reported by other groups. Lu et al. [52] carried out numerical simulations of light scattering by a biconcave shaped human

red blood cell (RBC) using the FDTD method. They have presented the numerical results for the angular distributions of the light scattering of an RBC and their dependence on shape, orientation, and wavelength. They have suggested that enhanced back scattering from RBCs of biconcave shapes can be used as a sensitive tool to measure changes in RBC shape. Ost et al. [53] experimentally differentiated erythrocytes and leukocytes in dilute whole-blood samples by observing forward and orthogonal light scatter at 413.1 nm, corresponding to the absorption maximum of oxy-hemoglobin. They also quantitatively determined the wavelength dependence of the integrated differential scattering cross section of spherical erythrocytes.

2.4 Microfabrication and integrated opto-microfluidic devices

The discovery of photolithography for microfabrication in the 1960's gave researchers a different perspective for building small things [54]. The microfabrication technologies developed for the microelectronics industry have also been applied for various other fields including chemistry, biology, medicine etc. for the miniaturization of bulk and complex instruments to reap benefits such as, reduced sample and reagent volumes, system cost, size and power requirements, possibilities of point-of-care diagnostics and disposable use, innovative applications that are not possible otherwise. As stated before, these technologies have also been utilized for miniaturization of flow cytometry.

15

However, precise fabrication is required to establish optimal fluid flow in flow cytometry, where cells are hydro-dynamically focused into a single-line stream. The additional advantages of using microfabrication to realize a flow cytometer include the ability to create desired channel structures rapidly and inexpensively, and to obtain optimized channel geometries that are difficult to fabricate using conventional glass machining techniques. Using Micro-electro-mechanical system (MEMS) technology and integrating the necessary parts of a flow cytometer on to a biochip, the device footprints and fabrication costs can all be reduced. The integration of optics and microfluidic device (Opto-microfluidics) is a typical example [55] [56]. It helps to use more compact optics and volume-efficient on-chip sample detection through integration of optical components in close proximity to the fluidic system. Besides the integration of optics and other components in microfluidic devices, the use of polydimethylsiloxane (PDMS) allows rapid prototyping for lower fabrication cost, and the concept of the disposable biochips [57] [58]. PDMS has many favourable properties including transparency in the UV–visible (230 nm to 700 nm) and selected bands of near-IR, and is thus suitable for the fabrication of waveguides and optical elements. It is also easy to fabricate, has a relatively low production cost, is bio-compatible and has elastomeric mechanical properties that provide flexible and watertight interconnects [59] [60] [61] [62] [63] [64] [65] [66]. These properties make it ideal for microfluidic applications [67].

The LOC technologies are currently undergoing a transition from concept to realization requiring many refinements. There are opportunities to improve the performance of the whole system by improving the function of individual components. Some issues still need to be resolved, e.g. channel blockage, leakage, device contamination, flow anomalies and changing surface properties. However, a number of LOC devices have already been developed and are available commercially. The BioMEMS-768 by GenoMEMS and Agilent Technologies' 2100 BioAnalyzer perform electrophoretic separation of protein, DNA, or RNA. CelTor Biosystems developed the CytoChip system which is a drug analysis platform that simulates a precise biological environment. The PathAlert, from Invitrogen allows detection of infectious agents using PCR and analysis techniques. This device can be used to detect plague, anthrax, small pox, or tularemia pathogens [68].

A number of reviews have been published that compiled the major developments in the LOC fabrication technologies [69] [70] [71] [72]. Some of the important reports related to cytometry are cited below.

Wang et al. [73] reported the development of an innovative micro system, in which several different optical elements, i.e. waveguide, lens and fiber-to-waveguide couplers were integrated with microfluidic channels to form a complete microchip flow cytometer. All the optical elements, the microfluidic system and the fiber-to-waveguide couplers were defined in one layer of polymer

by standard photolithography. They reported successful measurement of scattered light using this microchip.

Yang et al. [74] reported a three-dimensional polymer hydro-focusing micro cell sorter for microfluidic cytometry applications. They demonstrated the hydro-focusing capability of the device with an experiment to sort erythrocytes. Miyake et al. [75] reported a similar multilayered sheath flow chamber that can generate a three-dimensionally focused narrow stream of micro-particles; a three-dimensionally focused stream is surrounded by sheath liquid on all sides, whereas a two-dimensionally focused stream is surrounded by sheath flow on just two sides and contacts the top and bottom channel surfaces.

Lee et al. [76] reported an innovative micromachine-based flow cytometer integrated with buried optical waveguides on soda-lime glass substrates. Experimental results showed that the optical loss is less than 15 dB for a 40 mm long waveguide.

Godin et al. [77] [78] demonstrated the focusing capabilities of a two-dimensional fluid-filled lens microfabricated in an optical polymer. Their functionality for the flow cytometry was also demonstrated.

Jacobson et al. [79] and Schrum et al. [80] studied electro-kinetic focusing of fluids in glass microchips. They achieved focusing of the fluids using electrophoresis, electroosmosis, or a combination of the two.

Medoro et al. [81] reported a lab-on-a-chip device for electronic manipulation and detection of micro-particles based on the use of closed dielectrophoresis cages combined with impedance sensing. They used a PCB prototype to trap, concentrate, and quantify polystyrene micro-beads. They demonstrated the effectiveness of the approach for particle manipulation and detection, without the need for either external optical components or chemical labeling.

Hosseinkhannazar et al. [66] fabricated a polydimethylsiloxane (PDMS) optofluidic biochips with integrated solid-core polyepoxyacrylate (PEA) optical waveguides and experimentally tested the device. Each biochip contained three 70-μm-wide solid-core waveguides focused on the middle section of a 50-μm-wide, Y-shaped, microfluidic channel.

Fu et al. [82] reported a device that incorporated various microfluidic functionalities, including peristaltic pumps, dampers, switch valves, and input and output wells, to perform cell sorting in a coordinated and automated fashion.

In this thesis, we have worked with a microfluidic flow cytometer chip that consists of built-in hydrodynamic flow focusing system, solid-core optical waveguides and hydrodynamic side flow switching in an all-PDMS platform. To our knowledge, this is the first report of a chip implementing all these functionalities in an all-PDMS platform.

2.5 Cell sorting mechanisms

There are many applications in diverse areas of science where distinct characteristics of individual cell or subpopulation of cells is necessary to study many processes where details of cell behaviour and functions provide understanding of biological mechanisms, as opposed to averaging the parameters of an entire cell population. For example, detection, sorting and analysis of cancerous cells, which is very rare in its initial stages, are required to carry out to study them and to find out a remedy for that. There are some reports in oncology for the diagnosis of chromosomal defects and cancers, such as leukemia, lymphoma and breast cancer [83]. As is mentioned before, one of the goals of my PhD research project is to design and build a sorter component as an integral part of the micro-cytometer that can sort cells based on detected signals. Particularly, we are motivated to develop this cell sorter device so that we can utilize it for the sorting/enrichment of the rare very-small-embryonic-like (VSEL) stem cells from cord blood samples. Separation of one type of cells from a mixture of different types of cells (or cell matrix) is a very common challenge. There are some reports of cell sorting in the literature, e.g. *E. Coli* bacteria [82], motile sperm [84] and separation of stem cells from bone marrow matrix [85]. If the concentration of the target cell is extremely low (i.e. rare cells) enrichment is necessary to make analysis more practical. For example, in the early stage of breast cancer, there are only 1 or 2 target circulation tumor cells per 10 billion blood cells, therefore vast removal of red blood cells is required before the target cells can be quantified

[31]. In human cord blood, there are about 5-10 VSEL stem cells per 1 million blood cells. With this rare population of stem cells in cord blood samples, our main objective is to use the sorter, presented in this thesis, for the enrichment of the VSEL stem cells.

Isolation of a particular type of cell/particle from a cell matrix or particle mixture require rapid and precise coordination between different parts of a flow sorter device to selectively control the movement of target samples in a liquid stream. To sort or enrich a particular cell from a cell matrix, a mechanism is required to distinguish the desired cell from the unwanted cells and subsequently another mechanism is required to perform an action to finally increase the concentration in the final sample. In large, bench-top flow cytometry, generally fluorescence-activated cell sorting (FACS) mechanism is implemented. FACS is also generally used for detection of cells in micro-flow cytometer. In our case, the identification of a cell might be achieved by detecting its fluorescent tag, but we also plan to use label-free identification. Our label-free cell identification technique is based on a cell's laser light scattering pattern and/or its laser light scattering intensity. After the cell is identified, it is subsequently sorted to the target collection port. For conventional bench-top flow cytometer, the most commonly used sorting technique is the droplet based sorting. After the flow is hydrodynamically focused, each of the cells is passed through the detection region in single file, interrogated by the laser light and comes out of the nozzle in a separate droplet formed by means of a periodic disturbance from the nozzle. The

droplets with the target cells are charged immediately after they are formed. An electrostatic deflector is used to deflect the droplets with the desired cells towards a target collector vessel. The sorting rate can reach 10,000 cells per second. While the conventional bench-top cytometers have very high throughput they do have some disadvantages including high cost of installation and operation, large size, complexity of the system and operation and the requirement of the large quantity of sample.

Micro-flow cytometers typically have lower throughput than conventional bench-top cytometers but micro-flow cytometers are typically less expensive and are more flexible allowing functionalities to be added for tailor-fitting specific applications and has potential to use in parallel to achieve even more throughput. Current methods commonly used for cell sorting in microfabricated flow cytometer include, mechanical cell trapping (micro-pillar array), magnetic field based sorting, optical tweezers, pinched-flow fractionation, filtering, electric field-based manipulations and separations, acoustic actuation etc. There are many reports of these cell sorting techniques in the literature, and only a selected few of them are reviewed here.

Zhang et al. [86] very recently reported a selective yeast cell trapping method that used microfabricated pillar arrays on PDMS platform to trap the yeast cells. By adjusting the diameter of micro-pillars they could control the number of yeast cells collected on each pillar. Bradley E Layton et al. [87] reported another

microfabricated filter device to sort red blood cells. Some other microfabricated mechanical filters have been described for trapping different cell types from blood [88] [89] [90] [91].

Among the different particle manipulation techniques, electric field based manipulations are very common in microfabricated cell sorters. There are many reports in the literature about this kind of cell sorting technique. There are two types of electric field based cell manipulation techniques: electrophoresis, which is applicable for charged particles (a dc electric field is applied to manipulate the charged particles), and, dieletrophoresis, which is applicable for polarizable (charged or neutral) particles (a non-uniform electric field is applied to manipulate the particles). In microchip cytometers, electrophoresis has been used in many instances to separate microparticles or biological cells and molecules in microchannels [92] [93] [94] [95] [96]. Also, dielectrophoresis has successfully been applied in microchips to manipulate and sort a variety of biological cells including, bacteria, yeast and mammalian cells [97] [98] [99] [100] [101] [102] [103] [104]. Fu et al. [95] presented the fluorescence-activated electrophoretic cell sorting of micro beads and bacterial cells in a microfluidic device. The device consists of three micro channels joined at a T-shaped junction in which an electro osmotic flow of samples advancing through a vertical input channel is diverted to a horizontal waste or collection channel. Fluid flow inside the channel is precisely controlled by voltages applied to inlet, waste and collection ports in a rapid manner. When a fluorescently labeled cell is detected in the input channel, the

23

sample stream flowing from an inlet to a waste port is quickly switched by reversing the electric field to change its flow direction to a collection port. A maximum throughput of 20 cells/s and sorting efficiency of 20% were reported.

A number of research groups have reported sorting of particles based on magnetic and fluorescent activated cell sorting in microfluidic devices. Miltenyi et al. [105] developed and tested a flexible, fast and simple magnetic cell sorting system for separation of large numbers of cells according to specific cell surface markers. The tagged cells are separated on high gradient magnetic columns. Unlabelled cells pass through the column, while labelled cells are retained. Pamme et al. [106] reported the separation of magnetic micropariticles by on-chip free-flow magnetophoresis. In continuous flow, magnetic particles were deflected from the direction of laminar flow by a perpendicular magnetic field depending on their magnetic susceptibility and size and on the flow rate. Magnetic particles could thus be separated from each other and from nonmagnetic materials.

The use of optical force or optical tweezer for controlling live cells was first reported by Askin et al. [107]. After a long break, Wang et al. [108] reported the use of this force to manipulate the direction of live cell flow in a continuous flow situation in a microfluidic device. They have implemented a fluorescence-activated cell sorter and evaluated its performance on live cells using optical force switching. They utilized a high-power near-infra red (NIR) laser to switch the hydro-dynamically focused cells from default waste channel to a collection port.

Throughput of up to 100 cells/s and sorting efficiency of 85% were reported, but a major drawback of this method is the requirement of a high-power NIR laser.

Acoustic actuated cells/particles focusing and sorting are reported by some research groups [109] [110] [111]. Johansson et al. [109] described a fluorescence activated and ultrasonic transducer actuated microfluidic cell sorter system to successfully sort biological cells. They reported that a maximum throughput of 27 cells/s was achievable with their system. Jakobsson et al. [110] presented a microfluidic sorter system with acoustically actuated particle manipulation technique. They have reported sorting of fluorescent and non-fluorescent polystyrene microparticles and a potential maximum throughput of 200 cells/s.

Hydrodynamic sorting mechanism was reported to be used in a number of micro-FACS systems [82] [112]. In this type of sorting, one or more controlled fluid channels are used to alter the state of flow of the main sample channel. This action diverts the flow along with the detected biological cells/particles or molecules to one of the target collection ports from a default waste collection port. Because this switching of flow in a pressure driven system is achieved with an external driving mechanism, this kind of sorting system does not have the required response time for high-speed sorting applications. Thus, this kind of hydrodynamic sorting system is suitable for very rare target cell/particle or molecule enrichment, e.g. sorting/enrichment of VSEL stem cells from cord blood, sorting/enrichment of very rare tumor cells in the early stages of breast

cancer. Fu et al. [82] reported the use of hydrodynamic flow and pneumatic valve in a multi-layer PDMS cell sorter to successfully sort *E. Coli* cells. They have reported a maximum sorting throughput of 100,000 cells/h (~28 cells/s) and a maximum sorting efficiency of 50%. Yang et al. [112] reported a fully automatic micro-flow cell sorter that utilized hydrodynamic flow switching to deflect the desired cells for collection. They controlled the side flow by providing a number of pneumatic valves. The reported sorting throughput was 2 cells per second.

Typically in any hydrodynamic flow switching sorter, the sorting throughput is much less than the capabilities of conventional droplet-based soring in bench-top FACS systems thousands of cells per second. However, we have chosen the hydrodynamic flow switching to implement for our applications. This is mainly driven by two important points. First of all, there is no electrical (e.g. droplet-based sorting and electrophoresis), ultrasonic or optical (optical tweezer sorting) hazard associated with this type of sorting which could cause changes to the internal structures or functionalities of the human derived cells. Secondly, although the microfluidic cytometers/sorters are currently operate at very slower speed, they could possibly be improved to sort cells at much higher speed by using massively parallel architecture of fluidic and optical devices (e.g. split waveguide, array detector) currently possible to fabricate using advanced microfabrication techniques. Even with the lower throughput of a hydrodynamic flow switching sorter, considering all the advantages of a micro-fabricated cell

sorter, it could be a viable option for many applications. One such application is rare cell sorting/enrichment.

Chapter 3

Development of an efficient numerical model of laminar flows in planar µfluidic devices

3.1. Introduction[1]

A theoretical understanding of microfluidic flow is essential for predicting the behavior of flows inside microfluidic chips and to optimize the chip designs. As mentioned in the literature review, there are a number of commercial software packages available that are used to solve microfluidic problems numerically. But, a complete 3D numerical analysis of a chip-scale fluid network is still very resource intensive and thus very prohibitive for design optimization, since the optimization requires repeated numerical simulations over a wide parameter space.

---

[1] The materials in sections 3.2 and 3.3 are part of a manuscript entitled "Quasi-3D modeling and efficient simulation of laminar flows in microfluidic devices" by M. Z. Islam and Y. Y. Tsui which was submitted to Microfluidics and Nanofluidics.

In this chapter, a novel and numerically efficient "Quasi-3D" (Q3D) simulation method is introduced for planar microfluidic chips in which the microchannels are approximately rectangular in cross-section due to the nature of the etching or embossing processes in microfabrication. As will be shown below, a Fourier series decomposition of the velocity profile in the direction normal to the planar layers reduces the 3D flow problem to a limited number of 2D problems that are much more rapidly solved than a single full 3D problem without sacrificing accuracy. This approach has been used in the past [113] for simulations of electromagnetic waves in networks of rectangular waveguides.

In Section 3.2, the reduced flow equations are derived from the standard equations for incompressible, laminar fluid flow. In Section 3.3, the method is applied to test cases where the conditions allow for a simplification of the model equations and compare the results with analytic solutions and numerical results from COMSOL™ (http://www.comsol.com), a commercial 3D hydrodynamic solver. In section 3.4, the model is extended to accommodate time-varying boundary conditions and the extended model is tested for an example case.

3.2. Theoretical background

For an incompressible liquid of mass density ρ in which the only forces are viscous drag and pressure gradients, the equations that determine the local velocity, $\mathbf{V}$, are the continuity equation,

$$\nabla.\mathbf{V} = 0, \tag{3.1}$$

and the Navier-Stokes Equation (NSE)

$$\rho\,[\frac{\partial \mathbf{V}}{\partial t} + (\mathbf{V}.\nabla)\mathbf{V}] = \mu\nabla^2\mathbf{V} - \nabla P, \tag{3.2}$$

where ρ is the mass density, μ is the dynamic viscosity, and P is the scalar pressure [114]. (Additional body forces acting on the fluid such as gravity, generally negligible in microfluidics, and electric forces may be added to the equations for electrokinetic flow but are not considered here.) The fluid flow is entirely determined by the pressure distribution, the incompressibility constraint Eq. (3.1) and the boundary conditions.

The following simplifying assumptions, commonly used in microfluidic simulations, are made here:

1. The boundary condition at a channel wall is assumed to be the "no-slip" condition, V(wall) = 0. This condition is well established even at the submicron level [115];

2. The flow is quasi-static so that the time derivative in Eq. (3.2) may be neglected. By this, it is assumed that the fluid velocities are sufficiently low that any change in the boundary conditions results in an instantaneous rearrangement of the velocity and pressure fields to conform to the new conditions;

3. The flow is dominated by viscous forces so that the term $\rho(\mathbf{V}.\nabla)\mathbf{V}$ can be ignored for low Reynolds number; i.e., $|\rho(\mathbf{V}.\nabla)\mathbf{V}|/|\mu\nabla^2\mathbf{V}| \approx \rho|\mathbf{V}|L/\mu <<1$ [33]. For aqueous flows in microchannels with scale lengths on the order of 50 μm, velocities need only be much less than 1 meter per second for this to be valid. For the majority of cases of interest, velocities are significantly less than 1 meter per second. Eq. (3.2) then reduces to the much simpler equation

$$\mu\nabla^2\mathbf{V} = \nabla P \tag{3.3}$$

4. Finally, there are no free-moving bodies (particles) in the flow that can locally disrupt the velocity profile, a condition commonly assumed in microfluidic simulations containing cells or particles in low concentrations so that the particle-induced hydrodynamic disturbances in the flow field can be neglected [116].

Eqs. (3.1) and (3.3) comprise a system of four equations in four unknowns. Despite the simple appearance of these equations, analytic solutions for general channel structures are obtainable in only a few special cases and numerical solutions are generally required.

In this thesis, the analysis is restricted to planar devices in which the microchannels are rectangular in cross-section. Rectangular channels may be

formed in glass by deep reactive ion etching (RIE), or by casting polymers such as polydimethylsiloxane (PDMS) on a negative silicon master, also formed by deep RIE. An example of such a silicon master fabricated by our research group is shown in Figure 3.1(a). Except for small regions around reservoirs or vias between different levels, the channels are of constant depth, **h**, typically on the order of 50 μm. The coordinate system used here to analyze such a system of microchannels is shown schematically in Figure 3.1(b). The microchannel system is parallel to the ***horizontal*** x-y plane, and normal to the ***vertical*** coordinate, z, where $0 < z < h$.

(a)   (b)
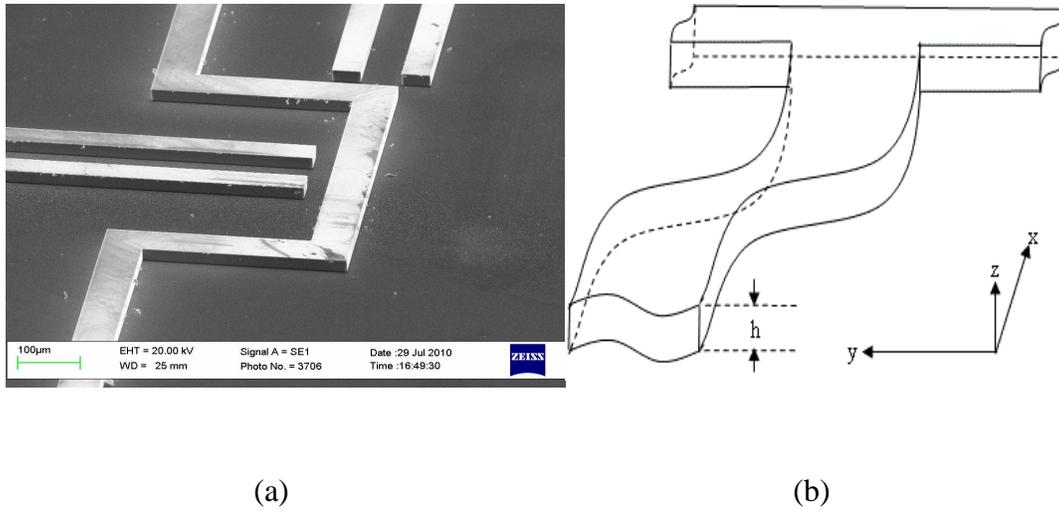
Figure 3.1: (a).Detail of silicon master formed by RIE for replicating rectangular microchannels in PDMS; (b) Schematic of an x-y planar system of rectangular microchannels of height "h".

3.2.1. Fourier expansion of the flow field

The velocity field is now expanded in a Fourier sine series,

$$\mathbf{V}(x,y,z) = \sum_{r=1}^{\infty} \left[\hat{x}\, u_r(x,y) + \hat{y}\, v_r(x,y) + \hat{z}\, w_r(x,y) \right] \sin(r\pi z/h), \tag{3.4}$$

that automatically satisfies the no-slip condition, $\mathbf{V} = 0$, at the upper and lower boundaries of the channels. The substitution of Eq. (3.4) into Eq. (3.1) results in

$$\nabla \cdot \mathbf{V} = \sum_r \left[\left(\frac{\partial u_r}{\partial x} + \frac{\partial v_r}{\partial y} \right) \sin(r\pi z/h) \right] + \sum_r \left[(r\pi w_r / h) \cos(r\pi z/h) \right] = 0.$$

$$\tag{3.5}$$

Multiplying both sides of Eq. (3.5) by $\sin\left(\dfrac{m\pi z}{h}\right)$, integrating over vertical dimension of the device, $0 \le z \le h$, and utilizing the orthogonality property of the sine functions, we have for all indices m,

$$\left(\frac{\partial u_m}{\partial x} + \frac{\partial v_m}{\partial y} \right) = \nabla_{xy} \cdot \mathbf{V}_m(x,y) = -\frac{2}{h} \sum_r (r\pi w_r / h) \int_0^h \sin(m\pi z/h)\cos(r\pi z/h)\, dz$$

$$= \sum_{\substack{r \ne m \\ r \pm m = odd}} \left[\frac{4mr}{h(r^2 - m^2)} \right] w_r. \tag{3.6}$$

Let us look at the first few equations resulting from the Eq. (3.6).

$m = 1:$ $\quad \dfrac{\partial u_1}{\partial x} + \dfrac{\partial v_1}{\partial y} = \dfrac{-4}{h}\left(-\dfrac{2}{3}w_2 - \dfrac{4}{15}w_4 \cdots \cdots \cdots \right)$

$m = 2:$ $\quad \dfrac{\partial u_2}{\partial x} + \dfrac{\partial v_2}{\partial y} = \dfrac{-4}{h}\left(\dfrac{2}{3}w_1 - \dfrac{6}{5}w_3 - \dfrac{10}{21}w_5 \cdots \cdots \cdots \right)$

$m = 3:$ $\quad \dfrac{\partial u_3}{\partial x} + \dfrac{\partial v_3}{\partial y} = \dfrac{-4}{h}\left(\dfrac{6}{5}w_2 - \dfrac{12}{7}w_4 \cdots \cdots \cdots \right)$

$m = 4:$ $\quad \dfrac{\partial u_4}{\partial x} + \dfrac{\partial v_4}{\partial y} = \dfrac{-4}{h}\left(\dfrac{4}{15}w_2 + \dfrac{12}{7}w_3 - \dfrac{20}{9}w_5 \cdots \cdots \cdots \right)$

In general, the even vertical Fourier coefficients of velocity are coupled to the odd in-plane coefficients and vice versa. However, microchannel flows are dominated by viscosity and in all regions of a device more than a few times h away from reservoirs or vias, the vertical components of velocity are negligible and the in-plane flows are symmetric around the mid-plane, z = h/2. (In section 3.3.4, justification is provided for this statement using full 3D numerical simulations.) Thus, away from inlets with non-zero, vertical input velocities, $w_r(x, y, z) = 0$ for all r and $u_r(x, y) = v_r(x, y) = 0$ for all even r. Also, as a result of Eq. (3.3), $\partial P / \partial z = 0$, or $P = P(x, y)$. So the equation for the velocity profile (symmetric along the depth) will be

$$\mathbf{V}(x, y, z) = \sum_{r=odd} \mathbf{V}_r(x, y)\sin\left(\dfrac{r\pi z}{h}\right) \qquad\qquad (3.7)$$

34

where $\mathbf{V}_r(x, y) = [\hat{x} u_r(x, y) + \hat{y} v_r(x, y)]$. Substituting Eq. (3.7) into Eq. (3.3), we obtain

$$\mu \sum_{r=odd} \left[\nabla^2_{x,y} \mathbf{V}_r(x, y) - \left(\frac{r\pi}{h} \right)^2 \mathbf{V}_r(x, y) \right] \sin\left(\frac{r\pi z}{h} \right) = \nabla_{x,y} P(x, y) \qquad (3.8)$$

Again multiplying both sides of the Eq. (3.8) by $\sin\left(\frac{m\pi z}{h} \right)$, integrating over the vertical dimension of the device $0 \le z \le h$ and utilizing the orthogonality property of the sine functions, we obtain an equation for each Fourier coefficient of the velocity field

$$\mu \left[\nabla^2_{x,y} \mathbf{V}_r - \left(\frac{r\pi}{h} \right)^2 \mathbf{V}_r \right] = (-1)^{\frac{r-1}{2}} \frac{4}{r\pi} \nabla_{x,y} P(x, y). \qquad (3.9)$$

Likewise, upon substitution of Eq. (3.7) into the continuity equation Eq. (3.1), we find that it holds for each index r.

$$\nabla_{x,y} \cdot \mathbf{V}_r(x, y) = 0 \qquad (3.10)$$

Thus the three-dimensional partial differential equations that define the problem have been reduced to a system of independent two-dimensional partial differential equations. After solving for the Fourier components of the velocity in the x-y plane, the velocity at arbitrary points, (x, y, z), can be found by summing

the Fourier series of Eq. (3.7). The number of terms to be included depends on the accuracy desired and, as will be shown later, this in turn depends on the aspect ratio of the rectangular channels. However, since a much lower number of mesh points can be used than that required for a full numerical 3D solution, the Q3D is supposed to be much more time efficient compared to the full 3D numerical solution. In the examples given in the next section, these 2D coupled equations were solved using the commercial finite element method solver, COMSOL^{TM}.

3.2.2. Numerical analysis: Introduction to finite element method

Many physical phenomena in science and engineering can be represented by partial differential equations (PDEs). Generally, solving these PDEs analytically by employing algebraic manipulation techniques for arbitrary geometry is almost impossible. One has to resort to numerical technique if the equations are complex. Among the many numerical simulation methodologies, finite element method (FEM) is typically used to solve PDEs approximately in arbitrary geometry. FEM is widely used in diverse fields of engineering and science to solve static and dynamic problems in structural mechanics, fluid mechanics (CFD), electromagnetics, biomechanics etc. The early form of this method was discussed by a few groups of people, such as Argyris, Turner and Courant [117]. Although Courant is considered the father of FEM for his early publication of the concept in 1942, it is Argyris and others who later supplied the details of the method [117] [118]. Since then FEM has become popular for engineering design and analysis

because of its flexibility in dealing with complex geometries. FEM is implemented in almost all commercially available multiphysics software like ANSYS, COMSOL Multiphysics, and CoventorWare. To solve the Q3D model developed in the previous section for a particular problem, we used the general PDE solver module of COMSOL™, Version 3.2b.

3.3. Test of the model

3.3.1. Straight rectangular channel

To check the accuracy of our model as a function of the number of terms retained in the Fourier series, the Q3D approximation was used to calculate the velocity profiles in a straight rectangular channel of width and height, *w* and *h*, (flow in the *x*-direction) and compared the result with the exact analytical series solution given by the following equation [119].

$$u(y,z) = \frac{pw^2}{8\mu}\left\{1 - \frac{4y^2}{w^2} - \frac{32}{\pi^3}\sum_{n=0}^{\alpha}\frac{(-1)^n \cosh\{(2n+1)\pi z/w\}\cos\{(2n+1)\pi y/w\}}{(2n+1)^3 \cosh\{(2n+1)\pi h/2w\}}\right\}$$

(3.11)

Here, $p = -\dfrac{dP}{dx}$, the pressure gradient in the direction of flow (- sign is accounted for the fact that pressure reduces downward the flow).
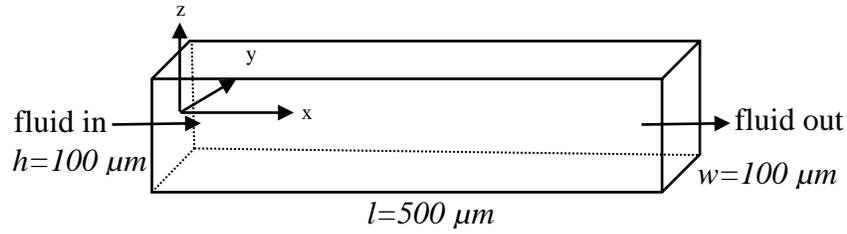
Figure 3.2: Schematics of the straight rectangular channel problem used to compare the Q3D model with the analytical solution given by equation (3.11)
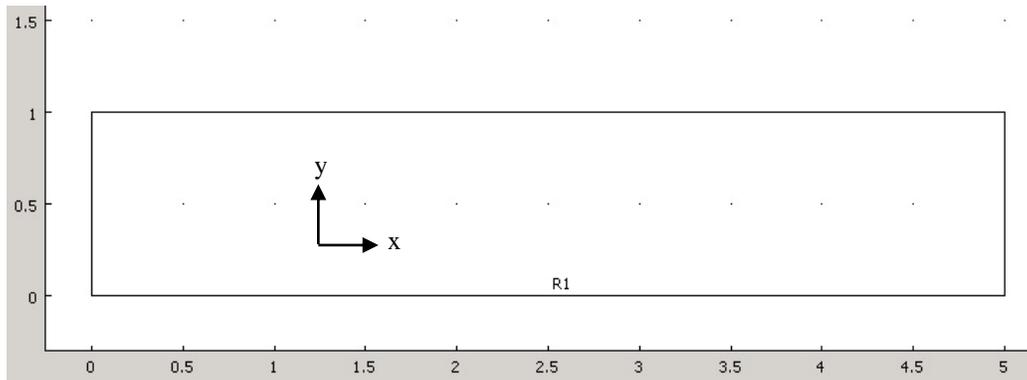
Figure 3.3: Q3D computational domain of the straight rectangular channel problem

The first example is a square channel with $h = w = 100\ \mu m$ and length 500 μm. This geometry is schematically shown in Figure 3.2. To obtain the full 3D flow solution of the problem, first we need to solve the Q3D model at the horizontal mid-plane of the geometry, $z = 0$. From the solution at the horizontal mid-plane we can synthesize the solution at any other point of interest inside the problem geometry by summing the Fourier series of equation (3.7). The

38

computational domain of this problem for the Q3D model is shown in Figure 3.3. To solve for the velocity and pressure at each point of this domain, first we set the required number (depending on the number of Fourier terms retained) of Q3D PDEs for this domain and then set the appropriate boundary conditions. At the channel ends, the input and output pressures were set to *100 Pa* and *0 Pa* respectively, and Neumann boundary conditions, $\partial u / \partial x = 0$, were used for the velocity components. As mentioned earlier, no-slip boundary condition was used at the channel boundaries. The viscosity of water at *20 ºC*, *μ = 0.001002 Pa-s*, was used in all calculations. As we have mentioned earlier, we used the general PDE solver of the popular commercial software COMSOL to solve our Q3D PDEs. The mesh used was triangular and Figure 3.4 shows a typical meshing of this geometry. Higher mesh concentration near the walls of the channel was used to account for the greater slope in the velocity profile near the walls than that in the middle of the channel. However, it is not necessary that a non-uniform meshing scheme has to be used for this to work, but it can be done to reduce the computational load. The mesh resolution should be fine enough to capture the required details of the simulation results.

Figure 3.5 shows the velocity profile on the Q3D computational domain as a surface plot. At the half-way points in the channel, $x = 250\,\mu m$, the analytical and Q3D-calculated velocity u profiles (normalized to the maximum analytical velocity value) were extracted (a) **across the horizontal mid-line**, $z = 0$, as a function of y and (b) **across the vertical mid-line**, $y = 0$, as a function of z. The

profiles are shown in Figure 3.6. The relative errors in the Q3D-calculated values of u, defined as $[u_A - u_{Q3D}]/u_A(ave)$, were also calculated along those lines. The results are shown in Figure 3.7. Note that the maximum flow velocity is 0.147 m/s and the relative error is on the order of 1% when only three Fourier terms are used.
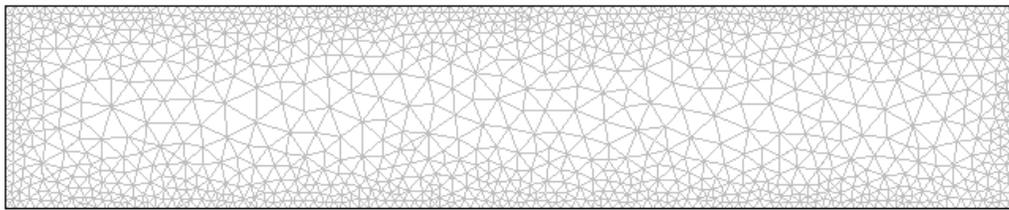
Figure 3.4: A typical mesh-plot of the straight rectangular channel used for the Q3D simulation.
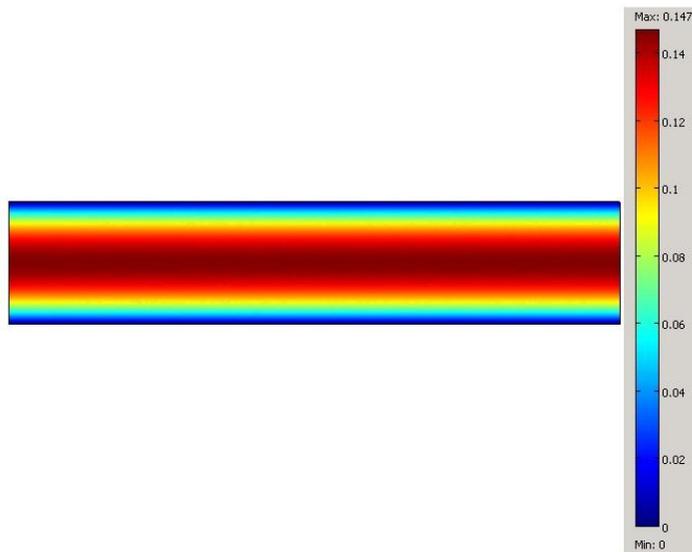
Figure 3.5: Velocity surface profile on the Q3D computational domain of the straight rectangular channel. The maximum velocity is 0.147 m/s.

(a)   (b)
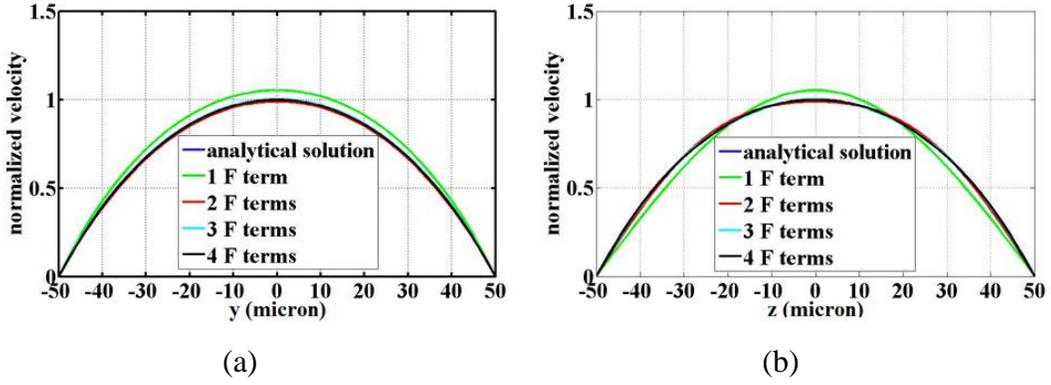
Figure 3.6: Analytical and Q3D velocity profiles for various numbers of Fourier

(F) terms in the series along the mid-lines in a square microchannel: (a) along the

horizontal mid-line, $z = 0$; (b) along the vertical mid-line, $y = 0$. The maximum

velocity is 0.147 m/s.

(a)   (b)
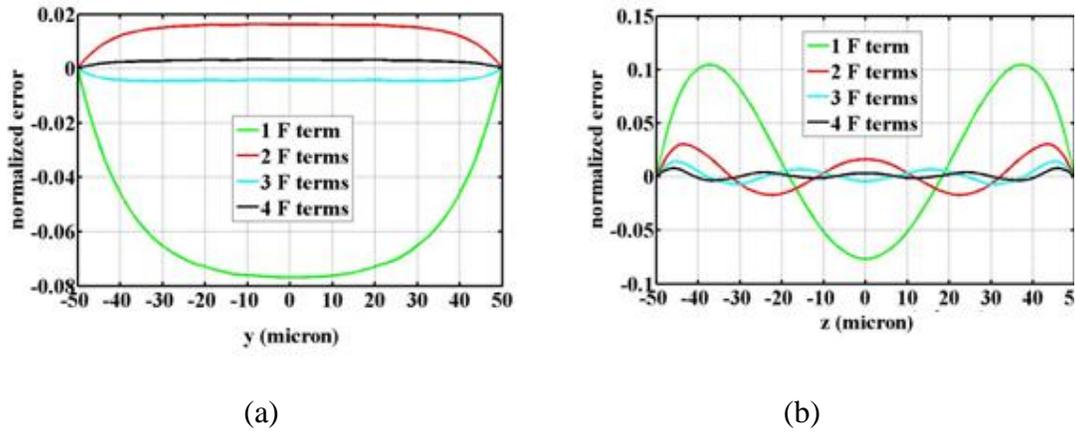
Figure 3.7: Relative errors in the Q3D-calculated mid-line velocity profiles in a

square microchannel for various numbers of Fourier (F) terms in the series: (a)

horizontal mid-line, $z = 0$; (b) vertical mid-line, $y = 0$.   The normalization factor,

$u_A(ave)$, in the error definition refers to the average of u_A across either the

horizontal or the vertical mid-line. The maximum velocity was 0.147 m/s.

41

An alternative error measure is the normalized root-mean-square (RMS) error over the whole cross-section defined as $\sqrt{\sum(u_A - u_{Q3D})^2 / \sum u_A^2}$, where the summations are over all analytic (A) and Q3D velocity components and all positions in the cross-section of the channel at $x = 250$ μm. For the square channel example above, the RMS error decreases with the increasing number of Fourier terms included in the Q3D model as shown in Figure 3.8(a). As shown in this figure, the RMS error is less than 1% when only one Fourier term is included in the model (in log10 units).

(a)   (b)
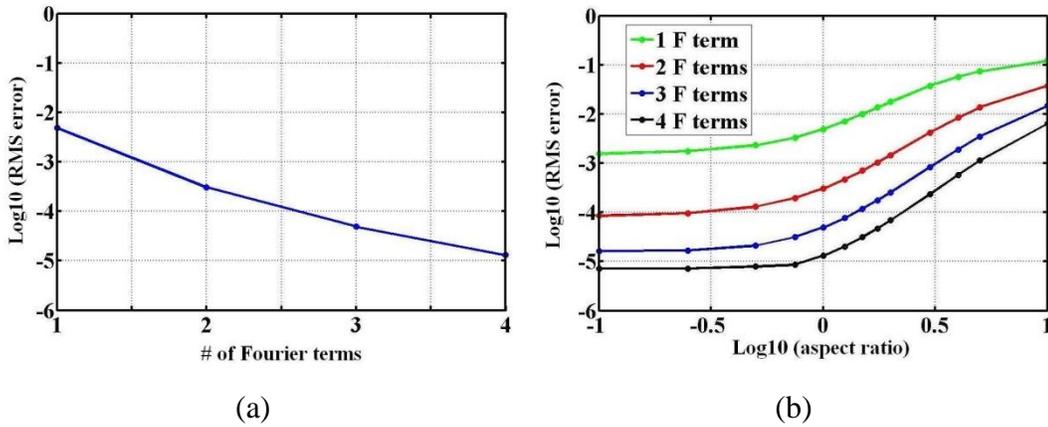
Figure 3.8: Total cross-sectional RMS error as a function of the number of Fourier terms used in the Q3D simulation for (a) the square channel, and (b) as a function of the channel aspect ratio, $\alpha = h/w$, over the range $0.1 \le \alpha \le 10$.

The accuracy of a simulation depends on the aspect ratio, $\alpha = h/w$, of the channel as shown in Figure 3.8(b). In this figure, the RMS error (in log10 units) is shown for aspect ratios over the range $0.1 \le \alpha \le 10$, and for up to four Fourier

terms included. For wide or shallow channels, ($\log10(\alpha) < -0.5$), the flow profile in the z-direction (vertical) is expected to be nearly parabolic and the RMS error is much less than 1% when only the first Fourier term is used. Conversely, for narrow channels, $\log10(\alpha) > +0.5$, the flow profile in the z-direction is expected to be more plug-like and more Fourier components are required for the same accuracy. Still, even with an aspect ratio of 10, the RMS error is less than 1% when only four Fourier terms are included.

3.3.2. Flow in a T-cell

The next test of the Q3D approximation is the solution of flow in a T-cell (shown in Figure 3.9) with three Fourier terms. Since no analytical solution for this system is available, our model solution is compared to the full 3D solution obtained using *the incompressible Navier-Stokes application module* of the commercial multiphysics software COMSOL™, Version 3.2b. The input arm is *500 μm* long and the output arms are *200 μm* in length and all arms have cross-sectional dimensions of *100×100 μm²*. As we have mentioned earlier, to solve the problem using the Q3D model, first we need to solve the Q3D model at the horizontal mid-plane of the geometry, $z = 0$ (Q3D computational domain). From the solution at the horizontal mid-plane we can synthesize the solution at any other points in the problem domain by summing the Fourier series of equation (3.7). The Q3D computational domain of this T-cell problem is shown in Figure 3.10(a).

Figure 3.10(b) shows the computational domain for the full 3D incompressible

Navier-Stokes application module of COMSOL.
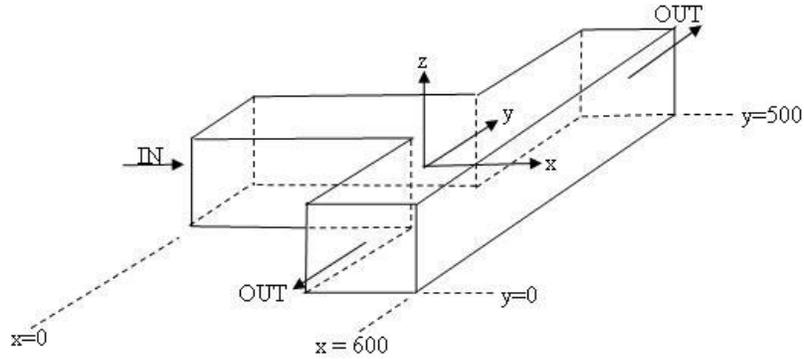
Figure 3.9: Schematics of the T-cell problem used to compare the Q3D model

with the full 3D incompressible Navier-Stokes application module of COMSOL.

(a)	(b)
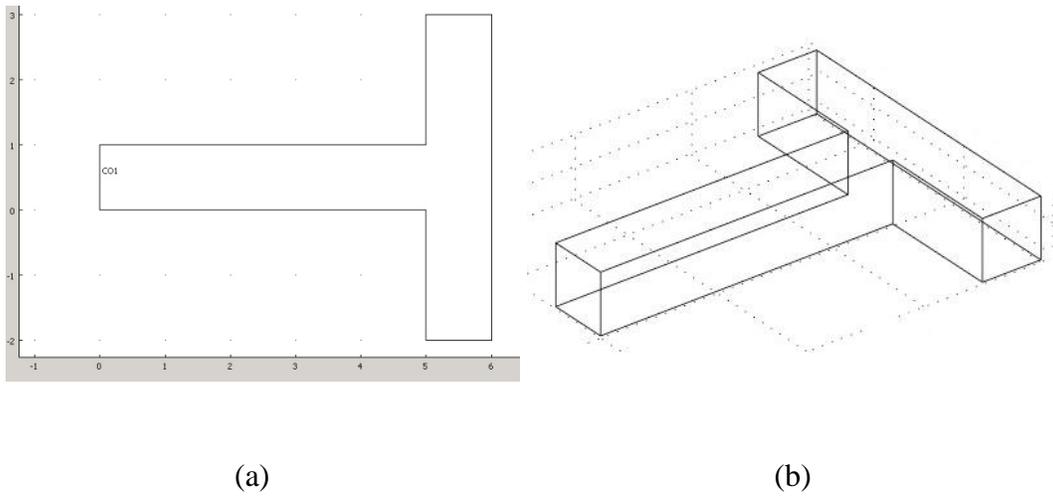
Figure 3.10: (a) Q3D computational domain of the T-cell; (b) full 3D COMSOL

Navier-Stokes computational domain of the T-cell

As usual, we defined a water-like fluid inside both computational domains. The viscosity of water at *20 ºC*, *µ = 0.001002 Pa-s*, was used in all calculations. At the channel ends, the input and output pressures were set to 100 Pa and 0 Pa respectively, and Neumann boundary conditions were used for the velocity components. As mentioned earlier, no-slip boundary condition was used at the channel boundaries. Triangular meshes were used for Q3D simulation. Meshed domain for Q3D simulation is shown in Figure 3.11(a). Normally, the same x-y mesh pattern was used in the full 3D Incompressible Navier-Stokes Application Module of COMSOL as the Q3D model, and, the element pattern was repeated for several levels vertically. Figure 3.11(b) shows the meshed domain of the full 3D incompressible Navier-Stokes simulation.

(a)   (b)
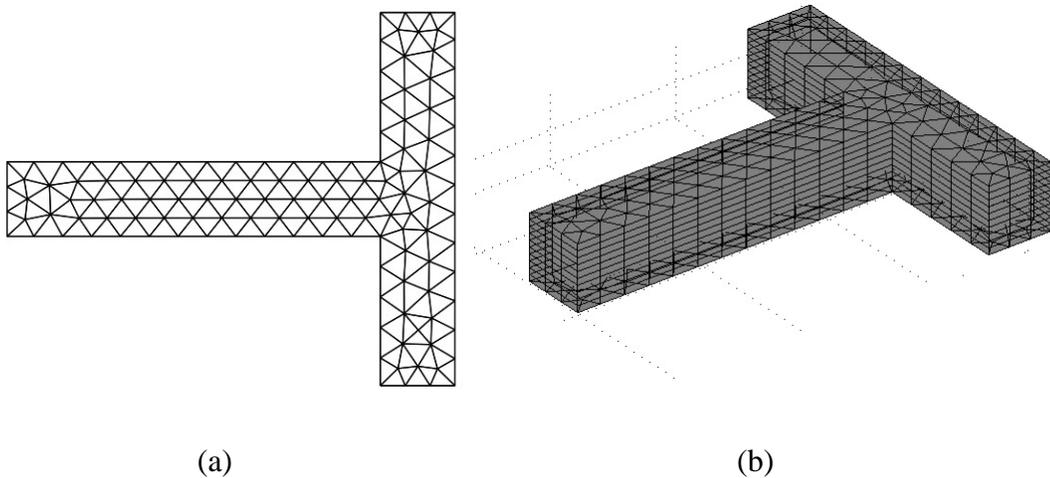
Figure 3.11: (a) meshed domain for Q3D simulation; (b) meshed domain for the full 3D COMSOL incompressible Navier-Stokes simulation

45

The surface plots of absolute velocity for the two simulation methods are shown in Figure 3.12(a) and 3.12(b) respectively. The *x*- and *y*-velocities along the centre lines of the input and output arms, respectively, are shown in Figure 3.13(a) and 3.13(b), and similarly the pressure in Figure 3.14(a) and 3.14(b). The differences between the Q3D and COMSOL calculations are indistinguishable on this scale. The normalized differences for either quantity, defined as $[v_{3D} - v_{Q3D}]/v_{3D}(ave)$, are shown in the same figures with the scale on the right-hand axis. Note that the normalized difference is less than 1%.

(a)   (b)
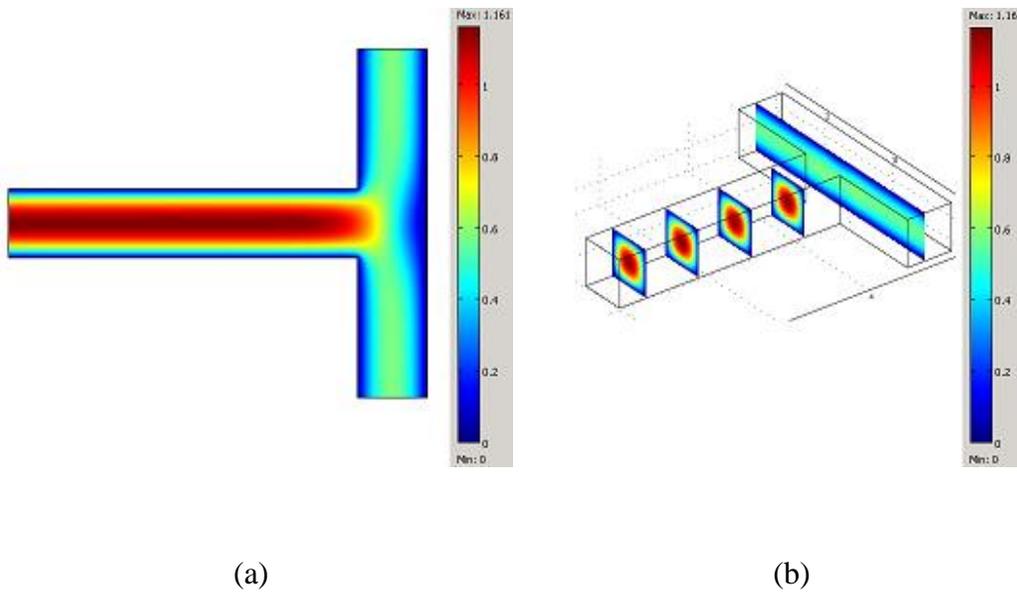
Figure 3.12: (a) surface velocity profile on the Q3D computational domain of the T-cell; (b) the surface velocity profile at some slices of the 3D incompressible Navier-Stokes computational domain of the T-cell.

(a)   (b)
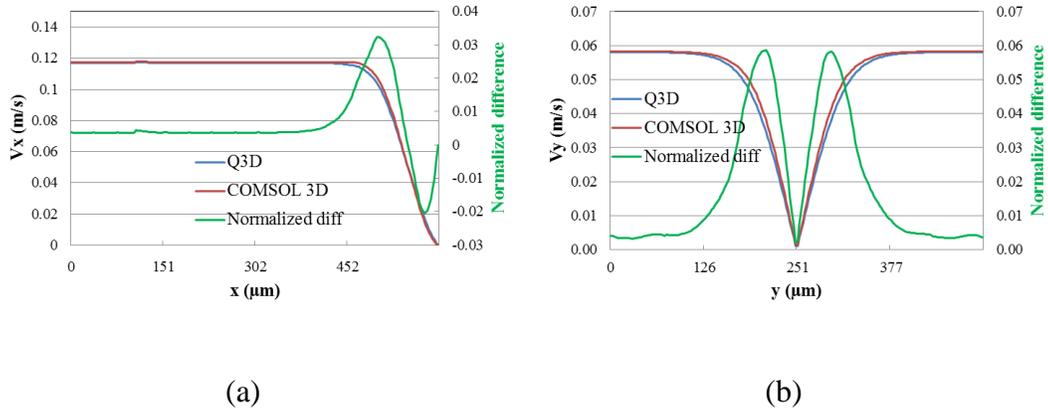
Figure 3.13: Velocity profiles along the centre lines of the input and output channels and normalized differences from the COMSOL 3D Navier-Stokes calculation: (a) velocity in input direction; (b) absolute value of the output velocities

(a)   (b)
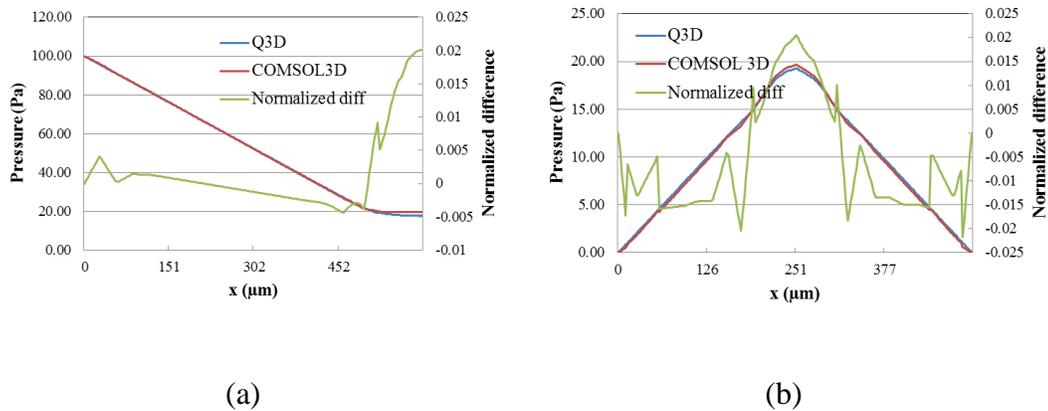
Figure 3.14: Pressure profiles along the centre lines of the input and output channels and normalized differences from the full 3D COMSOL Navier-Stokes calculation: (a) pressure along input direction; (b) pressure along output directions.

47

3.3.3. Computational resources
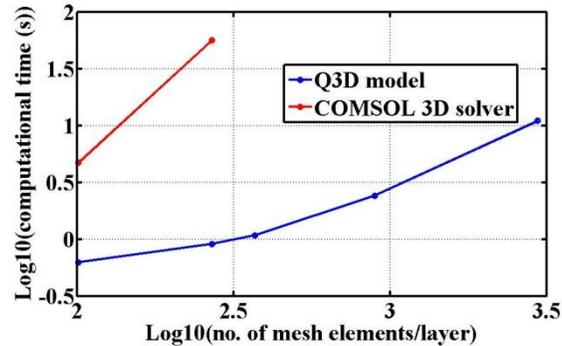
Figure 3.15: computational time as a function of number of mesh elements for the two simulation techniques: Q3D model and 3D incompressible Navier-Stokes application module of COMSOL.

The simulations described in the previous section were all performed on a desktop PC (AMD Athlon™ 64X2 Dual Core 4200 @ 2.2 GHz) with 896 MB of RAM running COMSOL Version 3.2b. For a direct comparison of computational speed, the same x-y mesh pattern was used in the Q3D model and 3D Incompressible Navier-Stokes Application Module of COMSOL, and for the latter, the element pattern was repeated for eight levels vertically. Also the underlying FEM solver and its parameters setting were kept the same in the Q3D and the 3D incompressible Navier-Stokes application module. The resulting computational time (in log10 unit) as a function of the number of meshes per layer (in log10 unit) is shown in Figure 3.15. With the limited resources of the desktop computer mentioned above, the 3D incompressible Navier-Stokes

application module of COMSOL ceased to run with more than 250 elements per level due to memory limitations. With that number of elements, the Q3D calculation was more than 50 times faster than the COMSOL calculation.

3.3.4. Justification of the approximation of symmetric flow
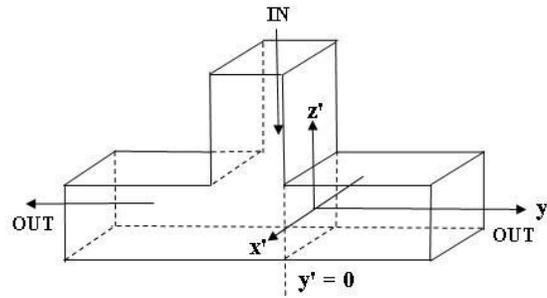
Figure 3.16: T-channel with vertical inlet to demonstrate the rapid relaxation to symmetric velocity profiles in the outlet arms.

In Section 3.2.1, it was stated that short distances away from inlets with vertical flows, the vertical components vanish and the velocity profile can be assumed to be vertically symmetric. To justify this claim, the previous 3D COMSOL results for a T-channel are used except that the input is now considered to be "downward" (-z' direction as shown in Figure 3.16). The new coordinates (x', y', z') now correspond to (z, y, -x) in the original orientation. The first eight Fourier components of the vertical (z') and axial (y') output velocity distributions were calculated at each value of x' in the outlet channel up to a distance of 175 μm from the inlet-outlet intersection. The maximum absolute values of these

49

components, normalized by the maximum value at each y' position, are plotted in log10 units in Figure 3.17(a) and 3.17(b) respectively. Figure 3.17(a) shows that all Fourier components of the vertical velocity component effectively disappear within 100 μm of the inlet. Figure 3.17(b) shows that all even Fourier components of the axial velocity component disappear while the odd components also quickly reach the equilibrium values expected in a vertically symmetric velocity profile.

(a)   (b)
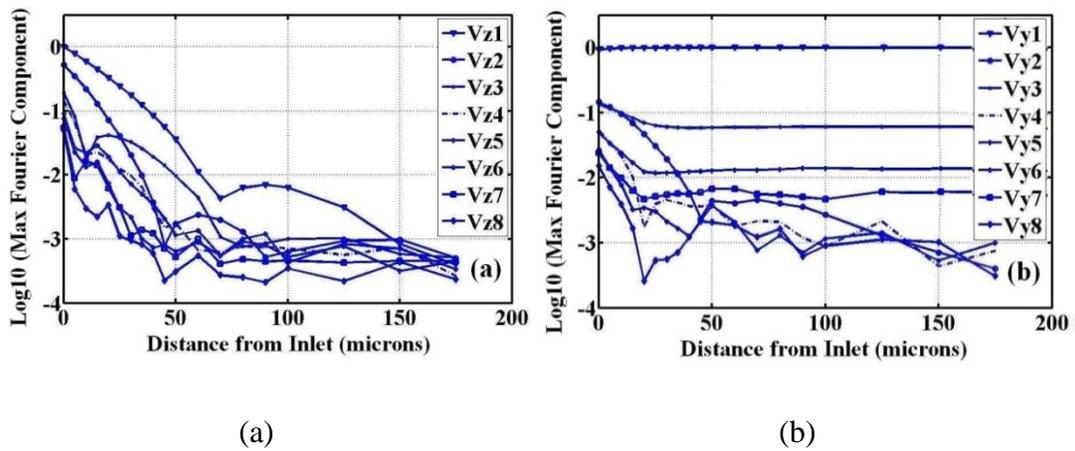
Figure 3.17. Maximum Fourier components of the velocity profiles as a function of the distance from the inlet: (a) vertical velocity components; (b) axial velocity components.

3.4. Extending the model to time-varying 3D flow problems

The Q3D model developed earlier for steady-state planar microfluidic flows can be extended for solving time-dependent flow problems. After following similar mathematical manipulations as shown in section 3.2, the Fourier components of the time-dependent flow velocities can be found to follow the following relationship with the time-varying pressure P:

$$\mu\left[\nabla^2_{x,y}\mathbf{V}_r(x,y,t)-\left(\frac{r\pi}{h}\right)^2\mathbf{V}_r(x,y,t)\right]-\rho\frac{\partial\mathbf{V}_r(x,y,t)}{\partial t}=(-1)^{\frac{r-1}{2}}\frac{4}{r\pi}\nabla_{x,y}P(x,y,t)$$

(3.12)

The continuity equation (3.10) remains the same for the time-dependent problem as the steady-state flow situation.

To solve the time-dependent PDEs of (3.12) along with the continuity equation we must use a general time-dependent PDE solver. Again, we resort to the commercial PDE solver module of COMSOL to solve our time-dependent Q3D model numerically. To show the applicability of our time-dependent model, we pick a typical problem of a flow switching system that has potential application in hydrodynamic cell sorting system [shown in Figure 3.18]. The four input-output arms are each *200μm* long and all arms have cross-sectional dimensions of *100×100 μm²*. As before, a water-like fluid is defined in the

51

computational domain. The boundary conditions are chosen as follows. Main inlet: time-independent flow profile, flow switching inlet: a pulsating flow (maximum flow velocity switches between 0 and a predetermined value), collection ports 1 and 2: kept at *0 Pa* pressure value. At all other boundaries, no-slip boundary conditions are used, as usual, for flow velocities. The time dependent boundary condition at the flow switching inlet is shown in Figure 3.19.

Main inlet

Flow switching inlet

Collection port II

Collection port I
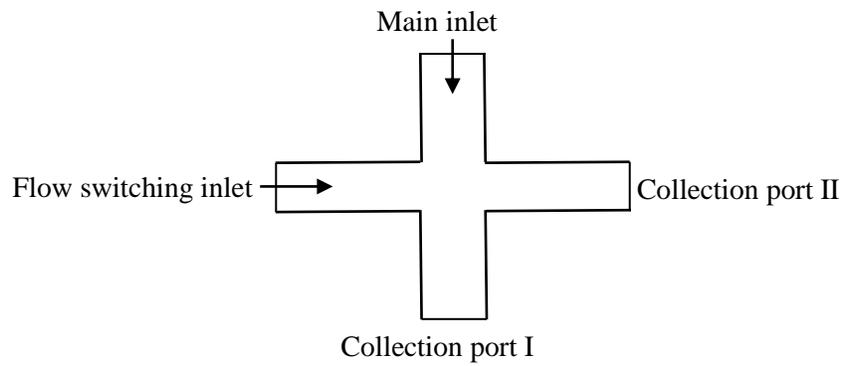
Figure 3.18: A hydrodynamic flow switcher. The main inlet has a constant pressure (e.g. sample inlet) and the flow switching inlet has a time-varying velocity profile to switch the main channel flow.

The streamline and arrow plots of the fluid flow inside the computational geometry at two different times of interest (0.05 s and 0.15 s, as the flow should switch at 0.1 s) are shown in Figure 3.20. As Figure 3.20 (a) shows the main flow is divided between the collection ports when the switching flow is not activated. After the activation of the switching flow inlet at time 0.1 s, the main inlet flow is
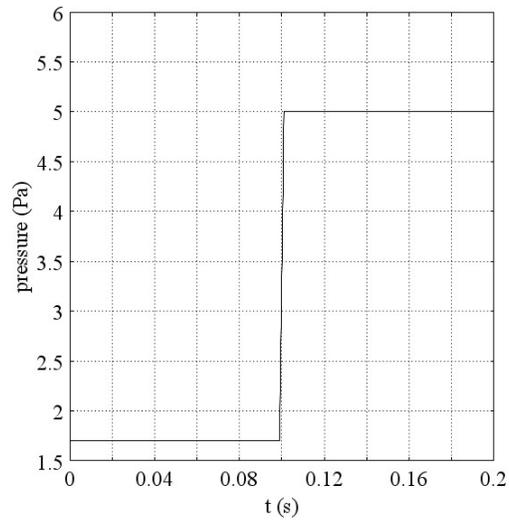
Figure 3.19. A time-varying pressure boundary condition applied at flow

switching inlet

(a)   (b)
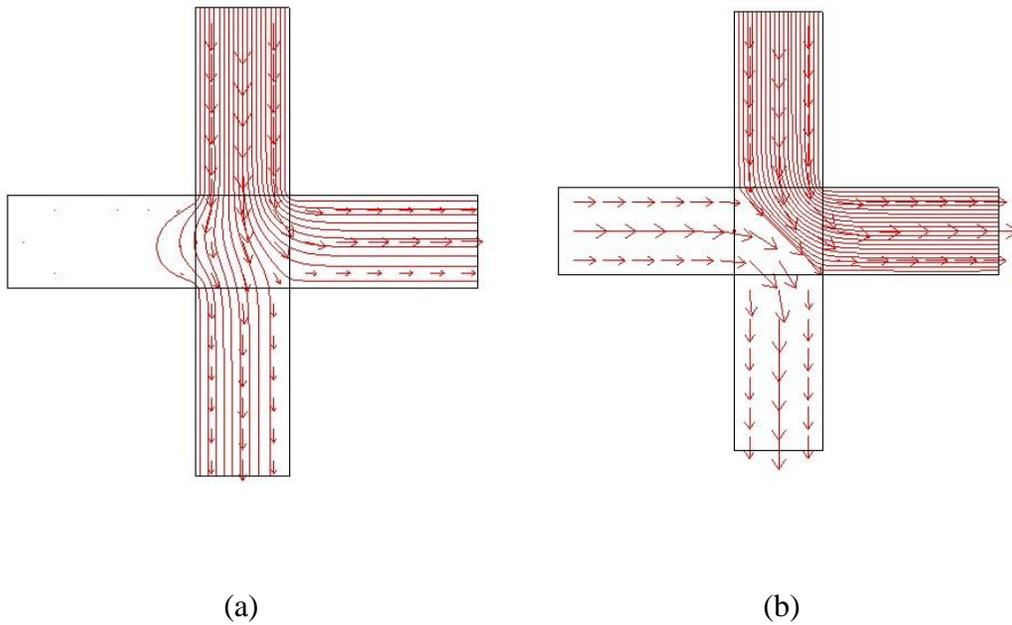
Figure 3.20. (a) Streamline plots at the centre plane of the channel at time, t =

0.05 s; (b) the same plots at time, t =0.15 s. Because the flow switch is activated at

t = 0.1 s, the main inlet flow is completely diverted to the collection port II.

diverted totally to the collection port II. As the flows are laminar, there is no mixing of fluid from the two inlets. Fluid flow from switching inlet occupies the whole of the collection port I, and, that`s why the main inlet flow is diverted to the collection port II. The corresponding surface plots of the velocity profiles are shown are shown in Figure 3.21.

(a)   (b)
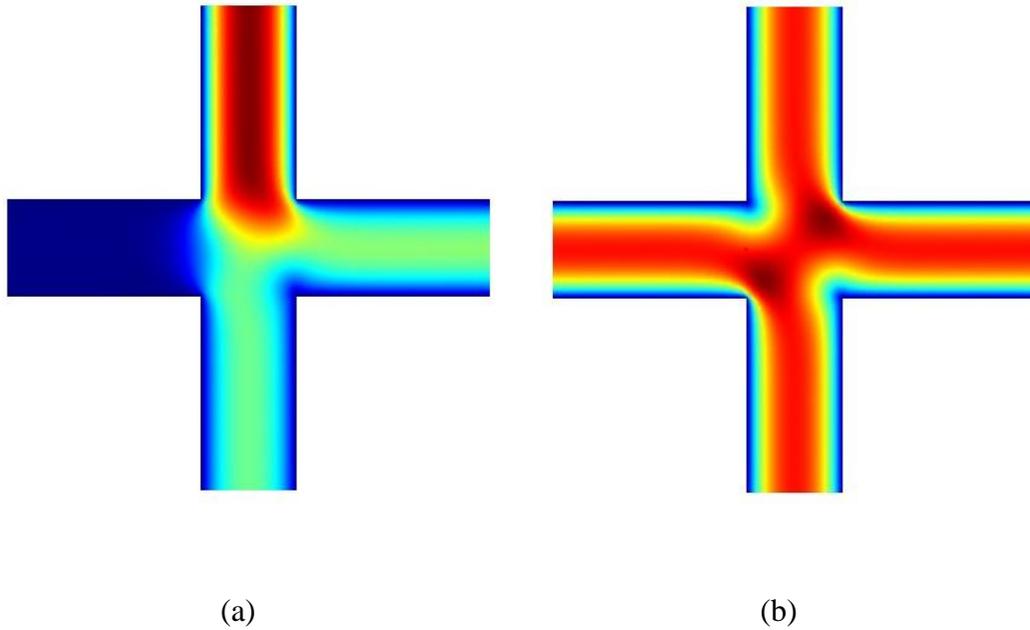
Figure 3.21. (a) Surface plot of the magnitude of velocity at horizontal mid plane at time, t = 0.05 s; (b) the same plot at time, t =0.15 s. Because the flow switch is activated at t = 0.1 s, it shows that the main inlet flow is switched from the collection port I to the collection port II.

The time-varying velocity profiles at the centres of the switching and main inlet boundaries are shown in Figure 3.22. Due to the change in the pressure value

at the flow switching inlet at time, t = 0.1 s, the velocity of flow changes here from 0 to a certain value. The most important thing here to observe is the velocity profile of the main flow inlet (shown in Figure 3.22 (b)). Initially the flow velocity at this end was higher. But it is reduced to a lower value as the flow switching inlet is activated. In this particular example, the boundary conditions were set to such values that the flow velocities at the main and flow switching inlets were settled to equal value so that the main flow inlet is switched completely to the collection port II.
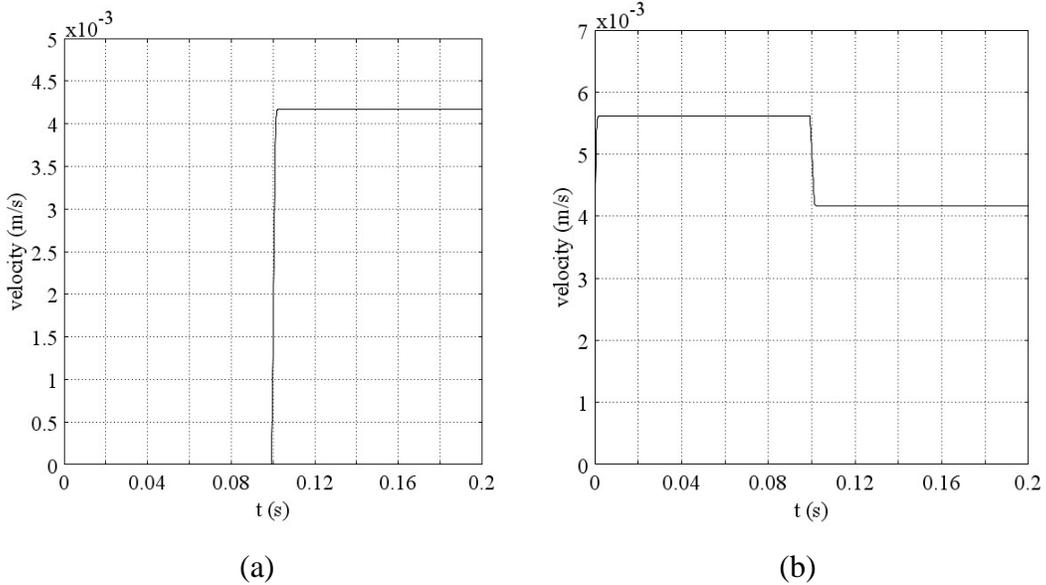
Figure 3.22. Velocity as a function of time: (a) at the centre of the flow switching inlet boundary; (b) at the centre of the main inlet boundary

3.5. Conclusion

In this chapter, we have developed a novel quasi-3D model for efficient simulation of flows in planar microfluidic devices with low Reynolds numbers. A Fourier series decomposition of the velocity profile of an incompressible fluid along the height of the microfluidic chip reduces the 3D Navier-Stokes flow equations to several independent 2D equations. This makes the solution of a microfluidic flow problem feasible with significant decrease in computation time compared to the prevailing numerical software packages. The significant reduction in computation time allows detailed 3D modeling of microfluidic devices on desktop computers and design optimization of chip-scale devices.

Finally it should be mentioned here that, in spite of the computational advantages of this model over other numerical approaches, it has some limitations too. The quasi-3D model is valid only for planar microfluidic devices with geometries and flow parameters characterized by a low Reynolds Number pressure-driven flow. The good news is that most of the microfluidic applications developed utilizing the microfabrication technologies fall within these limitations and can be studied by this model.

Chapter 4

Prototyping of miniaturized flow cytometer

4.1. Introduction[2,3]

In principle, experimental and numerical approaches can be used to design a Lab-on-Chip (LOC) system. But as explained in the previous chapter full 3D chip scale simulation remains very expensive to perform and thus the experimental approach is the main approach currently being adopted for designing LOC systems. As mentioned in Chapter 1, the experimental approach is based on a fabrication-design-fabrication loop, which could be extremely expensive and time consuming. Typically, an optimized chip development can take several months to

---

[2] Some of the materials of this chapter forms parts of an original article entitled "Rapid and cheap prototyping of a microfluidic cell sorter" by M. Z. Islam, J. N. McMullin and Y. Y. Tsui which is published in Cytometry Part A 79A, 361-367, 2011

[3] A part of this chapter forms an article entitled "Development of an opto-microfluidic flow cytometer for the sorting of stem cells from blood samples" by M. Z. Islam et al which is published in the proceedings of SPIE, 7386, 73860C(1-8), 2009

a year, which is prohibitive to medium-size and small biotech companies and academic laboratories [120]. So, for this kind of design methodology, it is a good idea to follow some sort of rapid and low-cost prototyping techniques to realize a conceptual model of the desired functionalities and test that model in proof-of-concept experiments during the initial stages of the fabrication-design-fabrication loop.

As we have mentioned earlier in Chapter 1, for the last few years there is a growing interest toward miniaturized flow cytometer research. The miniaturized flow cytometers offers the potential for disposable assays, cost and size reductions and portable point-of-care diagnostics [15]. We set one of our research goals to develop a micro-flow cytometer for stem cell sorting applications, as we have mentioned in chapter 1. However, before we proceeded to fabricate a sorter chip utilizing the state-of-the-art microfabrication technologies, we had utilized some off-the-shelf materials and tools to make prototypes of typical miniaturized cell sorter architecture and performed some proof-of-concept experiments to characterize their functionalities. In this chapter, we describe two methods of prototyping that we adopted to realize the initial model of the cell sorter device.

4.2. Overview of microfluidic prototyping

4.2.1. Defining microchannels on substrate materials

There are a number of methods available to date that can be used to define microchannels on a number of different materials. Silica-based technologies, such as glass or quartz etching, Silicon surface etching, poly dimethylsiloxane (PDMS) micromolding, soft lithography etc. produce microfluidic devices or master mold by photolithographic and wet/dry chemical etching processes to pattern the substrate with the required microchannel configuration [70] [121] [122]. These techniques are relatively time consuming and they typically require the use of expensive state-of-the-art fabrication facilities. A number of ways of prototyping polymer microsystems are reported in the literature, which are fast and cost-effective. Desktop machinery for making microchannels with feature sizes down to a few μm exists at prices a fraction of the price of typical state-of-the-art clean-room processing equipment. A brief overview of some of these methods is given here.

Several groups have investigated the laser based direct micromachining techniques of polymeric materials to produce the microfluidic channel structures on poly methyl methacrylate (PMMA) substrates [122] [123] [124] and other polymeric materials [125]. Apart from the Gaussian channel cross-sections resulting from these techniques, they have the disadvantages of being costly and potential hazard of working with lasers. Some groups have used computer

numeric controlled (CNC) micro-mill or mini-mill to directly inscribe the microfluidic channels into the substrates [126] [127]. Feature size of a few μm was reported. Yuen et al. [128] reported a method for prototyping of flexible microfluidic devices using a desktop digital craft cutter. The desktop digital craft cutter is similar to a desktop printer/plotter, but it cuts papers and other materials like vinyl with a blade instead of printing/plotting onto it. It is normally used for making vinyl décor, scrapbooking, paper crafting, etc. Microchannels as thin as 200 μm in width, various functional planar and 3D microfluidic devices were demonstrated with this digital craft cutter rapid prototyping method. The complete fabrication process from device design (layout editing) to working device can be completed in minutes without the need of expensive equipment. However this technique cannot be applied to a rigid working material.

4.2.2. Bonding of microfluidic devices

Several methods of irreversible and reversible bonding for microfluidic device prototyping exist. Most commonly used irreversible bonding methods are gluing, which is done chemically or by UV exposure, thermal/fusion bonding, laser bonding etc. Among these techniques, thermal/fusion bonding can provide much smoother interface and has the potential to make the process very simple and cheap. Most commonly used reversible bonding method is the double-sided adhesive bonding. This method was used in Ref. [128]. Because of this non-

permanent bonding, it can be very challenging to obtain a leak-free chip with this method. This also makes the chip difficult to handle and clean.

4.3. Making of the Prototypes

In our case we used two low cost methods to make two cell sorter prototypes for our proof-of-concept experiments. They are:

(a) **Prototype I:** Flow channels were inscribed into a transparency sheet and bonding was achieved through an irreversible UV epoxy gluing.

(b) **Prototype II:** Flow channels were inscribed into a transparent polymer material, called Surlyn® [http://www2.dupont.com/Surlyn/en_US/], which is new in application in microfluidic devices but has been being used in a variety of applications for years – from food and cosmetic packaging to consumer and industrial goods. One of its most important applications has been in window glass lamination. We have adapted the technology of curing shatter-proof polymer film between dual layer automotive glasses to the bonding of this prototype. Compared to other methods of prototyping reported in literature, this method uses less expensive tools and materials for defining microfluidic channels on the substrate material, and hence results in low-cost chips. The bonding of chip layers is achieved through a simple and inexpensive fusion bonding set-up without the use of a commercial bonder. In addition, the bonding set-up provides a moderate vacuum environment that

aids in making the bonding interface bubble-free. Thus it is expected to provide better bonding interface between the layers.

4.3.1. Prototype I

As mentioned earlier, a general transparency sheet was used to make the first cytometer chip prototype. The development process of the miniaturized prototype is shown and explained graphically in Figure 4.1(a). A Y-shaped microfluidic channel and straight channels for optical fiber insertions were cut into a transparency sheet and then bonded with UV curable epoxy between two standard microscope glass slides. The upper slide was coated with chromium film to reduce unwanted scattered light reaching the system's photo detector during experiments, and, an observation window of approximately 100 μm × 1 mm in size was etched to expose a small detection region in the microfluidic channel with a view to limiting the solid angle of detection thus improving the signal-to-noise ratio of the cytometer.

The channel dimensions and structure are shown in Figure 4.1(b). As shown, the chip contains one fluid inlet and two outlets that are to connect to off-chip syringe and collection vessels through polyethylene tubing. The width of the fluid channel is 1.5 mm and the distance from the observation point to the separation point into the two channels is 17 mm. Since this transparency sheet

was tightly bonded between two standard glass slides, the height of the microfluidic channel is approximately the thickness of the polymer sheet, 200 µm.
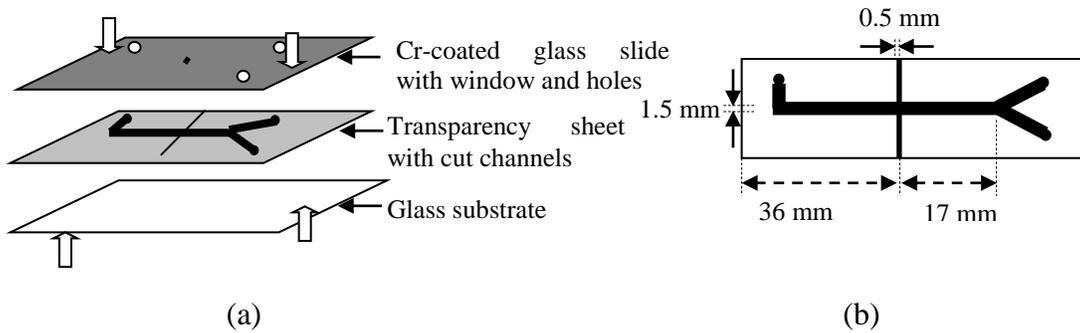
Figure 4.1: (a) procedure of fabrication of cytometer chip. (b) Details of channel dimension.

4.3.2. Prototype II

The process flow diagram for the making of the prototype II is shown in Figure 4.2. First of all, a steel template of the chip with the intended microfluidic channel structures and openings for optical fibers is made by utilizing water-jet cutting technology. The template is then placed over a transparent, thin Surlyn® (DuPont™) sheet and a hot knife (Hot-Knife™, 25 Watt, Industrial Fiber Optics, Tempe, AZ, USA) is used from the above to inscribe the features through the template into the Surlyn® sheet. Hot Knife™ is normally used for cutting optical fiber with no splintering or fracturing. It has a fine-point blade and is used like

soldering iron or wood burning tool. The feature-inscribed Surlyn® sheet is then fusion bonded in between two microscope glass slides employing a special technique described below. Finally, optical fibers are inserted into the corresponding openings from sides and are kept in their places by bonding them with UV epoxy.

Making of a steel template of the channel structures by using the water-jet technology

Inscription of the channel structure of the template in Surlyn by using a 'hot knife™'

Fusion bonding of the inscribed Surlyn sheet in between two microscope glass slides

Insertion and bonding of optical fibers into the chip by UV epoxy
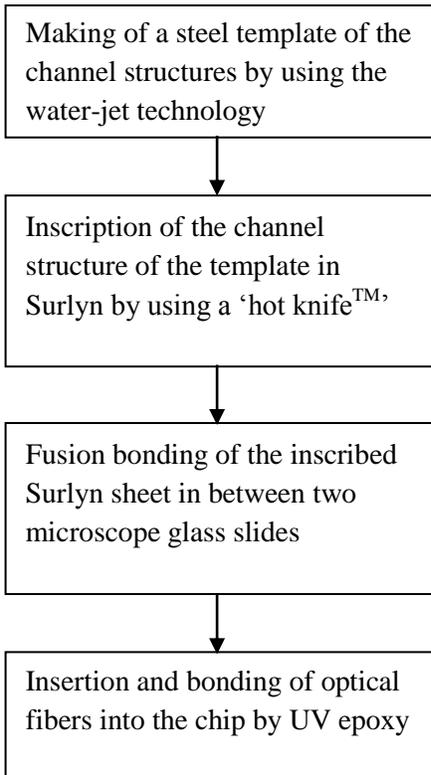
Figure 4.2: Steps in the making of the cytometer chip Prototype II

Similar to Prototype I, the Prototype II also contains a Y-shaped microfluidic channel, the most commonly used flow-channel shape in microfluidic cytometers, and two straight side channels for optical fiber insertions

64

for light input and light dumping. The channel dimensions and structure are shown in Figure 4.3. The minimum feature size attainable with the in-house water-jet technology was about 1,000 µm. So the width of the channels in the template was limited to this size and that in the Surlyn® sheet was a little bit smaller, about 800 µm. As said earlier, the feature-inscribed Surlyn® sheet is fusion bonded in between two microscope glass slides. Similar to prototype I, the upper slide is coated with a film of chromium to reduce unwanted scattered light reaching the photo detector during experiments. A circular observation window of 100 µm in radius is etched at this slide to expose a small observation window on top of the detection region of the microfluidic channel. As mentioned earlier, this window is expected to improve the signal-to-noise ratio of the detection system of the cytometer by limiting the solid angle of detection. The height of the microfluidic channel is approximately the thickness of the Surlyn® sheet which is about 325 µm.
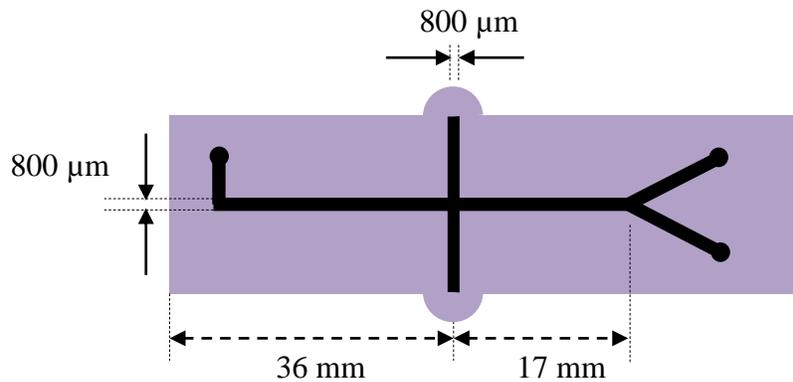
Figure 4.3: Details of the channel structure in the Surlyn® sheet. The thickness of the sheet and hence the height of the channel is ~325 µm.

65

We made use of three different available options to fusion bond the Surlyn® sheet in between two microscope glass slides. They are (1) use of a commercial bonding machine, Suss microtech™ wafer bonder, (2) use of a vacuum hot plate, and (3) adoption of the curing technique of shatter-proof polymer film between dual layer automotive glasses. Among the three options the last one is especially attractive, because it does not require any microfabrication facility and it is inexpensive and easy to implement. The bonding process utilizing this method is described here. The feature-inscribed Surlyn® film is sandwiched between two microscope glass slides. A special type of release fabric (Bleeder Lease® B, Airtech Advanced Materials Group, Huntington Beach, CA, USA) is hand cut and placed to cover the periphery of the glass slides and a breather layer (Airweave® N-10, Airtech Advanced Materials Group, Huntington Beach, CA, USA) is applied over the release fabric. The part, along with the bottom part of a vacuum valve, is then placed in a plastic film envelop bag, the vacuum valve top is installed carefully after slitting through hole in the bagging film. Then the vacuum line is installed and air is removed from the bagged part by a vacuum pump. The process is pictorially shown in Figure 4.4. Finally, the envelope is placed in an oven and kept it there in 105 ºC (glass transition temperature of Surlyn®) for 5 min. Thus, the Surlyn® film is fusion bonded between the glass slides. Tens of chips can be processed simultaneously in a single plastic film vacuum envelop. It is to be mentioned here that this prototyping method provides rigid, irreversibly bonded microfluidic chips that can be handled and cleaned quite easily without the fear of pulling the layers apart.
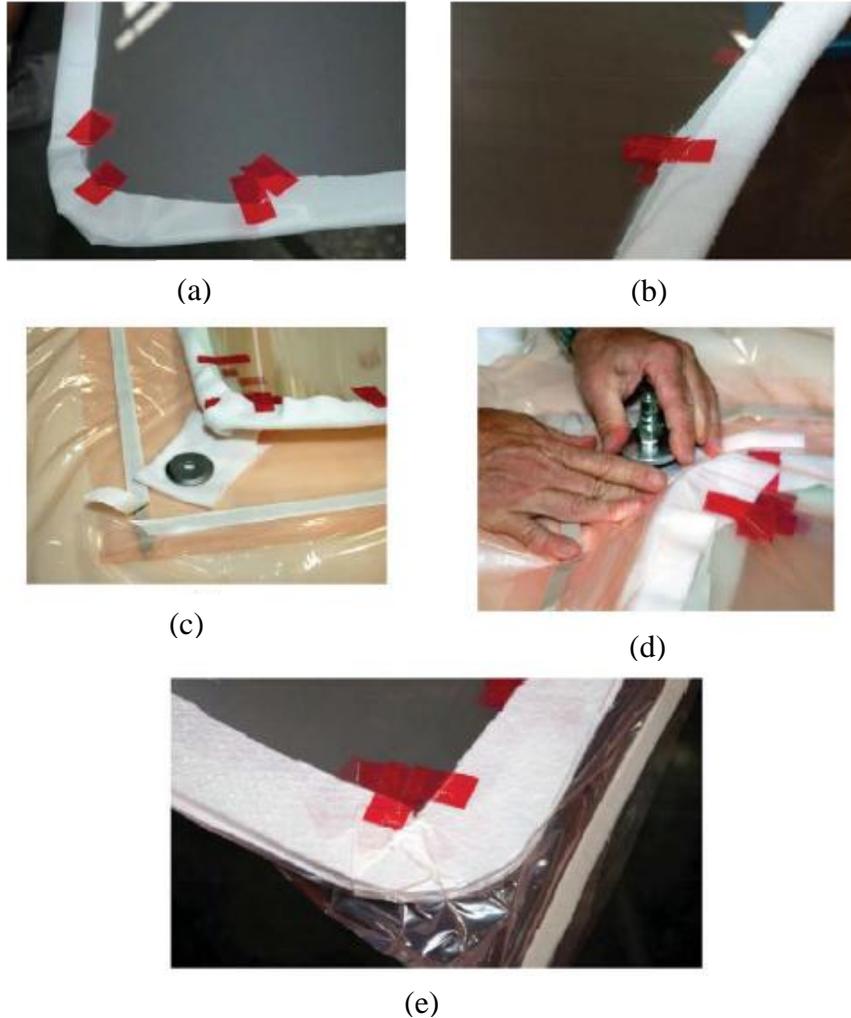
Figure 4.4: Pictorial representation of some of the steps of fusion bonding of Surlyn® film with microscope glass slides: (a) the release fabric, Bleeder Lease® B, should cover the entire edge surface of the glass-Surlyn®-glass assembly; (b) the breather layer over the release fabric. Overlapping tapes help minimize the surface contact; (c) the bottom part of the vacuum valve is placed over a small piece of breather cloth inside the bag; (d) the top part of the vacuum valve is installed carefully after the envelop is sealed properly and slitting through a hole in bagging film; (e) breather around the periphery aids in air removal by vacuum.

4.3.3. Assembling the prototypes
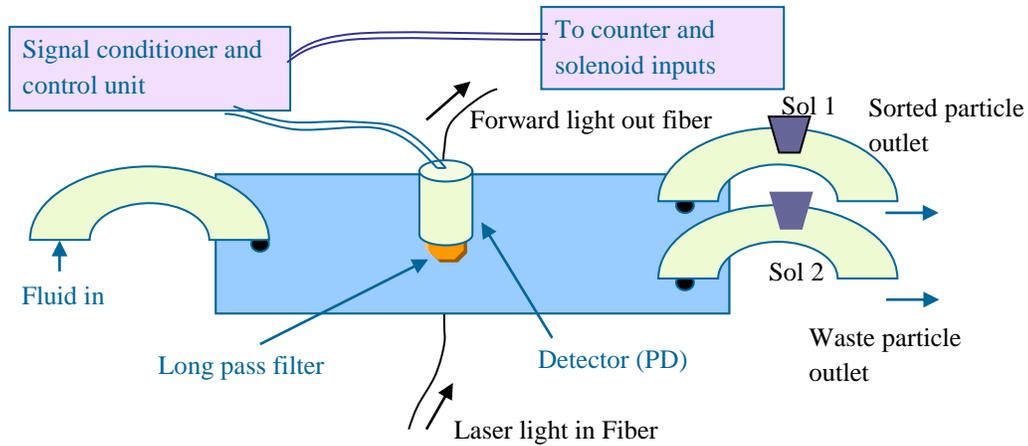
Figure 4.5: A larger view showing the coupling of laser light into and extraction of fluorescent light from the cytometer chip. The solenoid valves (Sol 1 and Sol 2) are used to switch the flow between sorted and waste bins depending on the detected signal from the photodiode (PD).

Both the prototype chips have one fluid inlet and two outlets, and, their positioning and overall sizes of the chips are same for both of them. In the final assembly of the prototype chips, as depicted in Figure 4.5, the chip fluid inlet and outlets are coupled to off-chip syringe and collection vessels through 1-mm ID polyethylene tubing. One of the outlets, the sorted outlet, is used for the target particles/cells and the other outlet, the waste outlet, is for the unwanted particles/cells. The inlet tube was 75 cm long and both the outlet tubes were each 50 cm long. One solenoid valve is placed over each of the tube outlets for controlling flow through it.

4.4. Operating principle of the microfluidic cell sorter

The operating principle of the designed miniaturized cell sorter is similar to that of the conventional bench-top cytometer. Light from a 532-nm CW diode laser is coupled into the optical fiber that delivers light to the detection region of the microfluidic channel to interrogate the biological cells/micro-particles. The scattered/fluorescent light signals from the biological cells/micro-particles are collected by a photodiode (PD) placed on the top of the observation window. An important feature of both the prototypes is that, the laser beam, fluid flow, and the PD orientations are orthogonal to each other, typical to the bench-top cytometer. A sample containing two types of biological cells/micro-particles in which one type scatters light strongly and the other type only weakly scatters light is injected into the base of the Y channel. The direction of flow into the output streams is controlled by the solenoid valves. By default, the waste stream remains open while the detected signal is low. When detected light from a cell is detected above a fixed threshold, the waste stream is closed, the sort stream is opened and the flow is directed into the cell/ particle collection stream. This is schematically shown in Figure 4.5.

4.5. Testing the functionalities of the prototypes

4.5.1. Determining response time of solenoids
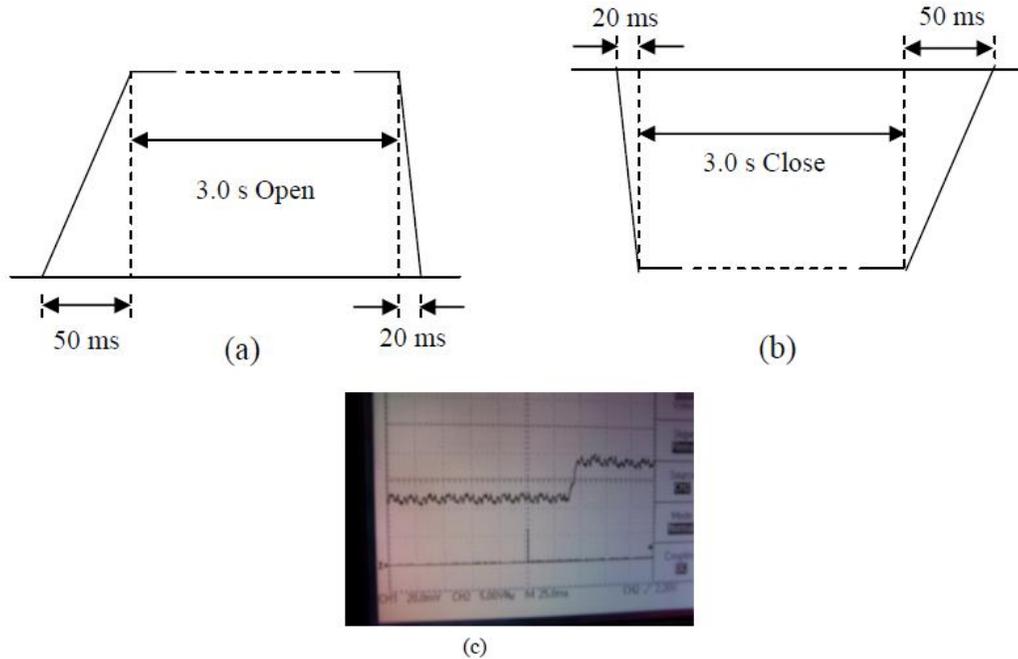
Figure 4.6: Response time (opening and closing) of Sol 1 (a) and Sol 2 (b). (c) A picture of signal transition from the oscilloscope during opening of one of the valves.

A simple technique was adopted to find the opening and closing time of both the sort and waste line solenoids (Sol 1 and Sol 2 in Figure 4.5). An LED from one side illuminated the valve opening and a PD from the other side of the valve detected its intensity. A pulse was used to trigger the solenoid and the

oscilloscope. The resulting captured signal of the PD provides the response time of the solenoid. The results are shown in Fig. 4.6.

The response time of both the solenoids Sol 1 and Sol 2 are identical, but opening time and closing time of the solenoids are different. Both the solenoids have an opening time of 25ms and a faster closing time of 10ms (considering 50% of the transition times). Again, assuming that the speed of pressure flow in water is equal to that of sound in water (~1500 m/s), it takes only 0.16 ms for the stopping pressure to flow from the solenoid to the point of separation of the channels. Thus, the throughput of the present system is limited by the response time of the solenoids.

4.5.2. Testing the functionalities of the sorter prototypes

To test the detection and sorting functionalities of the developed microfluidic prototypes, we used aqueous solutions of fluorescent latex beads of various concentrations. The illumination wavelength was 532 nm and input power was ~3 mW. A suitable long pass optical filter (cut off at 542 nm) was used additionally in between the PD and the observation window to stop background scattered light reach the PD.

We had two prototypes to be tested for their detection and sorting functionalities. Experimental details, results and discussions for both prototypes are explained separately below.

4.5.2.1. Detection of fluorescent beads: Prototype I

Experimental: In this experiment, 15µm diameter size orange fluorescent FluoSpheres® polystyrene microspheres (Molecular Probes Inc, Carlsbad, CA) were mixed with de-ionized water to make four aqueous mixtures with final concentrations of 60±3, 120±4, 160±7 and 333±7 beads/ml. Each of these mixtures was sonicated for about 2 minutes using an ultrasonic cleaner just prior to their insertion into the cytometer and a Beckman-Coulter particle counter was used to determine the concentrations of the mixtures. Each of the four mixers was injected into the cytometer prototype chip in separately by using a syringe pump, the particles were interrogated by light from a 532-nm diode laser, and emitted fluorescent signals were detected by a PD (with the optical filter placed in front of it) and counted by a counter circuit. The experimental set-up was as shown in Figure 4.5.

Results and discussions: The key results of the four detection experiments are summarized in Table 4.1. As shown in the table, although 720, 1440, 2560 and 4995 beads were run through the prototype chip in four separate experiments the PD detected only 384, 634, 940 and 1024 pulses respectively. If we assume that each detected pulse corresponded to a single fluorescent bead, then the detection efficiencies for the four samples were 53%, 44%, 37% and 21% respectively. That is, the detection efficiency decreases with the increase in bead concentration in the

sample. One possible reason for this behavior is that at higher concentrations, more beads are likely to be in the detection region simultaneously.

Table 4.1: Key results from the fluorescent beads detection experiments with Prototype I

	Sample 1	Sample 2	Sample 3	Sample 4
Concentration	60	120	160	333
Run time	1 h 30 m	1 h 30 m	2 h	1 h 52 m
Volume flow rate	8	8	8	8
volume flown through	12	12	16	15
# of beads flown	720	1440	2560	4995
# of pulses detected	382	634	940	1024
Detected pulses/min	4.24	7.04	7.83	9.14
Detection efficiency	53	44	36	20

In order to gain some insight into why the detection efficiency is less than 100%, let us consider the physical dimensions of the chip prototype. A cross-section of the chip along the optical fiber insertion channels and observation area and across the flow is shown in Figure 4.7. The thickness of the transparency polymer sheet that we used to cut the fluid and optical fiber insertion channels on it is approximately 200 µm but the diameter of the optical fiber is 125 µm and its core diameter is 100 µm. Therefore, the laser light does not illuminate the whole

cross-section of the fluid channel. The total cross-sectional area of the fluid here is 200 μm × 1.5 mm. If we neglect the divergence of the light beam coming out of the fiber, only 100 μm length of the total vertical height of the fluid cross-section would be illuminated and hence, the total illumination area would be 100 μm × 1.5 mm. The numerical aperture (NA) of the fiber is 0.22. If we take the divergence of the light beam into account, after about 220 μm away from the exit of fiber the whole vertical height (200 μm) of the fluid cross-section will be illuminated. Again, not whole of the fluid cross-section illuminated is actually sensed by the PD placed above the observation window because of the smaller size of the observation window. Considering the length of the observation window, only a part of the illumination area will be sensed by the PD above the observation window and this sensing area is 200 μm × 1 mm (considering beam divergence). This is the area of the illuminated fluid cross-section right under the observation window. Thus the ratio of sensing area to the total fluid cross section is ~67%. Thus if we assume that the velocity of fluid is uniform across the cross-section and the beads are evenly distributed in the fluid, potentially 67% of the total beads are observable with this chip prototype. However, fluid flow across the cross-section is not uniform. The actual flow profile is shown in Figure 4.8 (Obtained by solving the steady-state Navier-Stokes equations analytically for a rectangular channel flow). Integrating the flow profile over the sensing region we find that sensing cross-section is ~72% of the total fluid respectively. Thus the theoretical maximum detection (and hence sorting) efficiency achievable with this prototype is ~72%. In our experiments we set the counter circuit trigger level to 8

74

mV. One factor that could cause reduced detection efficiency is that fluorescent intensities from the beads can vary with their position in the microchannel and some of the fluorescent signals are so low that they did not trigger the oscilloscope. The other factor that could cause reduced detection efficiency is that the optical fiber was not placed at the mid-height of the fiber insertion channel.
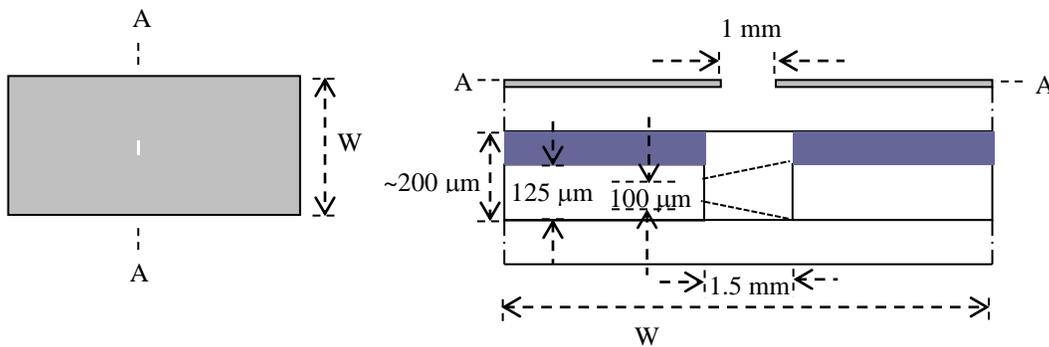
Figure 4.7: A cross-section (A-A) of the chip along the optical fiber insertion channels and observation area and across the fluid flow. Width of the fluid channel is 1.5 mm and the observation window length is 1 mm. Optical fiber diameter is 125 μm and its core diameter is 100 μm. Laser light from the illuminating fiber forms a cone-shaped illumination volume inside the fluid channel.

75
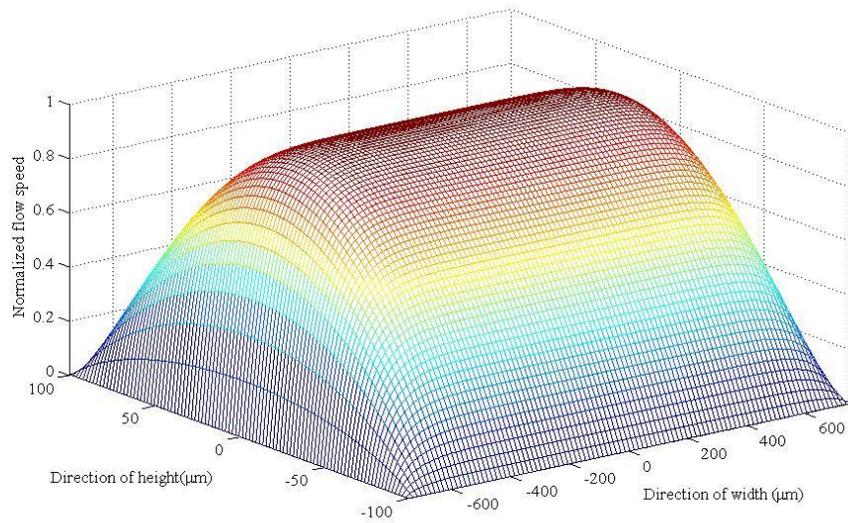
Figure 4.8: Fluid flow profile across the observation window

4.5.2.2. Sorting of fluorescent beads: Prototype I

Sample preparation: Two samples with the fluorescent bead concentrations of 60 and 120 beads/ml were prepared following the same procedure as outlined in the previous section.

Results and Discussion: Fluorescence activated cell sorting was performed with the same prototype chip. In brief, the emitted fluorescence signal was detected by a wide area PD, processed electronically and then used for switching two solenoid valves on the sorted particle and waste channels simultaneously (one to open and, another to close), forcing beads to the sort line. For each detected pulse, the sorted

channel was kept open (and the waste channel was kept closed) for 3 s to provide enough time for most of the detected beads to be sorted.

After the micro flow cytometer was run, the concentrations of beads in original, sorted and waste solutions were determined by employing the Beckman-Coulter counter. Each of the solutions was sonicated in an ultrasonic cleaner for about 2 minutes just before counting. This helped disperse the beads making the solutions uniform in concentration and reducing the clustering of beads. The key results of the sorting experiments are summarized in Table 4.2.

Table 4.2: Key results of the sorting experiments with Prototype I

	Sample 1	Sample 2
Concentration (beads/ml)	60 ± 3	160 ± 7
Volume of sorted solution (ml)	2.0 ± 0.1	4.5 ± 0.1
Concentration of sorted solution (beads/ml)	162 ± 7	288 ± 7
Concentration of waste solution (beads/ml)	49 ± 2	82 ± 3
Absolute sorting efficiency (%)	45	51
Sorting efficiency with respect to detected beads (%)	84	138

Sorting efficiency is found by dividing the number of sorted beads to the number of detected beads. As the Table 4.2 shows, the concentration of beads in the sorted solution was increased significantly for both cases while the converse

was true for the waste solution. Although the detection efficiency was decreasing with the increase in bead concentration, the sorting efficiency is showing the opposite trend. Both the detection and sorting efficiencies along with the theoretical maximum efficiency are plotted in Figure 4.9. The last row of the Table 4.2 depicts one important point that almost all the beads, which were detected by the PD, were sorted out. 138% sorting efficiency with respect to the detected beads for the Sample 2 indicates that perhaps sometimes even more than one bead was sorted out per detection pulse. This might be due to the clumping of beads with the increase in bead concentration.
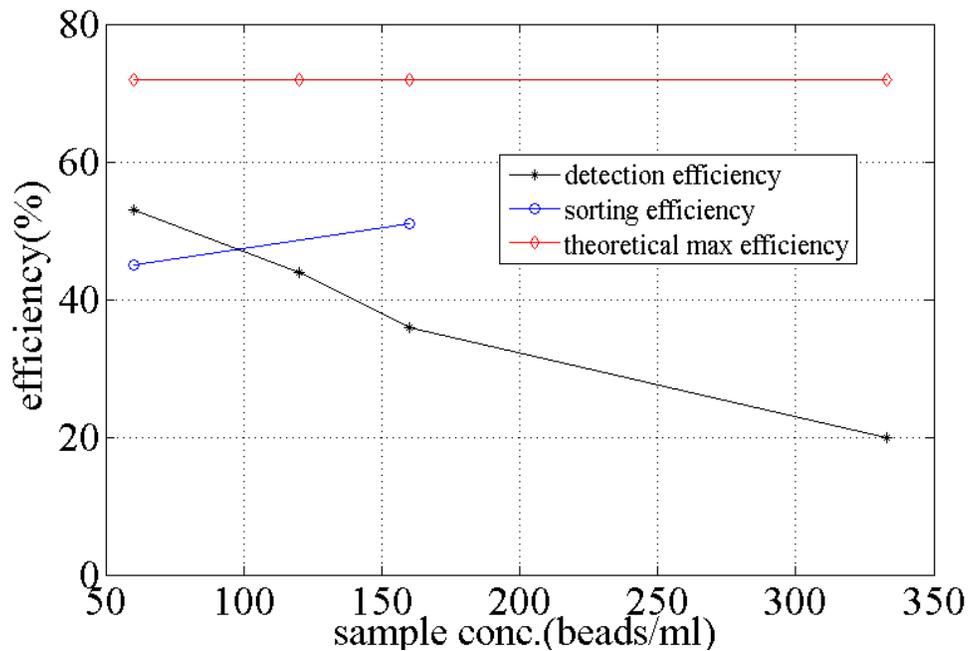
Figure 4.9: Detection and sorting efficiencies as a function of bead concentration in the sample

Currently, the theoretical maximum absolute efficiency (detection and hence sorting) that can be achieved with this chip prototype is limited by the sensing cross-section and it is found to be about 72%. The efficiency can be improved by using a more sensitive photo detector, a large diameter optical fiber and large observation window in the cytometer design. Hydrodynamic focusing can also improve the system by forcing the particles to travel in the middle of the microchannel.

4.5.2.3. Detection of fluorescent beads: Prototype II

Experimental: In these experiments, 15 µm orange fluorescent FluoSpheres® polystyrene microspheres (Molecular Probes, Carlsbad, CA) was mixed with de-ionized water to make three aqueous mixtures with final concentrations of 30, 60, and 90 beads/ml. Each of the three mixers was injected into the miniaturized chip prototype separately by using a syringe pump, the particles were interrogated by light from a 532-nm diode laser, and emitted fluorescent signals were detected by a PD and counted by a counter circuit. Each of these bead mixers was sonicated for about 2 min using an ultrasonic cleaner just before its insertion into the chip.

Results and discussion: The key results of the detection experiments with the prototype II are summarized in Table 4.3. For each of the three samples, an estimated 720 fluorescent latex beads were flowed through the chip. Because of the geometric configurations of the interrogation and sensing regions of this prototype II, only about 205 of these beads were theoretically observable (This is

explained in the later part of this sub-section). However, the table shows that the average numbers of pulses detected by the PD for these three samples are 228, 226, and 225, respectively, which is higher than the number of theoretically observable beads. If we assume that each detected pulse corresponded to a single fluorescent bead, then these numbers correspond to the detection efficiency of about 110% with respect to the theoretically observable beads. There could be two possible reasons for getting this higher number for the detection efficiency. The first, the actual illumination cross-section of the system could be greater than the geometrical illumination cross-section due to scattering of light in the observation region, and the second, the bead concentration might not be uniform across the flow, it could be higher near the central axis of the channels. We explored a little more about the first possibility and explained those in the next paragraph. We also see that the detection efficiency is almost the same for the three samples. One interesting finding here is that the detection efficiencies were much closer to theoretical prediction for Prototype II. This could be attributed to the smaller detection window of Prototype II that resulted in lower scattering light reaching the PD. So, in this case we were able to perform the detection experiments with a lower trigger voltage setting of 5 mV. Also, the concentrations of the samples used in this experiment were in the lower range of what were used with Prototype I, and, so the detection efficiency was higher.

Table 4.3: Key results from the fluorescent beads detection experiments with Prototype II

	Sample 1	Sample 2	Sample 3
Concentration (beads/ml)	30	60	90
Run time (h)	3	1.5	1
Volume flow rate (ml/h)	8	8	8
volume flown through (ml)	24	12	8
# of beads flown through	720	720	720
# of pulses detected	228	226	225
Detection efficiency (%)	31.67	31.39	31.25
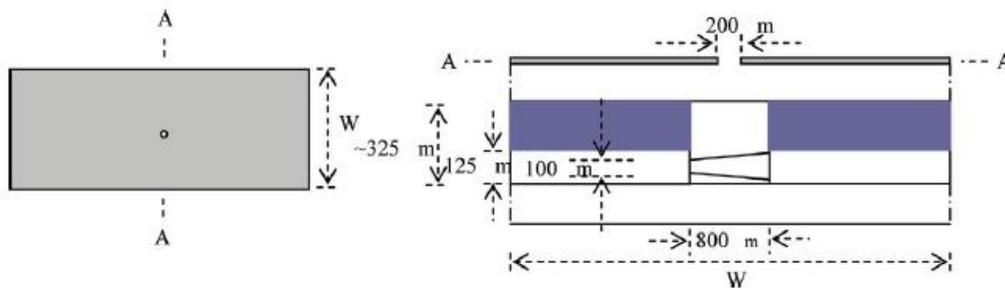
Figure 4.10: The cross-section (A-A) of the chip along the optical fiber insertion channels and observation area and across the fluid flow. Width of the fluid channel is ~800 µm and the radius of the observation window is 100 µm. Optical fiber core diameter is 125 µm. Laser light from the illuminating fiber forms a cone-shaped illumination volume inside the fluid channel.

In the previous paragraph, it was mentioned that only 205 out of the 720 beads were theoretically observable in each of the three experiments. To explain this number, let us consider the physical dimensions near the observation region of the chip, similar to the analysis we have done with the prototype I. A cross-section of the prototype II along the optical fiber insertion channels and observation area and across the flow is shown in Figure 4.10. The thickness of the Surlyn® sheet that we used to cut the fluid and optical fiber insertion channels on it is ~325 μm but the diameter of the optical fiber core is 100 μm. Therefore, the laser light does not illuminate the whole cross-section of the fluid channel. The total cross-sectional area of the fluid here is 325×800 μm^2. Again considering the diameter of the observation window, only a part of this illumination area will be sensed by the PD above the observation window. Considering the divergence of the light beam coming out of the optical fiber, following the same procedure as outlined in a previous section for Prototype II, we can determine that only ~28% of the total fluid flowed through the channel is within the sensible area by the PD. This number is obtained by integrating the flow profile across the channel over the sensible area. The sensible area is the area of the illuminated fluid cross-section right under the observation window. For the evenly distributed bead solutions that we used in our experiments, this corresponds to about 205 beads in the sensing region out of the total 720 beads. However, as mentioned earlier, the number of detected pulses was higher in each of the three experiments. This could be caused by an increase in the illumination cross-section, and hence the sensing cross-section, due to repeated scattering of light by the uneven side walls created

mainly by the UV cured epoxy in the observation region. To support this hypothesis, we theoretically estimate the number of observable beads if the channel cross-section is illuminated in its full height with a minimum width of 200 µm. We find this number to be 237 (~33% of the total fluid), which is closer to the number of detected pulses. This suggests that almost the full depth of the channel under the PD was illuminated due to scattering of light, making the actual illumination cross-section of the system much higher than the geometrical illumination cross-section, and hence the higher detection efficiency.

4.5.2.4. Sorting of fluorescent beads: Prototype II

Experimental: In these experiments, three aqueous samples with the same fluorescent bead concentrations as the detection experiments, i.e. 30, 60, and 90 beads/ml were prepared following the same procedure as outlined in the 'Experimental' sub-section of 'Detection of fluorescent beads: Prototype II' section. Then fluorescence activated cell sorting was performed with the prototype II. In brief, the emitted fluorescence signal was detected by the PD, processed electronically and then used for switching two solenoid valves on the sorted and waste channels simultaneously (one to open and, another to close), forcing beads to the sort line. For each detected pulse, the sorted channel was kept open (and the waste channel was kept closed) for 3 s. After each sample run, the concentration of beads in sorted solution was determined by visually counting the number of beads in a square cell made on a microscope glass slide under the

83

microscope. Each of the solutions was sonicated in an ultrasonic cleaner for about 2 min just before placing on the square cell. This helped disperse the beads making the solutions uniform in concentration.

Table 4.4: Key results from the fluorescent beads sorting experiments with Prototype II

	Sample 1	Sample 2	Sample 3
Concentration (beads/ml)	30	60	90
Concentration of sorted solution (beads/ml)	135	147	154
Sorting efficiency wrt detected beads (%)	88	97	104

Results and discussion: The key results of the sorting experiments are summarized in Table 4.4. The concentration of beads in the sorted solution was increased significantly for all the samples as shown in the table. It reveals another important point that, although the detection efficiency decreased with the increase in bead concentration, the sorting efficiency is showing the opposite trend. The last row of Table 4.4 depicts one important point that almost all the beads, which were detected by the PD, were sorted out. The slightly higher than 100% sorting efficiency with respect to the detected beads for the third sample indicates that perhaps sometimes even more than one bead were sorted out per detection pulse. This may be due to the fact that more beads could stick together at higher concentration and contribute to a single detection pulse.

The theoretical (geometrical) maximum efficiency (detection and hence sorting) that can be achieved with the present cytometer system is limited by the illumination and sensing geometry to be ~28%. The efficiency can be improved by hydrodynamic focusing.

The response time of both devices was limited by the solenoid switching time and it required 3 s to process a bead corresponding to approximately 30,000 beads per day. For the potential stem cell sorting application, the concentration of stem cells in blood is very low, on the order of five stem cells per microliter. Therefore, this device can potentially extract the stem cells from approximately 6 ml of blood every 24 h.

From working with these two prototypes we found that it is possible to achieve close to 100% sorting efficiency provided we can achieve 100% detection efficiency of the cells. One strategy would be to use hydrodynamic focusing to force a cell to travel in the middle of the microchannel to optimize the illumination by the laser and the detection of fluorescent light or scattering light from it.

Chapter 5

Micro-flow cytometer fabrication

5.1. Introduction

This chapter describes the design and fabrication details of the microfluidic flow cytometer that was fabricated using microfabrication tools in 'The University of Alberta NanoFab'. This design of the next generation of the micro-flow cytometer used the knowledge gained from the results of the experiments with the flow cytometer prototypes which have been explained in the previous chapter. Here the PDMS platform was used to build our microchip. PDMS is an optically transparent and soft polymer, has low toxicity and is a material that is probably uniquely suitable as a medium for the fabrication of microchambers in which to grow, manipulate and observe cells [129].

5.2. Important aspects of micro-cytometer fabrication

As mentioned earlier, there is a need for integrating all the functional blocks of an LOC system in a single chip. In this chapter, we unveil an efficient technique of integrating low-loss solid-core waveguides in an all-PDMS biochip. This technique is expected to push the realization of a true LOC system a step further.

Laser induced fluorescence (LIF) and forward scattered light or extinction are widely used optical detection methods for fluorescently labeled and label-free particle detection respectively. Most microfluidic cytometers perform fluorescence or extinction signal measurement using some form of on-chip or integrated waveguide structures. LOCs with integrated optical elements, e.g. waveguides, promise a number of important advantages, such as, reducing the size, cost and complexity of the systems, eliminating the need for the alignment of bulk optical instruments as the optical and fluidic elements can be precisely aligned with proper design and microfabrication steps, minimizing optical losses and reflections by reducing the number of interfaces [130] [131]. On-chip waveguides can be used to direct light within microns of the samples. Also, on-chip waveguide splitters and combiners allow for parallel processing of multiple samples or parameters with multiple excitation or detection points per input or output on the same chip [132]. On-chip waveguides for LOC applications have been previously fabricated using many different techniques. Use of optical fibers to deliver light into the microfluidic channels by groove assembly [133] [134] technique provides a good solution. But such technique, in our experience,

sometime cannot provide good sealing of the fiber grooves with the microfluidic channels and also the fibers are very difficult to be aligned with the microfluidic components. Another straightforward and interesting approach is to use a liquid-filled microfluidic channel as a liquid-core waveguide [135] [59]. However, it lacks structural robustness and optical stability that makes it not favorable for practical applications [136]. Concerning all these drawbacks, monolithic integration of solid-core optical waveguides with the microfluidic channel structures seems to be an attractive alternative. Typically, a planar LOC with integrated waveguides consists of a central core layer that contains the microchannels and waveguides and outside layers of lower refractive index that act as the upper and lower waveguide claddings. Taking advantage of the advanced micromachining and processing techniques already developed for semiconductor technology, waveguides in LOCs have previously been fabricated in glass and silicon by using a number of process technologies. However, recently microfluidic chips are commonly fabricated using PDMS material due to its favourable optical properties, ease of fabrication and lower cost of production. It possesses excellent physical and mechanical properties and has been widely used in microfluidic applications [67]. It is transparent in the UV−visible (230 nm to 700 nm) and selected bands of near-IR and hence is suitable for the fabrication of waveguides and other on-chip optical elements. In this chapter, a novel technique to fabricate a monolithic all-PDMS microfluidic biochip with solid-core waveguides is described. The technique is simple, inexpensive and uses commercially available PDMS materials. This technique avoids the labour-

intensive steps of filling the waveguide channels with higher index liquids, as is done in liquid-core waveguides, or higher index UV-curable resins, as is done in some solid-core waveguides.

As mentioned earlier, in a benchtop cytometer system, the detection system typically comprises of a light source, several photo detectors, waveguides, filters, and signal amplification equipment. Advances in the field of micro-electro-mechanical systems in recent decades have made it possible to develop a micro-flow cytometer with almost all of these components in it. But, such a system is inherently very expensive. It is also expected that the microfluidic chip in a point-of-care diagnostic system be disposable to prevent cross contamination between samples and therefore cost is an important issue. The cost of each microfluidic chip can be drastically reduced by keeping the light source, detectors and filters off-chip, while keeping the critical components on-chip. Once a master has been fabricated, the material cost of each chip in our system is much less (presumably less than a dollar) and a set of chips can be fabricated in less than 24 hours. The cost per analysis is simply the cost of an individual chip, or less if the chip is re-used.

In the sections below, the details of the design and fabrication of an all-PDMS opto-microfluidic flow cytometer chip with monolithically integrated planar solid-core PDMS waveguides in it are described.

5.3. Assessment of functional requirements

Before the design process is initiated, it is generally necessary for any engineering design to study and identify the functional/performance requirements of the envisioned device. This process is obviously guided by the intended applications of the device. As mentioned earlier, our aim is to develop a micro-flow cytometer for biological cells/micro-particles sorting applications. As a first step toward this, we developed two prototypes of the device and performed proof-of-concept experiments with them, the details of which are explained in Chapter 4. Based on the results of the performances of the prototypes and the general requirements of a cell sorter system we have identified the following four main functional and design elements of our next generation microfluidic flow cytometer. They are: general microfluidic flow elements, sample focusing element, micro-particle detection element and flow switching element. The design considerations to achieve these functionalities are described below.

5.3.1. General flow elements

For successful operation of the flow cytometer system, the pumping system must provide reliable and repeatable operation. It must be able to provide the desired pressure for each channel for hydrodynamic focusing function and can change the pressure rapidly for sorting function.

The selection of the size of the microchannel cross-section depends both on the size of the cells/micro-particles to be processed and the capabilities of microfabrication processing technologies available. Because of its capability to provide truly vertical (or very close to it) side-walls, the most commonly used process technology for the fabrication of PDMS master (described later) is the deep reactive ion etching (DRIE). We also chose this technology (Cryogenic DRIE) to fabricate the PDMS master for our chip. One advantage is that we can utilize our Q3D numerical model (described in Chapter 3) to predict the flow behaviour in our chip, as one of the essential requirements of the model is that the channel walls must be vertical.

5.3.2. Sample focusing element

From the results of the experiments with the prototypes, as described in Chapter 4, we know that sample focusing is very crucial to increase the detection and the overall sorting capabilities of a flow cytometer. The main function of a sample focusing element is to align the microparticles/cells near the centre of the channel in the detection region thus improving detection efficiency and sorting purity. In a benchtop cytometer, the focusing function is implemented by allowing a sheath stream to flow around the sample stream to pinch the particles in the sample stream to flow through near the centre of the combined stream. It also makes possible single-file dispensing of particles into the detection region which can be achieved by controlling the relative flow rates of the sheath and sample streams.

However, in microfluidic cytometry, fabrication of a 3D focusing element is complex and thus 2D focusing is typically used. 2D focusing is implemented by providing two side channels on the design that merges to the sample channel from both sides to focus the sample horizontally before the detection region. The width of the focused stream should be similar in size to the largest particle present in the sample stream for single file particle stream through the detection region. Individual control of each flow channel is necessary for better control of the focused stream width.

We can apply the Q3D microfluidic modeling to predict the flow behavior inside the chip in order to optimize the 2D focusing. Focusing also offers other advantages, such as more uniformity in detection signal, reduced clogging probability of microchannels etc.

5.3.3. Detection element

The detection element in a cytometer is comprised of a laser source, light delivery & collection optics and sensor. Distances of detection region from focusing and sorting zones are also important parameters. We decided to keep the source and sensor off-chip to reduce the cost of fabrication and make it viable for disposable use. Light delivery and collection optics are very crucial for the overall performance of the cytometer in terms of detection and sorting efficiencies, signal-to-noise ratio (SNR), resolution etc. In our earlier experiments with the

prototypes we found that detection and hence sorting efficiencies were low because of the small interrogation and sensing cross-sections. Also it was difficult to align the optical fibers with the main channel precisely. A micro-cytometer with integrated waveguides avoids both of these drawbacks. The interrogation and sensing geometries both can be optimized to achieve in principle 100% detection efficiency during the layout design step of the chip. Inherent alignment of the delivery and collection waveguides during the design step of the chip makes it a robust chip in terms of detection set-up. One important point to remember during the layout design is that the waveguides should be placed close enough the microfluidic channel wall to reduce the scattering and divergence of light but without making it vulnerable to potential fluid leakage from channel.

Another important point to be considered is that the distance of detection region from the focusing zone should be small enough so that the particles do not move significantly from their focused position as they reach the detection region. The same is true for the distance between detection region and sorting zone for the efficient operation of the chip. However, a minimum distance between these two points must be kept to account for the signal processing time and the response time of the flow switching system. In our prototype design, we have kept both of these distances much longer than what is adequate for proper functionality of the chip to facilitate better accommodation of the chip for experiments (for example, to conveniently place external fluidic connectors, optical filter, microscope, viewing camera etc.).

93

5.3.4. Sorting element

We opted to use hydrodynamic side flow switching system to sort the desired particles. To keep the functioning of our system simple, we targeted to only sort one type of cell (e.g. VSEL stem cell). So, the sorting element is comprised of two reservoirs: one for waste flow and another is for the target cells. One of these two reservoirs is the default destination of the main stream. So we need only one directing side flow to switch the flow from the default to the other reservoir. The driving pump of this directing flow must work in connection with the detection system to achieve this goal.

5.4. The basic architecture of the chip

The integrated chip includes hydrodynamic focusing, several waveguides for transporting light to and from the detection region and a side-flow channel for hydrodynamic flow switching. The main challenge is to integrate the solid-core waveguides into the microfluidic chip in an all-PDMS platform. The architecture of the opto-microfluidic chip for waveguide functionality implementation is shown in Figure 5.1. As shown in the figure, by sandwiching a material of higher refractive index between materials of lower refractive index, an integrated waveguide can be fabricated [57]. In this design, the chip consists of a central core layer of higher-index PDMS (Dow Corning 3-6121®) that contains the microfluidic channels and waveguides, and, top and bottom layers of PDMS of lower refractive index (Dow Corning Sylgard 184®) that act as the upper and

lower claddings for the waveguides and sealing for the microfluidic channels. In this design, the waveguide core is shielded by the air gaps from the two sides, as shown in Figure 5.1 (b).
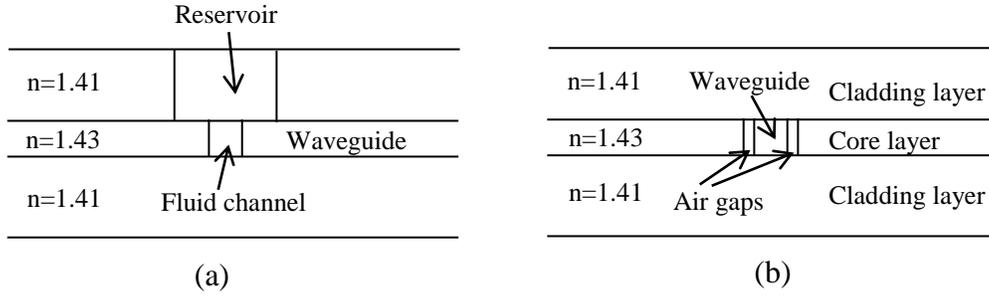
Figure 5.1: The architecture of the chip. (a) End view of a microfluidic channel, (b) end view of a waveguide showing air-gap claddings.

5.5. Fabrication overview

The integrated opto-microfluidic biochips were fabricated by using a silicon master mold replication method. In this method, the fabrication starts with the making of the silicon master. The design is produced in a commercial layout editor, L-Edit (MEMS Pro 8, CA, USA), and a Chromium mask is created on a glass substrate using a pattern generator (DWL 200, Heidelberg Instruments, CA, USA). The mask is then used to transfer the patterns of our design on to the surface of a silicon wafer by photolithography and wet etching. The areas between these patterns on the silicon wafer are then dry-etched by a deep reactive ion etching (DRIE) process. There are two ways to achieve this: CRYOGENIC

etching and BOSCH etching. Anisotropic etching of the silicon wafer utilizing the CRYOGENIC or BOSCH process in the inductively coupled plasma (ICP) machine can produce nearly vertical (~90º) sidewalls. However, compared to the CRYOGENIC process, BOSCH process offers higher etch rates but at the cost of higher sidewall roughness [137]. We choose the CRYOGENIC ICP-DRIE (Oxford Instruments) process to fabricate the channel to a desired depth of 60 µm. This process creates the positive relief structures of the microfluidic channels and the side air-gaps of the waveguides on the silicon wafer (Figure 5.2 (a)). This positive relief is referred as the master. The mold master transfers the pattern to the curable PDMS pre-polymer. A master on a silicon wafer is very durable and can be used almost indefinitely. Failure usually occurs from the user breaking the fragile silicon wafer.
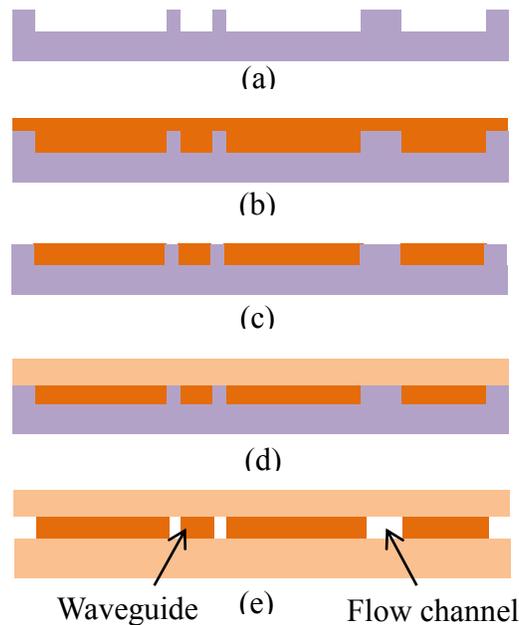
Figure 5.2: The steps of fabrication. The steps are explained below.

Once the silicon master is fabricated, the PDMS biochips are made by replica molding of the master. Replica molding is simply the casting of pre-polymer against a master and generating a negative replica of the master in PDMS. It is a monolithic process of making planar MEMS devices in PDMS. The first step of replica molding is the silanization of the silicon master to enable the easy removal of the cured PDMS layer from the master. The subsequent steps of fabricating the opto-microfluidic PDMS chips, shown schematically in Figure 5.2, are as follows.

1. A thin layer of degased liquid PDMS pre-polymer (Dow corning 3-6121, refractive index 1.43; shown in orange color in Figure 5.2 (b)) premixed with its curing agent are placed on the silicon master manually by using a Q-tip.

2. A nitrogen gun is triggered over the thin PDMS layer, especially on and around the waveguide structures, to blow out the excess PDMS pre-polymer. This expels any extra PDMS pre-polymer from the core regions of the waveguides in excess to the height of the positive relief structures for the side air-gaps (shown in Figure 5.2 (c)). This technique is supposed to improve the leakage of light from the waveguides and thereby reduce the propagation loss. The amount of PDMS pre-polymer accumulated on the other regions of the master does not have any impact on the proper functioning of the chip.

3. The master with the core layer of the PDMS pre-polymer is then kept in an oven for semi-curing at 80 ℃ for 15 min.

4. After the core PDMS layer is cured somewhat, a second PDMS pre-polymer (Sylgard® 184, refractive index 1.41, shown in pink color in Figure 5.2 (d)) is mixed with the curing agent, degased and poured on the core layer. In parallel, a similar, featureless lower index PDMS slab (Sylgard® 184, refractive index 1.41) is made on a featureless silicon wafer, which can be used for the sealing of the microfluidic channels and waveguides in the first PDMS layer once it is peeled off from the silicon master. The combined cladding-core layer and the featureless slab both can be cured together in a vacuum oven in 120 minutes at 80 ℃.

5. The combined cladding-core layer is peeled off from the master and reservoir access holes are punched through it.

6. Using the RIE machine in the NanoFab, both the PDMS layers are exposed to the oxygen plasma for 30 s for cleaning and surface activation and then brought into immediate contact and tightly hold them for some time to produce an irreversible bonding between them (Figure 5.2 (e)).

5.5.1. Deep reactive ion etching (DRIE) of silicon

Deep reactive ion etching (DRIE) is a highly anisotropic etching process used to create deep, steep-sided holes and trenches in wafers. In this work, we used the

CRYOGENIC DRIE process to produce deep, straight side walls on the silicon wafer to make the master for casting the microchannels and waveguides in PDMS. In the cryogenic DRIE process, the silicon wafer is first cooled at -110 ℃. SF_6/O_2 is used to provide fluorine radicals for silicon etching. The silicon is etched in the form of SiF_6, which is volatile. The forming of a blocking layer of oxide/fluoride (SO_xF_y) on the side walls, along with the cryogenic temperature inhibits attack on this layer by the fluorine radicals. The fluorine radicals, however, continue to vertically bombard the unmasked floor areas of the silicon wafer and etch them away [138]. In this process, we optimized the flow rates and duration of different gases to obtain an etch depth of ~60 μm with nearly vertical side walls. A SEM picture of the master is shown in Figure 5.3.
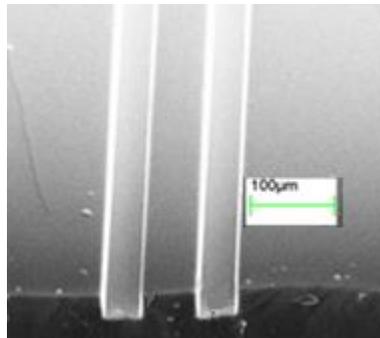
Figure 5.3: SEM image of the slot which will be filled with higher index PDMS pre-polymer to form the core of a waveguide

5.6. Design overview

We have two different designs of our chips as shown schematically in Figure 5.4. Both of these designs integrate the functionalities of hydrodynamic focusing, optical wave guiding and hydrodynamic flow switching. The only difference between the two designs is in the layout of the hydrodynamic flow focusing channels, which is discussed later in this section.

(a)   (b)
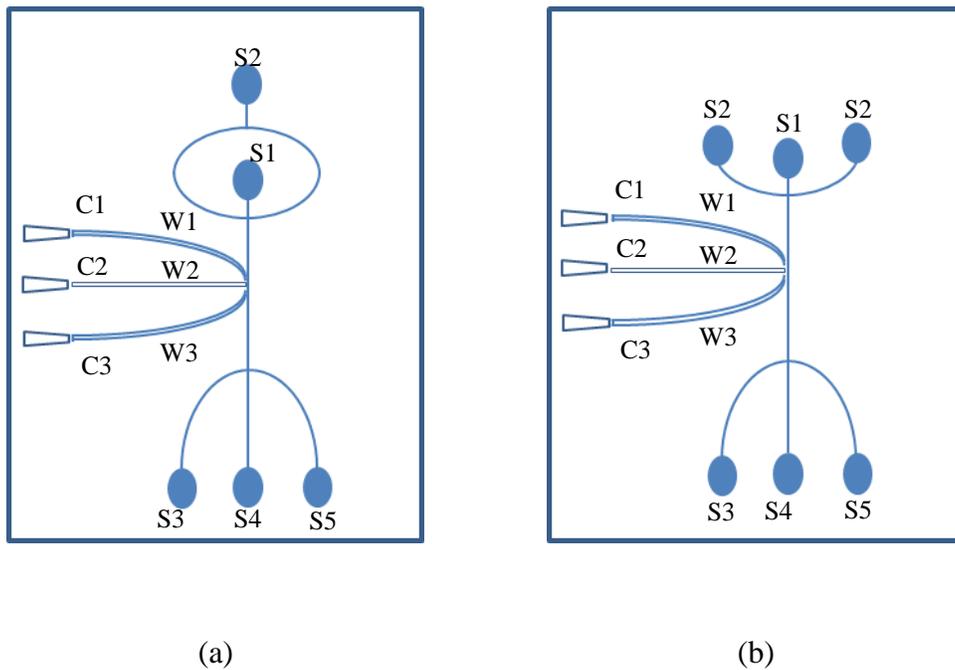
Figure 5.4: Schematic layouts of the chip designs. (a) Two sheath flow channels are merged to a single sheath reservoir; (b) Two sheath channels are kept independent to each other by connecting them to two independent reservoirs.

5.6.1. General flow channels
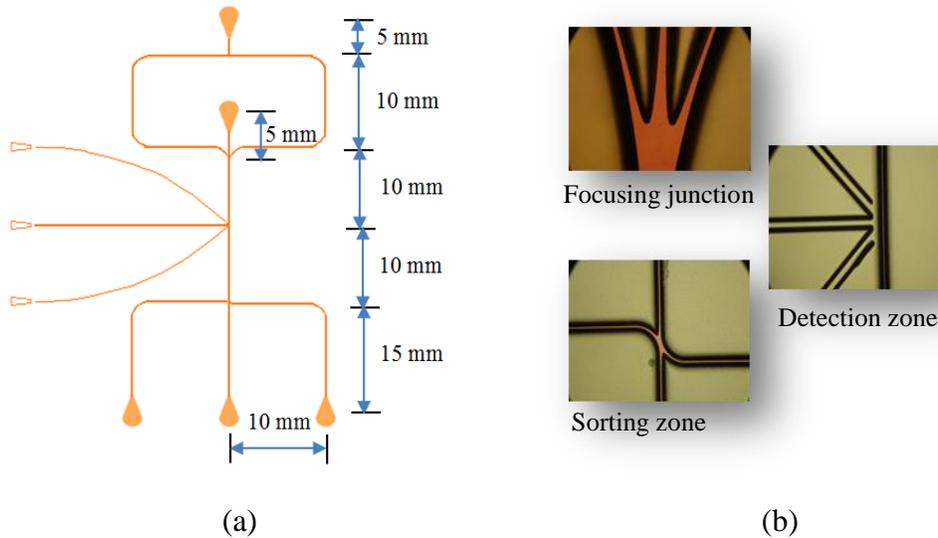
Figure 5.5: (a) The L-Edit layout of one of the chip designs along with the length labels. (b) Expanded view of the focusing, detection and sorting regions.

The original layout of one of the designs of the chip, drawn in L-Edit, with corresponding length labels is shown in Figure 5.5. As mentioned earlier, we purposely made the lengths of the channels much larger than sufficient to provide flexibilities for experiments allowing more room for placing external fluidic connectors, optical filter, microscope, viewing camera etc. The microfluidic channels connecting the sample, sheath fluid, flow switching fluid, waste particle and target particle reservoirs are all $60 \times 60 \ \mu m^2$ (W × H). These numbers are chosen based on the anticipated microparticle/cell size to be used in our experiments, which is 15 μm diameter maximum in our case, and the capability of the DRIE machine in the NanoFab. The DRIE machine in the NanoFab can etch

101

up to 65 μm depth with nearly true vertical wall. The size of the reservoirs is chosen to be 2 mm in diameter which is found to fit well with the commercially available cone-shaped plastic syringe tips for connection to external plastic tubing.

5.6.2. Sample focusing element

As mentioned earlier, we have implemented a two-dimensional hydrodynamic focusing mechanism in our chips. It consists of two identical side channels, called sheath fluid channels, merging to the main sample channel. An expanded view of the merging point is shown in Figure 5.5 (b). The two side channels create consistent sheath fluid flows near the two side walls confining the sample fluid near the centre of the channel horizontally. Two designs shown in Figure 5.4 differ only in the layout of the sheath channels. In one design (Figure 5.4 (a)), two sheath channels are originated from the same reservoir providing the option for using only one fluid control drive for the sheath fluid control. In another design (Figure 5.4 (b)), two sheath channels are connected to individual reservoir requiring two fluid control drives for the sheath fluid control. However, this design has the flexibility of controlling both sheath channels individually and thus provides better control over the focused sample stream. If there is any non-uniformity in the resistances of the two channels, which is likely in microfabrication, this later design provides better option to adjust the flows to get a better-focused sample stream.

5.6.3. Integrated waveguides

The on-chip solid-core waveguides W1, W2 and W3 are all 60×60 μm^2 (W × H) and are designed to accept light from a 62.5 μm core diameter multimode optical fiber that has a total outer diameter of 125 μm when the external jacket is peeled off. Optical fiber-to-waveguide couplers C1, C2 and C3 are designed into the chip by tapering out the waveguides at the edge of the chip to facilitate the optical fiber insertion. This coupling feature is expected to reduce the coupling loss substantially. These waveguides can be used for transporting light to and from the detection region. The ends of the waveguides near the detection region (shown expanded in Figure 5.5 (b)) in the main channel are placed in such a way that they should not interfere with one another. Also the angle between the two side waveguides at the detection region is designed at 90º. So they can be used for the side scattered light detection experiment of microparticles/cells, in which case the interrogation and detection optics are pre-aligned and built-in to the chip.

5.6.4. Sorting element

An expanded view of the sorting zone is shown in Figure 5.5 (b). Upon activation by a signal from the detection system of the sorter, the flow switching fluid from the left side channel will occupy the straight centre channel downstream thereby diverting the main stream fluid to the right sided channel.

5.7. Final product
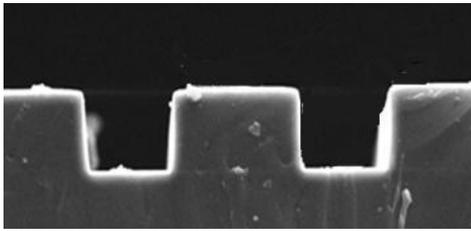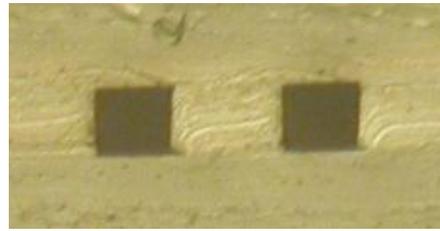
(a)   (b)

Figure 5.6: (a) The SEM image of the waveguide core and air-claddings on its two sides before the final cladding layer is bonded. (b) Snapshot of a waveguide from the side after the final cladding layer is bonded.

Figure 5.6 (a) shows an SEM image of a portion of a waveguide before the final cladding layer is bonded to it. It shows the higher-index PDMS core with lower-index PDMS cladding in bottom and two air-gap cladding on the two sides. The boundary between the two types of PDMS is invisible in the SEM picture. A snapshot of a waveguide from the side of a finished biochip is shown in Figure 5.6 (b).

We have measured the depth of the channel at several locations and found that the measurements are within a few microns around 60 μm. However, for the purpose of modeling we assumed a uniform depth of 60 μm throughout the chip.

We have utilized a steel tool to punch access holes to the reservoirs manually before the final PDMS cladding layer is bonded to the core layer. However, precise control of the tool placement is very difficult that adds to chip-to-chip variability. Also it is known that the surface properties of PDMS chips changes with time and storing condition. Normally the PDMS is hydrophobic, but due to the plasma bonding process it becomes hydrophilic. However, with time it gradually reverts to its hydrophobic state. So, the resistance of the channels to the fluids also changes with time and storing condition. So, the experiments should be planned accordingly. It is found beneficial to keep the PDMS microchannels filled with water to help retain its hydrophilic characteristics.

Chapter 6

Optical characterization of the chip

6.1. Introduction

To evaluate the performance of a flow cytometer utilizing optical detection it is important to characterize the signal-to-noise ratio (SNR) of its optical detection system. The integrated waveguides are a crucial part of our opto-microfluidic flow cytometer. So, the evaluation of the losses incurred by the waveguides is also very important for overall characterization of the chip. This chapter describes the propagation loss measurement of the integrated waveguide and SNR measurement of fluorescence light when particles of known size are flowed through the device and interrogated by a laser light.

6.2. Waveguide propagation loss measurement

The fabrication procedure outlined in chapter 5 produces planner microfluidic channels with rectangular cross-section, integrated waveguides, and most importantly, built-in excellent waveguide-to-microchannel alignment. However, higher loss in microfabricated waveguide, in comparison to its large-scale counterpart, is a concern. Waveguide losses can be separated into coupling loss, propagation loss, bending loss etc. We tried to minimize the coupling loss by incorporating a tapered coupling structure in the chip during the design step, which is explained in the previous chapter. Scattered light is emitted from the sides of the waveguide and lights it up. The scattered light is mainly influenced by the surface roughness and defects in it. Higher waveguide loss can be anticipated if the boundaries are rough. So it is directly related to the etching process used. There are some techniques that can be applied after the DRIE process to reduce the roughness of the sidewalls, e.g. the use of low concentration alkaline [139]. In this work, we did not use any method to improve the surface smoothness of the sidewalls of our master.

An important characteristic of the integrated waveguides that affects the overall performance of the system is the optical propagation loss per unit length. The standard principle that is used to measure the propagation loss of a microfabricated waveguide is that the power of the scattered light from the waveguide is proportional to the power of the confined light at each point along the waveguide [65]. The setup that we used to measure the propagation loss for our integrated waveguide is shown schematically in Figure 6.1. A picture of the

107

setup used for the loss measurement is shown in Figure 6.2. Light from a diode laser at 532 nm (green) is focused on one end of a multimode glass optical fiber (62.5 μm core diameter) using a 5× microscope objective. Light from this optical fiber is launched into the central, straight on-chip waveguide by aligning the other end of the optical fiber (jacket peeled off) with the end-polished waveguide with the help of a 3D micro-positioner. This light coupling can be improved very much by applying a drop of glycerine on to the polished waveguide end. The glycerine drop acts like an index matching fluid and thus it improves the light coupling from the fiber to the waveguide.
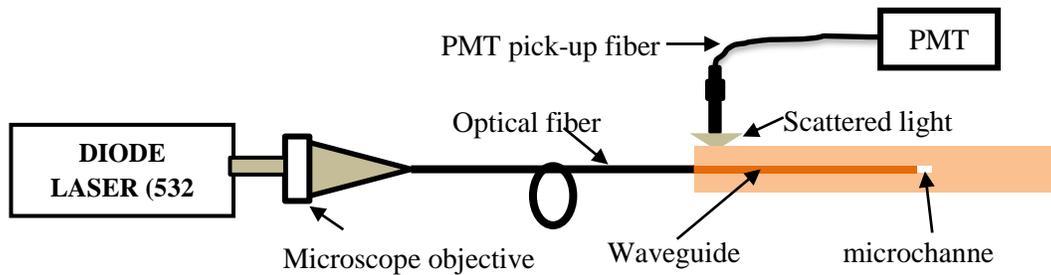
Figure 6.1: The schematic diagram of the setup used for the waveguide loss measurement
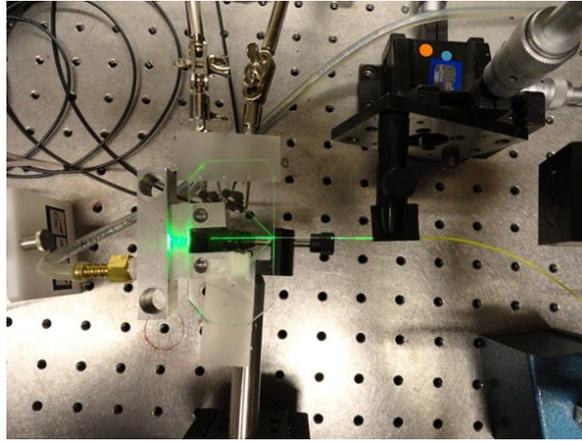
Figure 6.2: A picture of the setup used for the waveguide loss measurement

A pick-up optical fiber is mounted on top of the waveguide but not touching it to measure the scattered light. The scattered light is measured from point to point by moving the pick-up fiber along the waveguide. The pick-up fiber that we used in our experiment was a thick plastic jacket optical fiber with a core diameter of 1 mm. The scattered light was captured with this fiber at intervals of 1 mm along the waveguide and delivered it to a photomultiplier tube (PMT) detection system for measurement. The pick-up fiber was mounted on a 3D micro-positioner to allow for easy adjustment.

The same experiment was repeated for 633 nm laser light from a He-Ne laser.

(a)	(b)
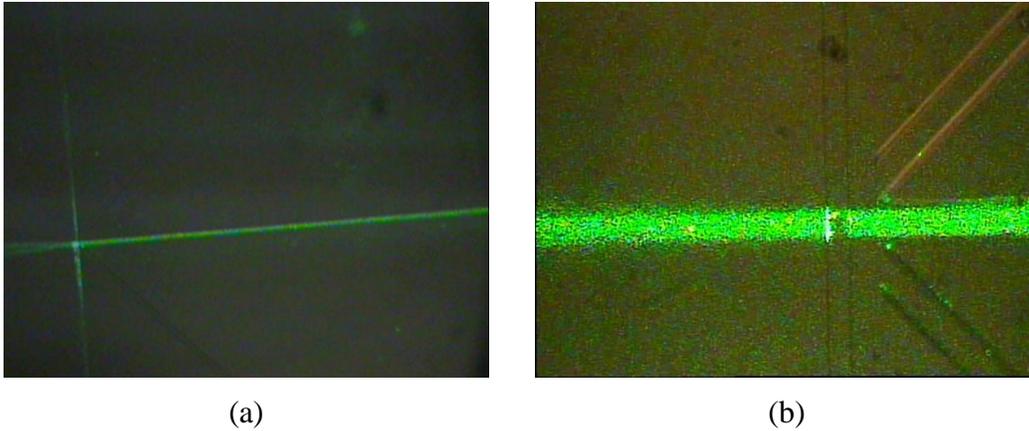
Figure 6.3: (a) A snapshot taken from the top when the waveguide is carrying

laser light; (b) Expanded view of guiding the laser light around the detection

region

The pictures of light propagating through the central waveguide in the chip

are shown in Figure 6.3. Figure 6.3 (a) shows that the laser light is confined fairly

well in the waveguide. Two extra narrow beams of light are emerged out of the

main laser beam due to coupling mismatch near the coupling point, which can be

seen in the Figure 6.2. However, this situation was improved greatly by the use of

the glycerine drop in between the fiber and the waveguide. Figure 6.3 (a) also

shows a lot of scattering along the microchannel at the end of the waveguide. This

would happen when there was no water in the channels. As the Figure 6.3 (b)

shows, this situation was very much improved with water in the channel.

Plots of the normalized intensity (in dB) of the scattered light are shown in

Figure 6.4 along with the least square linear curve fits. As shown in the diagram,

the measured propagation losses are 1.6 and 1.5 dB/cm at 532 nm and 633 nm, respectively. The results are encouraging as they are low by the integrated optics standard. A smaller propagation loss value for the red light could be due to the weaker scattering of longer wavelength wave. Most of the contemporary reports for integrated waveguides show higher or similar results for the propagation losses.
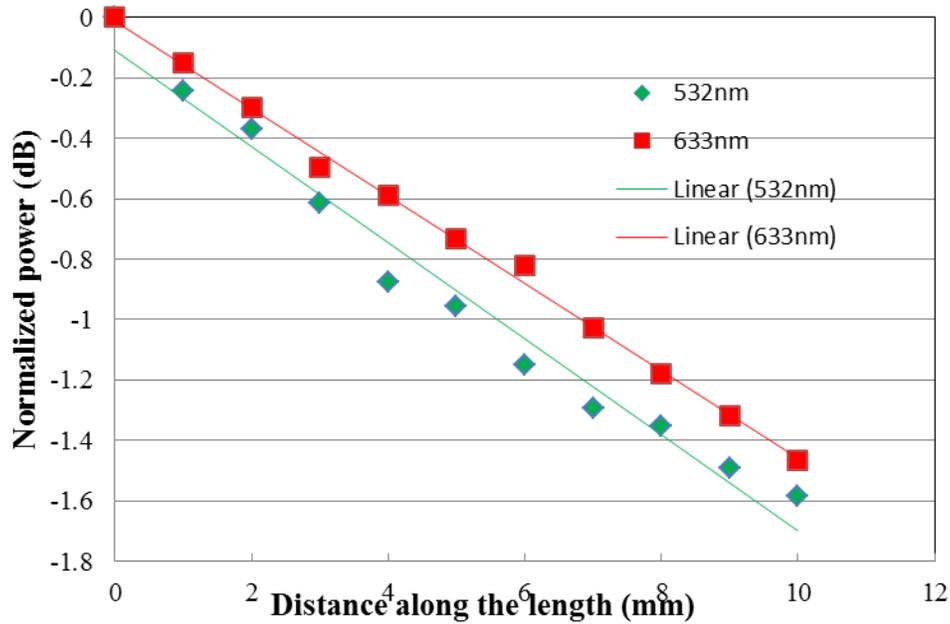
Figure 6.4: Side-scattered optical power loss in dB along the centre waveguide of the PDMS chip at 532 nm and 633 nm. Propagation losses are determined from the linear fit to the experimental data

6.3. Measurement of the signal-to-noise ratio

A performance indicator for a detection system is the signal-to-noise (SNR) ratio and it can be improved by increasing the light collection efficiency while reducing the noise of the detection system. The higher the SNR, the lower is the limit of detection (LOD), which is typically defined as the smallest sample concentration detectable with an SNR equal to 3. Because the SNR is indicative of the overall sensitivity of a detection system, we have estimated the SNR of the detection system of our fabricated chip. The experimental set up is shown in Figure 6.5. An aqueous solution of polystyrene microspheres (FluoSpheres®, 10 μm, orange fluorescent (540/560), MOLECULAR PROBES®, invitrogen™, USA) is injected into the chip through the sample inlet (the chip configuration is described in Chapter 5). DI water is pumped through the sheath inlet to focus the beads in the main channel. In this experiment, the fluid flows were controlled by the 'MFCS™' system of FLUIGENT (*http://www.fluigent.com/section/microfluidic-flow-control-products/microfluidic-flow-control-mfcs-series/*). Light from a 532 nm (green) diode laser is coupled into a multimode optical fiber (62.5 μm core dia) using a 5× microscope objective. The light coming out of the other end of the fiber was adjusted to 3 mW by using an optical power meter (835, Newport, USA). The output of the fiber is then coupled to the excitation waveguide. In this experiment, we used the central waveguide as the excitation waveguide. The light from this waveguide interrogates the fluorescent beads passing through the channel and fluorescent light is emitted by the interrogated beads. Part of this

fluorescence light is captured by the collection waveguide at an angle of 45° to the excitation waveguide and fed into a 1 mm plastic optical fiber that directs light to a PMT (R2949, Hamamatsu, Japan) equipped with a long-pass (cut-off: 542 nm) filter for the suppression of scattered green light. This set-up is shown in Figure 6.5 (a). In an alternative setup, optical detection is done from the underside of the chip without using any of the collection waveguides, by placing the 1 mm plastic optical fiber directly under the region where the micro-particles are interrogated (shown in Figure 6.5 (b)). The output of the PMT is read by a Data Acquisition Card (NI USB-6218, 16-bits, National Instruments) at a sampling rate of 50 KHz using the LabVIEW® software. The PMT gain in each setup is adjusted to such a value that even the highest detected peak does not saturate the PMT and/or the data acquisition card.

(a)   (b)
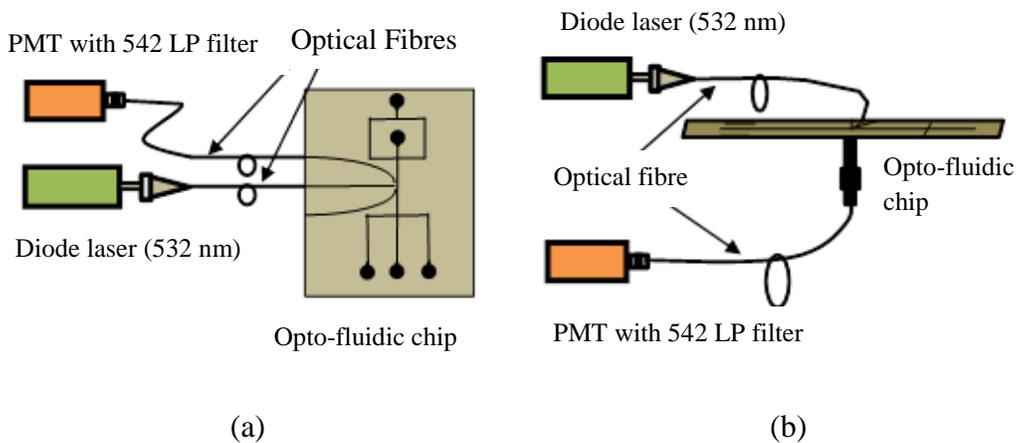
Figure 6.5: The schematic diagram for the setup of the SNR measurement. (a) Setup 1: signal is picked up through a collection waveguide; (b) Setup 2: signal is picked up by placing an optical fiber under the chip.

113
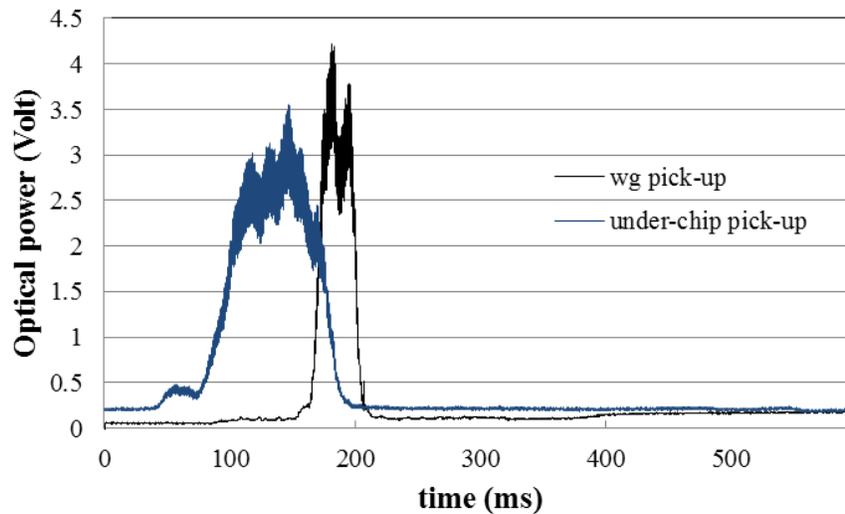
Figure 6.6: The PMT output for fluorescence from microspheres using waveguide pick-up (setup of Figure 6.5 (a)) and under-chip pick-up (setup of Figure 6.5 (b)). The two pulses correspond to two separate experiments with the sample and sheath pressure values set at 30 and 36 mbar, respectively.

Table 6.1: Comparison of the SNR and SBR obtained from the micro-flow cytometric detection experiments using waveguide and under-chip signal pick-up setups.

	Baseline (V)	Noise (V)	Average signal peak (V)	Average SNR	Average SBR
waveguide pick-up	1.11×10^{-1}	8.0×10^{-3}	6.1	765	55
Under-chip pick-up	2.08×10^{-1}	1.36×10^{-2}	5.1	374	25

Typical representative signal for each of the setups is shown in Figure 6.6. These two signals correspond to two different experiments with varying signal pick-up setup. In both experiments, the light coming out of the optical fiber was kept constant at 3 mW, the sample and sheath pressures were set at 30 and 36 mbar, respectively (3000 and 3600 Pa, respectively). The background signal (signal picked up by the detection system when there is no particle in the channel) is mainly due to the scattered green light in the chip. To compare the results of our experiments to those reported in the literature, the sampled signals of the PMT output are averaged off-line to give an equivalent sampling rate of 50 Hz. The results of the experiments for both setups are summarized in Table 6.1. The SNR is calculated by dividing the average of the background-corrected signal peak by the standard deviation of the background signal. We have also determined the signal-to-baseline ratio (SBR) for two setups, because this parameter is also used in many cases to measure the performance of a detection system. This is calculated by dividing the average of the background-corrected signal peak by the average of the background signal. The average SNR for the waveguide pick-up (Figure 6.5 (a)) and under-chip pick-up (Figure 6.5 (b)) were found to be 765 and 374, respectively. The result shows that, in terms of SNR, the waveguide pick-up performs better than the conventional way of sensing through the underside (setup 2) or the topside of the chip. The better performance of the waveguide pick-up system can be attributed to the following. A schematic diagram of the light delivery and collection geometries are shown in Figure 6.7. The numerical aperture (NA) of the collection waveguide in the horizontal plane (light is

confined   by   the   air-cladding   in   the   sideways   direction)   is

$$NA = \frac{\sqrt{n^2_{core} - n^2_{air}}}{n_{core}} = \frac{\sqrt{1.43^2 - 1.0^2}}{1.43} \approx 0.72 \text{ , whereas, } NA \text{ of the under-chip pick-}$$

up fiber is 0.5. So, the higher *NA* of the collection waveguide could lead to better

SNR for this detection setup. However, from the experiments we have observed

that the baseline for the under-chip detector is larger than that for the on-chip

detector for the same gain setting of the PMT in the two setups. This means that

the under-chip pick-up fiber collects more amount of background excitation light

compared to the collection waveguide. This could be due to the fact that because

of the larger core surface area of the under-chip pick-up fiber it will collect more

stray lights from PDMS impurity sites, surface roughness and reflections from

different channel surfaces.
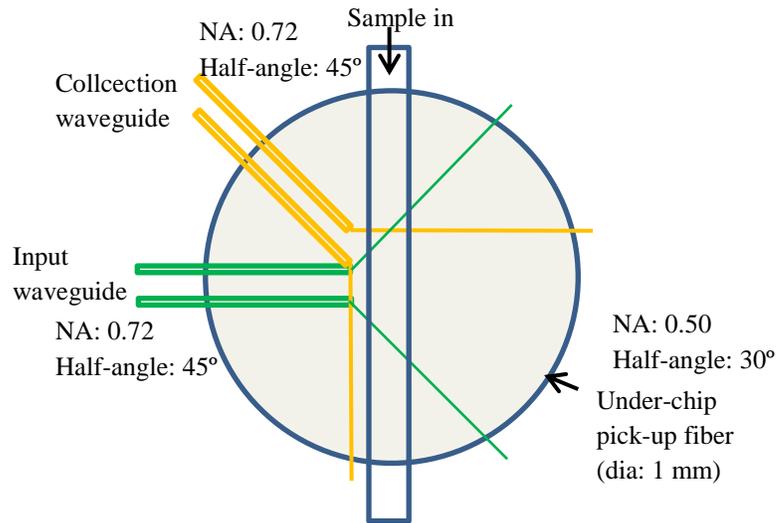
Figure 6.7: Schematic diagram showing the light delivery and collection

geometries

Our results show improvement over those reported in a similar work [65]. They reported that they achieved an average SNR of 570 ± 30 in electrophoretic detection experiments with their microfluidic device with integrated liquid-core waveguides, whereas they achieved an average SNR of 330 ± 30 with a commercial microfluidic electrophoresis system [140] that employed an underside detection approach. In their experiments they used PMT as the detector and SNR was calculated by averaging several samples together to give an equivalent sampling rate of 50 Hz, which were also the cases in our experiments.

Chapter 7

Experimental evaluation and numerical verification of the sorter performance

7.1. Introduction

This chapter describes the details of experimental performances of the cell sorter chip and the theoretical understanding of the experimental results with the help of our Q3D numerical model (Chapter 3) and the simplified circuit model of microfluidics (Appendix A).

7.2. Experimental methodology

The experimental methods for testing the flow cytometer system are relatively straightforward, but, attention to the detail of flow is very important to avoid contamination of the channels and to generate bubble-free, reproducible flow

inside the chip. To prevent the PDMS channel surfaces from reverting back to the hydrophobic state and contaminants from depositing during the storage of the chips, all PDMS chips are filled with DI water and sealed with adhesive tapes shortly after their O_2 plasma bonding process. The PDMS biochips are kept this way until they are used in the experiments and the chips are stored again in the same way after the experiments. The PDMS chips require thorough purging of their microchannels by DI water prior to and after their use in experiments to ensure residual materials from previous experiments and any trapped air bubbles are removed. Purging is carried out from each of the microchannel ends to thoroughly clean every channel of the chips. Another important procedure is that each of the micro-particle solution samples was sonicated for about two minutes using an ultrasonic cleaner prior to starting of experiments to ensure uniform particle concentration.

Volumetric flow metering, colored fluid and fluorescent particle visualization and velocity tracking were used to investigate the flow behaviour of the PDMS microfluidic chip. Hydrodynamic flow focusing studies were carried out with colored DI water prepared using commercially available food dye. Still images of the flow in the region near the focusing junction were recorded and were used to find the widths of the focused streams. The number of fluorescent particles with and without hydrodynamic focusing was counted and their velocities were determined by the time-of-flight technique. The dynamics of particle switching by the pneumatic fluid control system was studied by analyzing

video images of the fluorescent particles in the micro-flow in the region near the switching junction.

7.3. Flow calibration/characterization of the chip

We studied two methods to characterize the flow behaviour of our fabricated biochip: volumetric analysis and fluorescent particle speed measurement. We compare our experimental results to those calculated using the Q3D model. As we have mentioned in an earlier chapter, the flow control is accomplished using the 'MFCS™' system of FLUIGENT (*http://www.fluigent.com/section/microfluidic-flow-control-products/microfluidic-flow-control-mfcs-series/*). It has four pneumatically controlled channels whose pressure outputs can be controlled independently and dynamically by using LabVIEW script. Pieces of elastic tubes of 12 cm length each (ID: 1mm/OD: 3mm) are connected at the end of each channel. The connections between these tubes and biochip ports are accomplished via plastic syringe tips which are cut at the appropriate sizes to fit into the ports tight enough to provide leak-free fluid delivery in and out of the biochip.

7.3.1. The flow control system: 'MFCS™' of FLUIGENT

The MFCS stands for the 'Microfluidic Flow Control System'. Different types of MFCS are available commercially. The one that we used in our experiments was a 4-channel 69 mbar/500 mbar MFCS. Figure 7.1 shows a photo of the MFCS used as the flow controllers in all of our flow experiments. It is composed of four

pressure driven flow controllers with an independent and dynamically controllable output pressure range of 0-69 mbar. The system input is a 500 mbar pressure source. It is also possible to operate this unit with a vacuum source input. It can easily be accessed by a USB cable and controlled by a LabVIEW script on a PC for dynamic control of the pressure channels. It can also be controlled by a dedicated microcontroller for better response time of operation. Unlike the automatic syringe and peristaltic pumps, it provides pulseless flows with highly stable flow rates. According to manufacturer's test results it provides a flow stability of <0.1%, a response time of ~35 ms and a flow rates from sub nl/min to hundreds of ml/min. The pneumatic pressure supply pathways of the MFCS are shown in Figure 7.2.
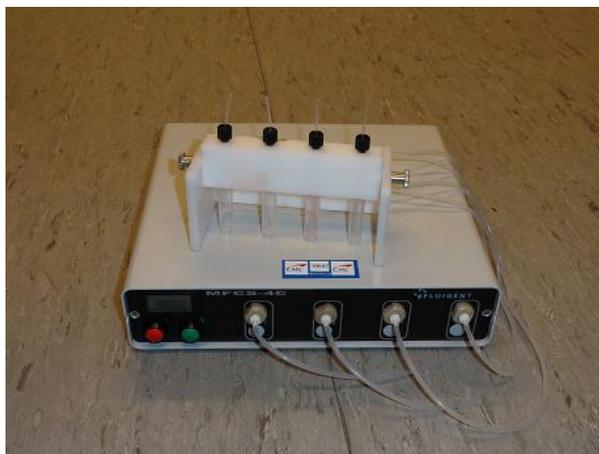
Figure 7.1: A photo of the MFCS from FLUIGENT used as the flow controller in the experiments

121
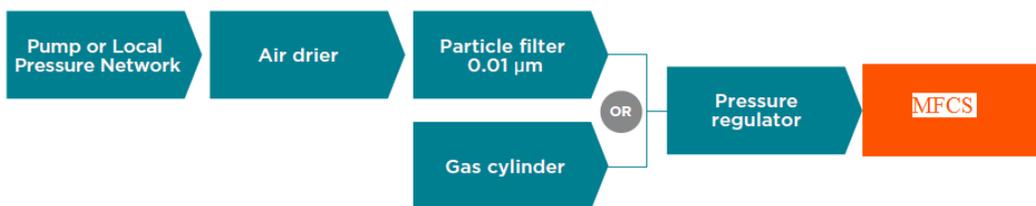
Figure 7.2: The pneumatic pressure flow in the MFCS system

7.3.2. Flow characterization: volumetric analysis

The chips used in the flow characterization experiments have the two sheath flow channels merged together to make a single sheath inlet. Initially the complete flow system is cleaned by pumping DI water through it by using the 'purge' function of channel 1 of the MFCS. It is to be mentioned here that only channel 1 of the MFCS has this purging capability and all 500 mbar pressure would apply to channel 1. After the complete flow system is purged and cleaned, channel 1 is connected to the sample inlet of the chip and the 'purge' function of this channel is again kept on for a sufficient duration of time so that the whole microchannel system of the chip is filled with DI water without forming any air bubble in it and sufficient water comes out of each of the remaining ports of the chip and typically a drop of water semi-spherical in shape with diameter of ~3mm would form at the ports. Now another channel of DI water (e.g. channel 2) with the DI water dripping out of its plastic tip is inserted very carefully into the sheath flow inlet (S2 of Figure 5.4 (a)) through the drop of water over it minimizing the formation

of air bubbles. This procedure would lead to the formation of a continuous path of liquid between the channels 1 and 2. Similarly another pressure channel (e.g. channel 3) is connected to the outlet of the straight channel (S4 of Figure 5.4) forming continuous liquid paths among the channels 1, 2 and 3. Now the other two ports of the biochip (S3 and S5 of Figure 5.4) are sealed with adhesive tapes. Once that a bubble-free, continuous flow system is established, the required flow conditions for the experiment are established by setting up the desired pressure in each channel through the control software.

Although the flow was supposed to stabilize in a few ms (according to manufacturer's data, response time: ~35ms), we waited for about a minute to give enough time for the stability of the flow. Having established the stability of the flow, the experiment proceeds by collecting the liquid flowed through the chip at the output vial (connected to channel 3) for some duration of time. Duration of flow is measured by a stop watch. The stop watch is started right at the moment when a drop comes out of the outlet plastic tubing (this drop is not collected in the outlet vial) and stopped whenever the last collected drop drips into the vial. The weight of the outlet vial is taken before and after the collection of the flowed DI water by an electronic weighing machine (Mettler PC 180) which has a weighing resolution of 1 mg. Flow speeds are calculated based on the weight of the collected liquid and the dimension of the microchannel. Table 7.1 summarizes the experimental results.

Table 7.1: Summary of the volumetric flow measurement results

Mainstream pressure (mbar)	Sheath pressure (mbar)	Duration of flow	Starting weight (gm)	Final weight (gm)	Volume flowed (ml)	Average speed (mm/s)
5	5	205m 27s	1.238	1.288	0.05	1.13
10	10	186m 52s	1.236	1.326	0.09	2.23
20	20	29m 48s	1.311	1.338	0.027	4.19
30	30	41m 32s	1.235	1.296	0.061	6.8
40	40	30m 02s	1.258	1.31	0.052	8.02
50	50	160m 25s	1.234	1.656	0.422	12.18
60	60	29m 45s	1.237	1.326	0.089	13.85
70	70	30m 02s	1.238	1.342	0.104	16.03

As a sample calculation, at sample and sheath pressure setting of 30 mbar, total volume flowed through the chip for a duration of t=41 m 32 s=2492 s is v=0.61 ml. So, the average flow speed at the main microchannel (from the start of focusing to the sorting point of the chip) is, $s = \dfrac{v}{xt}$ = 6.8 mm/s, where, x is the cross-section of the main microchannel which is equal to 60×60 μm^2.
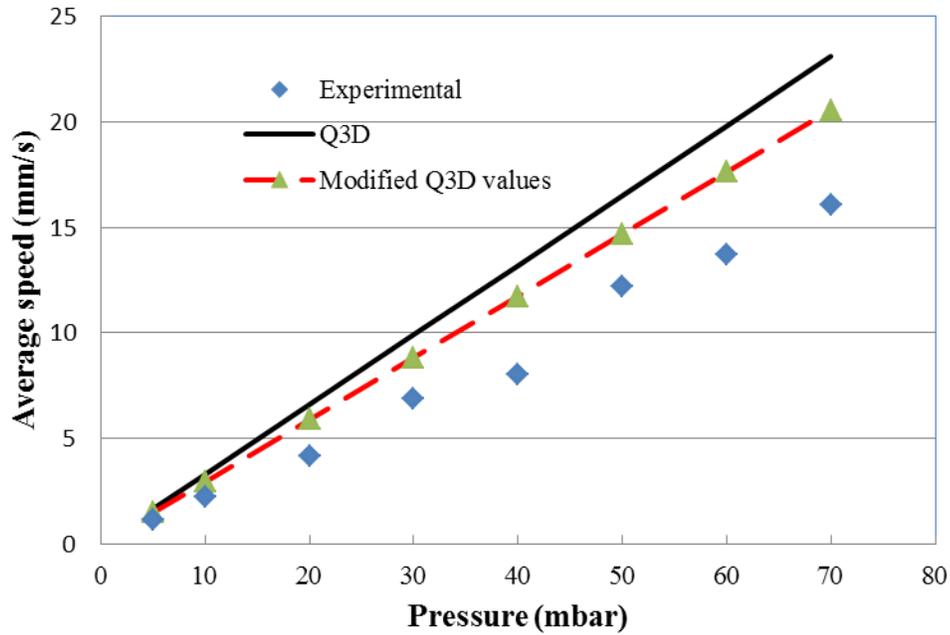
Figure 7.3: Experimental and numerical average flow speed of DI water in the main channel of the chip as a function of the pressure applied to the sample inlet. The modified Q3D values are calculated taking into account the change in the effective cross-sectional area due to non-perfect vertical walls and the effect of input/output tubing. The pressure at the sheath inlet was kept at the same value as that applied at the sample inlet.

The average flow speed of DI water in the main channel of the chip as a function of the applied pressure in the sample inlet is shown in Figure 7.3. The flow rate of the DI water as a function of the applied pressure would have the same trend as the average flow speed shown in Figure 7.3. It is to be mentioned here that with the change of the pressure applied to the sample inlet (channel 1), we also changed the pressure applied to the sheath inlet (channel 2) to the same

value as the sample inlet. Figure 7.3 also shows the corresponding numerical results from the Q3D model of the biochip. As seen from this figure, the differences are quite significant, especially at the higher pressure values. To address this discrepancy we have investigated the effect of several factors that might have possible contribution to this error[4]. They are: change in the effective cross-sectional area of microchannels from its ideal value of $60 \times 60 \ \mu m^2$ due to non-perfect vertical channel wall, evaporation of DI water during the experiments, neglecting pressure drop in the plastic tubing between the pressure channel and biochip ports etc. We have measured the inclination angle of a channel wall of our chip to be about 87°. It is estimated that this would reduce the effective cross-sectional area of the channel by about 5%. So the flow velocity would be reduced by about 5% if we take this into account. By using simplified circuit model of microfluidics, we estimate that the flow velocity will be further be reduced by about 6% if the pressure drop in the plastic tubing is considered in the calculation. This estimation is carried out for two pieces of plastic tubing at sample and sheath inlets and one at the outlet (length and diameter of each are 12 cm and 1mm, respectively). The numerical predictions corrected for these two factors (a total of 11% reduction in the original Q3D values) are shown as the dotted line in the Figure 7.3. As we have mentioned earlier we have collected the liquid at the outlet in a sealed vial. It is likely that the loss due to evaporation would be small. So it is neglected here until further study is carried out. Even after the corrections are

---

[4] Uncertainties due to weighing and pressure are estimated to be very insignificant to the difference

made to the numerical values, the differences in experimental and the modified values are big in higher pressure values. At this point we assume that there must be a factor that reduced the effective pressure applied to the chip inlets proportionately during the experiment, e.g. a leakage in the air or liquid plumbing system. Further study is needed to address this issue.

7.3.3. Flow characterization: Fluorescent particle tracking

An alternative method of calibrating the flow inside the chip is to inject fluorescent plastic microspheres in the micro-flow and measure their speeds using the time-of-flight technique. The speed distribution of the fluorescent microspheres can be determined by measuring their transit times between two points of known distance (8 mm) in the channel. A snapshot of the set-up of this experiment is shown in Figure 7.4(a) and a schematic diagram of the set-up is shown in Figure 7.4(b). An aqueous solution of fluorescent microspheres is inserted into the sample inlet. We used 10μm diameter size orange fluorescent FluoSpheres® polystyrene microspheres (Molecular Probes Inc, Carlsbad, CA). The solution should be sufficiently dilute (less than 14,000 particles/ml) so that there will be no more than a single bead on the average at a time between the inlet and outlet in the main microchannel. The experiment is conducted both with and without the sheath flow. The sheath inlet is fed by a DI water source as usual. The particles are interrogated by two laser beams at two points of the main channel; at the detection region of the chip and at another point downstream 8 mm apart. The

emitted fluorescent signals are collected by two optical fibers (1 mm dia core) placed under those two regions and are fed to two photodetectors each equipped with 542-nm long-pass filter for the suppression of green light. In our experiments we utilized two 532-nm diode lasers for interrogation and two PMTs for emission detection. The transit time of a fluorescent microsphere was recorded by using an oscilloscope.

(a)   (b)
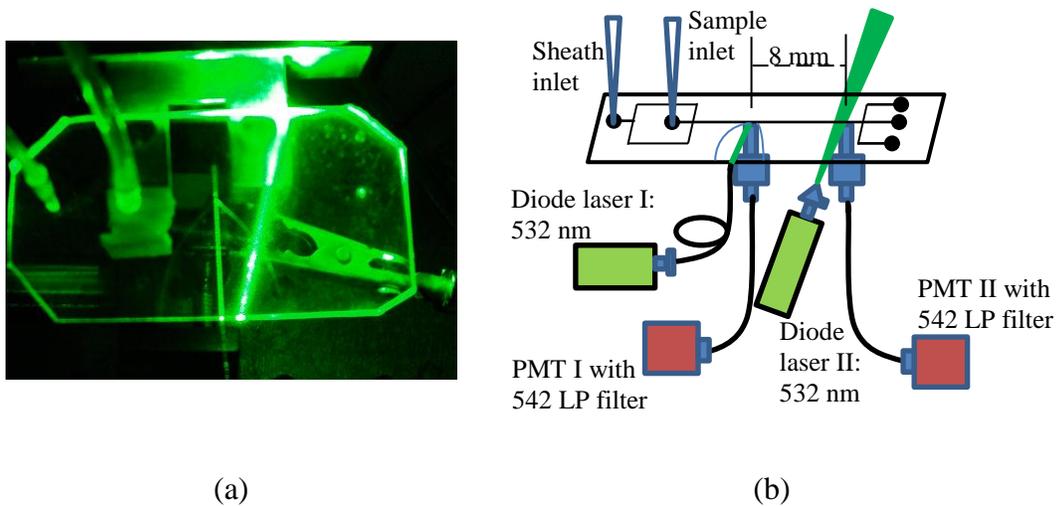
Figure 7.4: The set-up for the measurement of transit time of fluorescent particles. Particles are interrogated at the detection region of the chip by a laser beam through the central waveguide and at another point downstream by another laser beam focused through the chip without any waveguide. (a) a snapshot of the set-up; (b) schematics of the set-up

The snapshot of a representative pair of signals from the two PMTs for a single particle transit is shown in Figure 7.5. Transit time is measured from the

timing of occurrence of two signal peaks of a single particle transit by using the time scale of the oscilloscope.
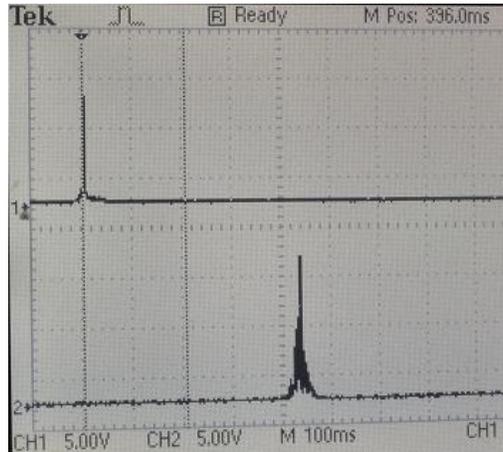
Figure 7.5: A signal pair from a single particle transit through the microchannel. They are captured by two PMTs placed a known distance away under the main microchannel of the chip. Transit time is measured from the difference of occurring of two signal peaks. This picture corresponds to the flow conditions of sample and sheath pressure values of 50 and 65 mbar, respectively.

The velocity distributions of microspheres without and with flow focusing are shown in Figure 7.6(a) and 7.6(b), respectively, for sample and sheath pressure of 50 and 65 mbar, respectively. Each of these figures is drawn for the same number of total particle count of 46 for comparison purpose. If we assume that the particle concentration inside the microchannel is uniform, then we can determine the average speed of the flow by taking average of the velocity

distribution. However, for the flow with focusing this is definitely not the case, as particle concentration is not uniform across the flow. So, we determine the average flow speed without focusing and the results are plotted in Figure 7.7 as a function of pressure at sample inlet. An estimated error of ±10% is added to the experimental values to account for the uncertainty in the measurement of distance between two observation points and timing reference measurement in the oscilloscope. Figure 7.7 also shows the Q3D calculated values and the modified Q3D values that account for the effects of non-perfect channel wall (~5% reduction) and pressure drop in the inlet tubing (~1% reduction). The figure shows that at lower pressure values (up to 30 mbar), the experimental values agrees well with the numerically calculated values within the estimated uncertainty. However, at 40 and 50 mbar pressure values, the experimental values are well above the calculations. One important effect that may cause this discrepancy is the lateral migration of particles due to wall effect and pinching effect in a microchannel flow [141] [142]. The particles near the wall of the microchannel are pushed towards the centre due to the wall effect and the particles near the centre are pushed towards the wall due to the pinching effect (except the particles that are exactly at the centre of the microchannel). Y W Kim and J Y Yoo [141] showed that lateral particle distribution is highly influenced by the channel-to-particle size ratio and the flow velocity. They mentioned that channel-to-particle ratio should be less than 20 to stimulate particle migration. They also showed that at lower speed values (low Reynolds numbers), the migration due to wall effect is much more prominent than that due to the pinching

(a)   (b)
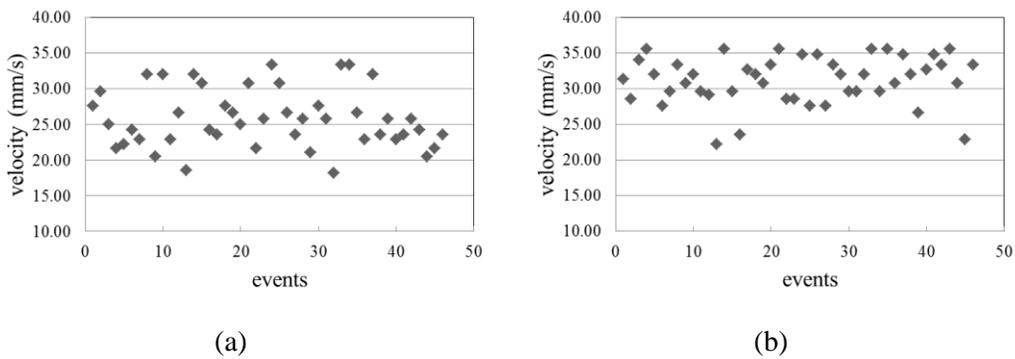
Figure 7.6: micro-particle velocity distributions: (a) Particle velocity spectrum without hydrodynamic focusing; (b) The spectrum with the hydrodynamic focusing. Here sample pressure was 50 mbar and sheath pressure was 65 mbar, number of particle in each case is 46.
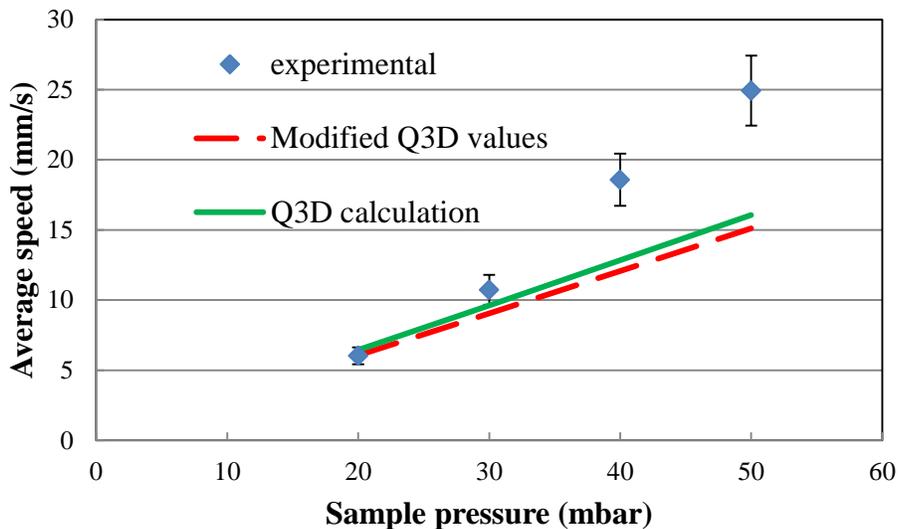
Figure 7.7: Average flow speed calculated from the velocity distribution of fluorescent particle and numerical average flow speed as a function of sample pressure. The modified Q3D values are calculated taking into account the change in the effective cross-sectional area due to non-perfect vertical walls and the effect of input tubing.

131

effect and that the migration increases with the flow velocity. In our system, channel-to-particle ratio is only 6, so at higher pressure values (still at low Reynolds numbers) particle distribution across the channel cross-section does not remain uniform due to lateral migration of particles away from the walls (wall effect). That's why our experimental average speed is higher than the Q3D calculated values. Further study needs to be done so that the particle dynamics can be added to the Q3D model for complete understanding of the results.

The particles flowing through the centre of the channel do not migrate laterally due to zero net pinching force at the centre of the channel [142]. So, after conducting each of the runs of this experiment for long enough duration to pass significantly large number of particles (typically about 50 particles in our experiments) through the microchannel, the speed of the fastest moving microsphere/microspheres can be assumed to be the maximum flow speed. Experimental maximum flow speed (speed of fastest moving particles) and Q3D calculated maximum flow speed at the main microchannel of the chip for the flow with focusing are summarized in Table 7.2.

As the table shows, the experimental maximum particle speeds agree reasonably well with the maximum flow speed calculated by using the Q3D model. A plot of the experimental and Q3D model numerical results as a function of the sample pressure is shown in Figure 7.8 for quick comparison. This figure also shows the modified numerical values that account for the effects of non-

perfect channel wall (~5% reduction) and pressure drop in the inlet tubing (~3% reduction) In this comparison, we are neglecting the particle-induced hydrodynamic disturbances of the fluid flow in numerical model, as the particle concentration of the samples used in the experiment was very small [143]. As the plot shows, the difference between the numerical model and experimental results decreases as the applied pressure increases.

Table 7.2: Comparison of the results obtained from the fluorescent particle tracking experiment of flow with hydrodynamic focusing and Q3D model simulation

Sample pressure (mbar)	Sheath Pressure (mbar)	Experimental max speed (mm/s)	Q3D model max speed (mm/s)
20	23	10.4	14.2
30	36	18.7	21.5
40	50	26.8	28.8
50	65	35.6	36.4
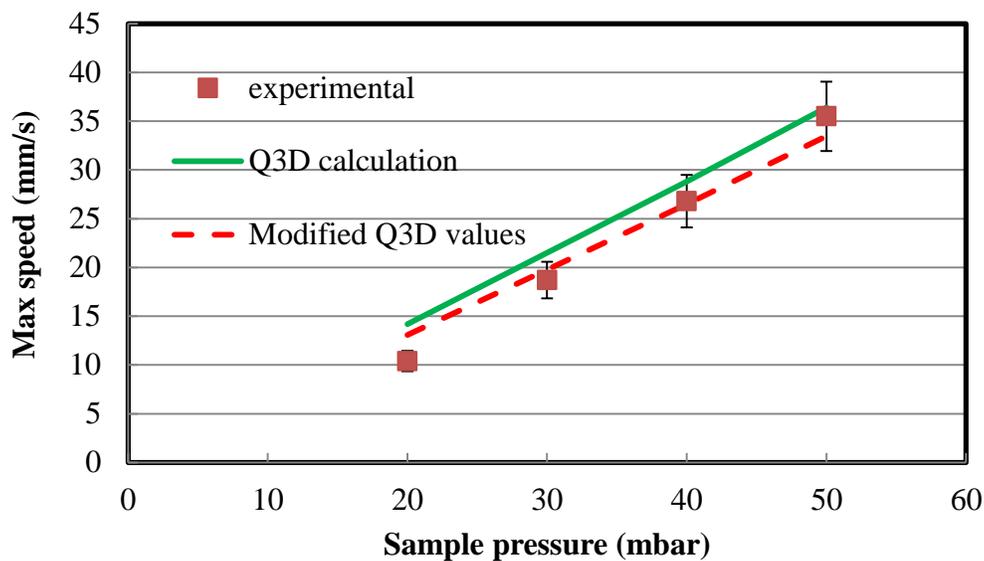
Figure 7.8: Maximum flow speed in the main channel of the chip as a function of the pressure applied to the sample inlet. Modified profile accounts for the change in the effective cross-sectional area due to non-perfect vertical channel walls and inlet tubing resistance

7.4. Evaluation of the flow focusing functionality of the chip

Characterization of sample focusing functionality is very important as it is mentioned in an earlier chapter that it is one of the four crucial building blocks of a cytometer system. The purpose and functionality of sample focusing has been described in the earlier chapters (Chapter 2 and 5). This section describes the experimental procedure to determine the width of the focused stream in the fabricated PDMS biochip summarizes the results and compares them with the

Q3D numerical results. The effect of focusing on the velocity distribution of the microspheres has been investigated and is discussed at the end.

7.4.1. Experimental estimation of focused stream width

(a)	(b)
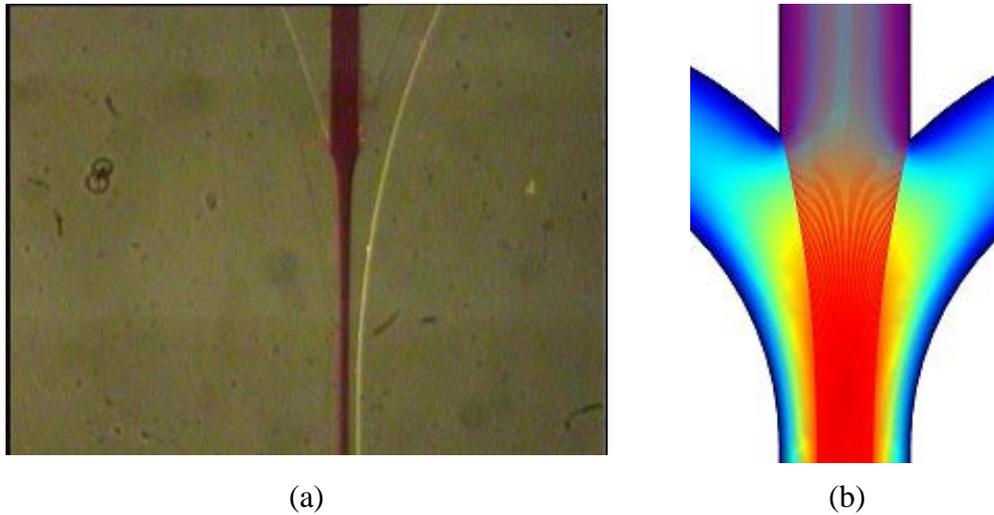
Figure 7.9: (a) A snapshot of flow focusing with sample pressure of 50 mbar and sheath pressure of 65 mbar. (b) corresponding Q3D numerical model of focused flow

A very simple approach is used to visualize the hydrodynamic flow focusing in our chip and to determine the width of the focused stream. Colored DI water (prepared first by mixing commercially available food dye with DI water and then filtered using a 0.1 μm filter) is flowed through the sample inlet and normal DI water is flowed through the sheath inlet of the chip. All the steps are carried out to

ensure a clean and bubble-free flow through the chip, as mentioned in the previous experimental procedure in the section 7.3.2. After the flows are stabilized (typically after 2 mins), still images of the channel flows in the region close to the junction of the sample and sheath channels are acquired with the microscope CCD camera image acquisition system and studied with the help of MATLAB to find the widths of the focused streams. The images are taken very close to the junction to reduce the effects of diffusion of colored fluid into the sheath. A snapshot of the flows with focusing is shown in Figure 7.9(a).

As the flows are laminar, it is expected that sharp boundaries exists between the sample and sheath fluids and the dividing streamlines between them define the focused stream width. The main difficulty in determining the exact location of these dividing streamlines is that the diffusion of food color across this boundary results in a color intensity profile across the flow that is not perfectly rectangular and hence does not directly provide these streamlines. To reduce the effects of diffusion in the measurements, we run this experiment with the highest possible flow rates for the sample and sheath fluid (sample pressure was kept constant at 50 mbar and sheath pressure was varied from 40 to 65 mbar), we took the snapshots of flows as close to the starting of focusing as possible and we used the full-width at half-maximum (FWHM) approach to estimate the width of focused stream from the color intensity profile of still images of focused streams across the flow. The FWHM value is the width of the sample profile that corresponds to the locations where the color intensity is half of the maximum

profile intensity. This is only an approximation of the actual focused width. The diffusion of the dye particle in the transverse direction affects the profile width. So the focused stream width found using this method depends on the sample and sheath fluids and the location where the profile has taken. As we have mentioned earlier, we estimated the focused stream width at about 1 *mm* from the junction to minimize the effect of dye diffusion. The plot of the dye color profile across the focused flow for sample and sheath pressure values of 50 and 65 mbar, respectively, is shown in Figure 7.10. The plot shows the FWHM estimation of the focused stream.
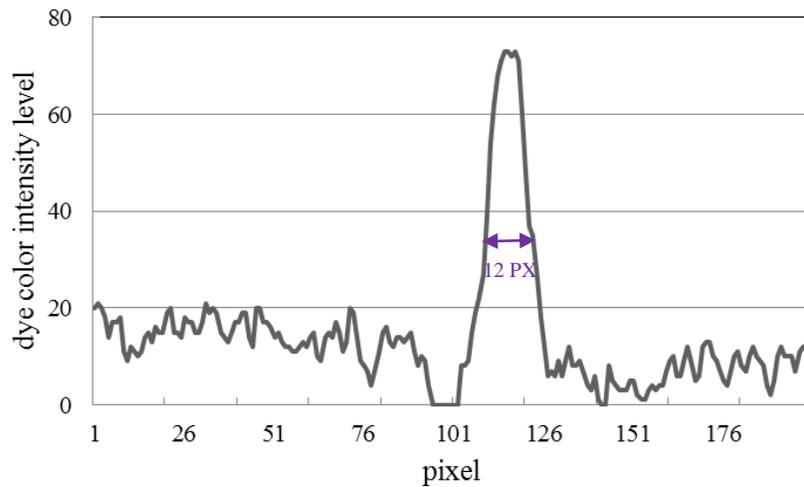
Figure 7.10: Intensity level plot of the dye color across the flow in the main microchannel at about 1 mm from the junction. Pressure setting was 50 and 65 mbar in the sample and sheath inlets, respectively. The FWHM estimation of the focused stream width is 12 pixels (26.67 μm). The corresponding width of the total flow cross-section was 27 (60 μm) pixels.

The focused stream width estimated using the FWHM approach along with the values obtained from the Q3D model simulation (shown in Figure 7.9(b)) is plotted in Figure 7.11. The values from FWHM estimation lie within *5%* of the Q3D numerical predictions. The exact width of the focused stream can be determined by de-convolution from knowing the diffusion coefficient of the dye solution. Further study is needed to implement this.
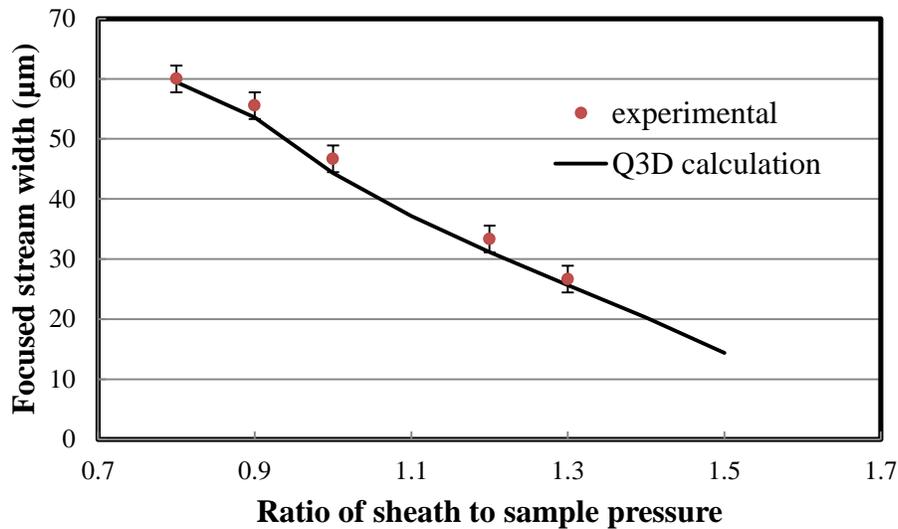
Figure 7.11: comparison of the estimated FWHM focused stream width with the Q3D model values

7.4.2. Effect of focusing on particle velocity distribution

The velocities of microspheres through the microchannel with and without the sample hydrodynamic focusing are determined using the fluorescent particle

tracking set-up as described in the sub-section 7.3.3. The velocity distributions of microspheres without and with flow focusing are already shown in Figure 7.6(a) and 7.6(b), respectively, for sample and sheath pressure of 50 and 65 mbar, respectively. As we can see from the figures, due to the flow focusing, more particles were moved to the higher range of the velocity spectrum. This can be seen from the Figure 7.12 that compares average velocity as a function of pressure for the two cases. As the sample flow is squeezed by the sheath flow the particles in the sample flow are pushed towards the centre of the flow stream led to a higher velocity. As the figure shows, the average speed increases and standard deviation decreases with the hydrodynamic focusing. However, some particles were not moved to the higher velocity regime, as our chip only provides a 2D hydrodynamic focusing.
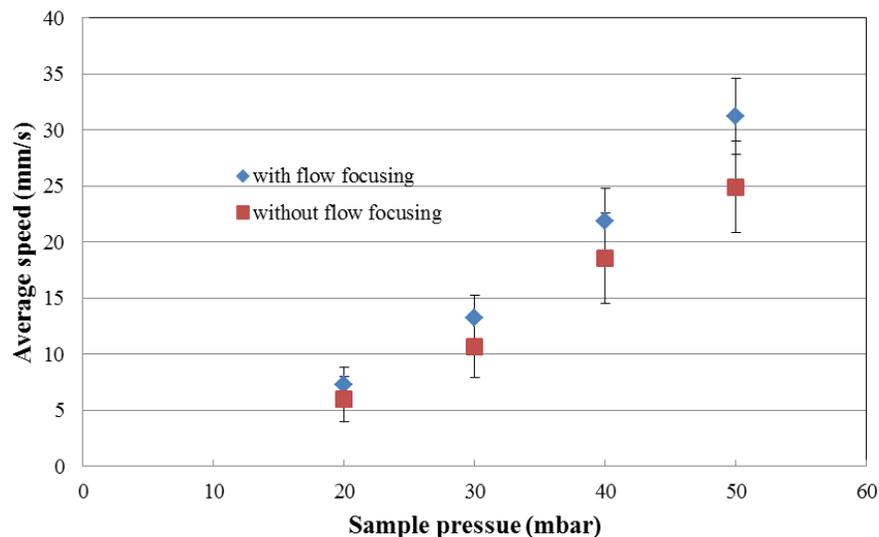
Figure 7.12: Comparison of the average flow velocity for flows with and without

hydrodynamic focusing

139

7.5. Proof of concepts: particle count and numerical studies

7.5.1. Experimental

In this experiment, we counted the number of fluorescent micro-particles flowed through the main microchannel of the chip with and without hydrodynamic focusing for varying pressure settings. The experimental set-up is very similar to that of particle tracking experiment, except the absence of the second detection point and hence there is no need for the second laser source in this experiment. In brief, an aqueous solution of 10 μm fluorescent microspheres is inserted into the sample inlet of the chip. For each pressure setting, two runs of the experiment are conducted; one with DI water sheath flow and another with blocked sheath inlet. In each run, the particles were interrogated by light from a 532-nm diode laser fed through the center waveguide of the chip and emitted fluorescent signals were picked up by an optical fibre placed right under the detection area of the chip and fed into a PMT equipped with a 542-nm long pass optical filter. Flow control of the MFCS and particle counting were carried out with a LabVIEW script on a PC. Each of the runs was conducted for five minutes for comparison of particle counts. The results are summarized in Table 7.3. The results show that the particle count reduces as we activate the sheath fluid inlet for each of the sample pressure settings. Qualitatively this is easy to understand that as sheath fluid occupies part of the microchannel volume, the sample inlet channel dispenses lesser amount of

fluid to the main microchannel due to higher effective flow resistance of the downstream channel. Figure 7.13 shows the plots of particle count with and without sheath flow against pressure at the sample inlet for quick reference.

Table 7.3: Summary of results obtained from the particle detection experiment

Sample pressure (mbar)	Sheath Pressure (mbar)	Particle count
20	23	12
	no sheath	21
30	36	15
	no sheath	30
40	50	18
	no sheath	40
50	65	20
	no sheath	52
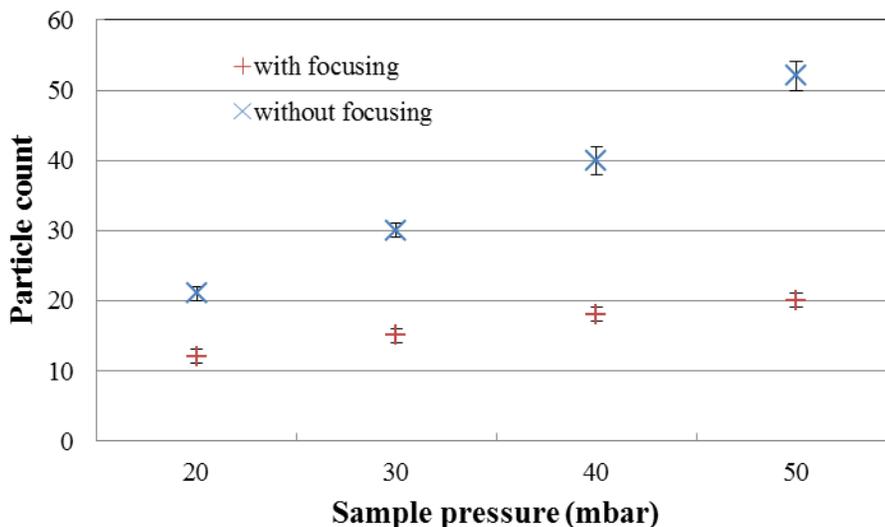
Figure 7.13: Experimental particle count as a function of pressure applied at the

sample inlet

7.5.2. Numerical understanding of the particle count experiments

To gain a better understanding of the results, we have again utilized the Q3D model and we have also developed a simple analytical model, 1D circuit equivalency model. The derivation of the 1D circuit equivalency flow equation for our chip is shown in Appendix A.

With the Q3D model, we solve for the particle dispense rate of the sample inlet to the main microchannel with appropriate boundary conditions to reflect the conditions of flow with and without sheath fluid. Because the no-sheath flow was experimentally realized by simply blocking the sheath inlet with an adhesive tape on top of the sheath inlet, we apply a no-slip boundary condition at the sheath

inlet boundary of the Q3D model. Among the three outlets of the chip only the central one was placed at a boundary condition of *0 Pa* (atm. pressure) and the other two are in no-slip boundary condition as they were kept blocked during the experiment. In calculating the particle dispense rate we have assumed that the particle dispense rate is proportional to the flow rate of sample fluid through the sample inlet microchannel (i.e., uniform particle concentration).

The experimental and numerical results of the ratio of particle count (particle count with sheath flow/particle count without sheath flow) as a function
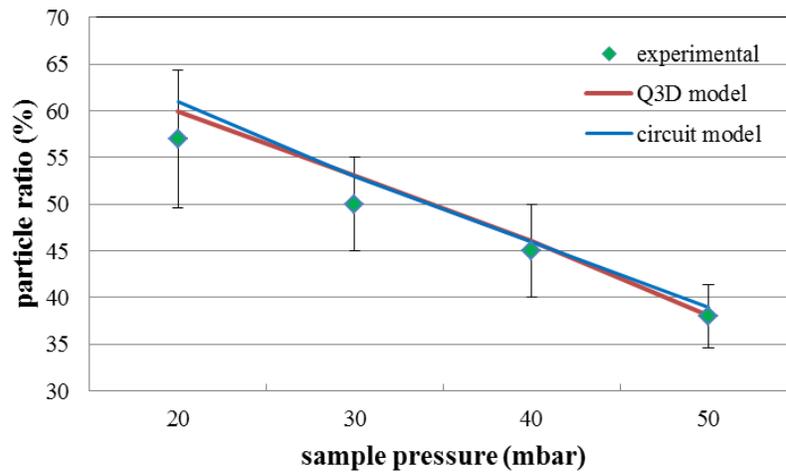
Figure 7.14: Comparison of experimental and numerical results of particle ratio (particle with sheath flow/particle without sheath flow)

of pressure at the sample inlet are shown in Figure 7.14. As we can see from the plots, even the simplified circuit model provides results with astonishingly close

match to the numerical results of the Q3D model. Experimental results are in good agreement with the results of both of the models. The maximum deviation occurs at 20 mbar with the experimental value 6% lower than the Q3D numerical predictions. Higher error at low pressure is due to very lower number of particle counts during the experiments.

7.6. Demonstration of sorting functionality

The ultimate goal of developing this microfluidic cytometer is to sort a particular type of cells/particles from a mixture of different types of cells/particles, i.e., to utilize this as a cell sorter. As a preliminary study of the sorting functionality of our biochip, we demonstrated the switching capability of our side-flow switching system using a homogeneous fluorescent microparticle solution and determined two sorting parameters, the sorting efficiency and maximum possible throughput. We did not measure another commonly referred sorting parameter, the sorting purity, as that required some more instruments that we lacked in our lab. As our goal was to sort rare events from a mixer (e.g., VSEL SC from cord blood), enrichment was more important to us than purity.

7.6.1. Determining flow switching time

As we have already mentioned in earlier chapters that the targeted particle is sorted by diverting the main microchannel flow from a default destination by activating a side-flow channel after the targeted particle is detected upstream. The

activation and setting up of the side-flow stream take some finite time that limits the throughput of sorting. So finding this time lag (combination of response time of MFCS and settling time of side-flow stream) is very important. The details of the experimental procedure to find this time parameter are stated below.

Both the sample and sheath flows of the chip are already established with DI water and controlled by two pressure channels of the MFCS. Also a third pressure channel is connected to a colored DI water reservoir of the side-flow switching inlet and it is adjusted to such a pressure value that a no-flow condition is established through the side-flow channel. After these conditions are stabilized, a single trigger pulse is used to switch the side-flow pressure to a higher value so that the main flow (combined sample and sheath flows) is completely diverted from the default outlet channel to the other outlet channel. This can be identified by the complete occupation of the default output channel by the colored water. The same trigger pulse is also used to switch on a LED on top of the chip, near the diversion region. . The video images of the flow at a region near the junction of the two outlet channels and the pressure channel are recorded. The total time lag, from the instant of applying the pressure switching pulse to the instant when the side-flow stream settles down to its final width, is determined from the recorded video. It is to be mentioned here that the instance a glow from the LED is observed in the video is taken as the starting point of the trigger pulse. The switching delay of the LED is small compared to the response time of the MFCS pressure channel and the settling time of the fluid flow. It was observed that

combined response time of the MFCS and settling time of the side-flow of our system is ~100 ms. Thus, our sorter system is limited to a maximum throughput of about 600 cells per minute.

7.6.2. Dynamic sorting of homogeneous microparticles

Automatic particle detection and counting, microscope imaging and real-time monitoring of fluorescent microspheres were used to experimentally characterize the dynamic sorting functionality of our chip. Initially, dynamic sorting of microspheres from its homogeneous aqueous solution was performed to evaluate its sorting efficiency. The experiments were conducted with hydrodynamic focusing included. Light from a 532-nm CW diode laser was focused into an optical fiber that coupled the light to the central built-in waveguide of the chip that delivered the light to the detection region of the chip to interrogate the microspheres. The laser induced fluorescence emissions from the microspheres were collected by a PMT placed right under the detection region. Upon the detection of a particle, the switching was performed and controlled automatically using a data acquisition card and a special architecture of the LabVIEW software, the 'producer-consumer' architecture. In this architecture, in a multi-thread system, a loop continues to monitor the output of the detection PMT while another loop executes the activation algorithm of the side-flow pressure channel simultaneously. A second PMT was placed under either the waste channel or the sorted particle channel to monitor whether the detected particle was actually

sorted or not. Also for the lower speed particles (up to 30mbar pressure), video image for a region near the junction of the three channels was recorded to

(1)	(2)	(3)

(4)	(5)	(6)
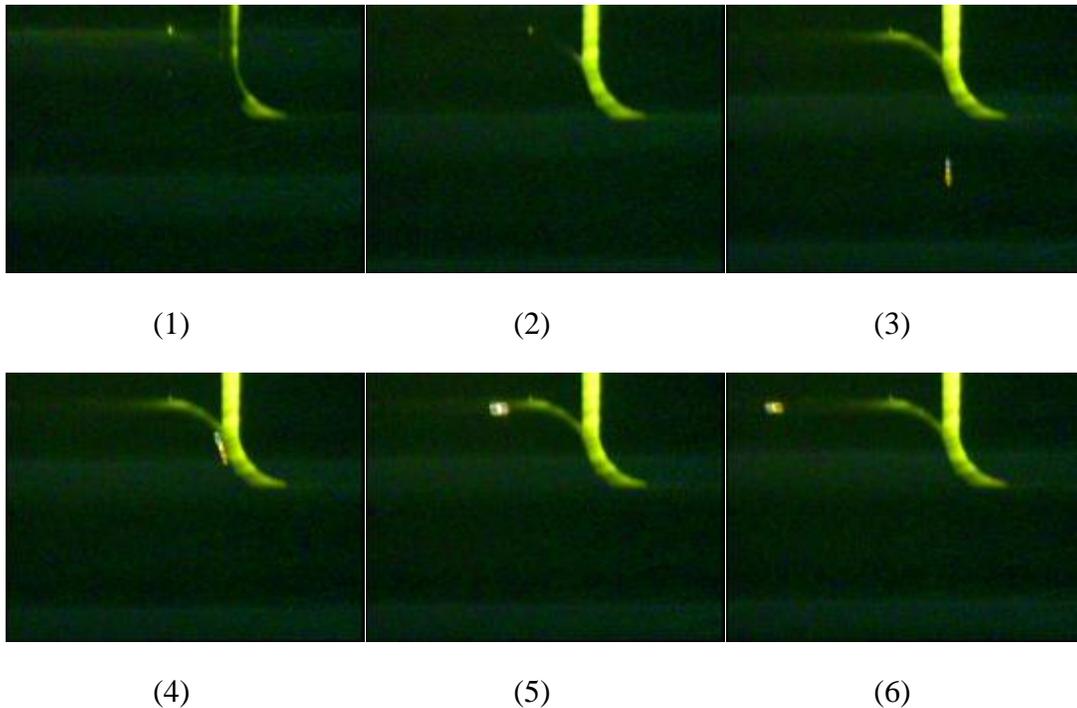
Figure 7.15: Six sequential images to show the event of the sorting of a particle. Main microchannel is from bottom to top of each picture and side-flow microchannel is from right to left of each picture (carrying yellow colored fluid in pictures). Image (1) shows the initial default flow state. Image (2) shows the side-flow was activated initializing the switching upon the detection of a particle upstream. Images (3), (4), (5) and (6) show the different positions of the particle during the switching event.

determine whether the detected particle was sorted or not. The flow was kept switched for some pre-determined duration and after that the default flow was

again re-established. The flow switching duration was varied with sample pressure settings. The duration was chosen such that even the lowest speed microsphere should have reached the sorted particle channel before the default flow was re-established. Figure 7.15 shows 6 sequential still images taken from the recorded video of one of the experiments to depict a particle being sorted.

Table 7.4: Summary of the results of the sorting experiments

Sample pressure (mbar)	Sheath Pressure (mbar)	Duration of flow switching (s)	Sorting efficiency (%)
20	23	3	97 ± 3
30	36	2	97 ± 3
40	50	2	93 ± 3
50	65	1	87 ± 3

The experiments were conducted for different pressure settings for the sample and sheath inlets. The results are analyzed for the same number of total detected particles of 20 and their summary is shown in Table 7.4. The sorting efficiency was close to 100% for the first two cases but as the pressure increases the sorting efficiency drops. We observed that at the higher pressure settings some

of the high-speed particles were not diverted to the sorted particle outlet even though their speed was well below the higher threshold set by the flow switching time. Because the distance between the detection point and the diversion point is 1 cm and flow switching time is ~100ms, the maximum speed a particle can have and still should be sorted is 10 cm/s. From previous results, the maximum speed of particle at our highest pressure setting (sample: 50 mbar, sheath: 65 mbar) is 3.56 cm/s (experimental value) or 3.64 cm/s (Q3D model value), well below the threshold. So, normally all the high-speed particles should have been sorted. However, surprisingly we observed that the flow switching was sometimes further delayed (visibly more than 100ms, between 500*ms* and 1*s*) during the dynamic sorting operation. This could be due to running the flow control LabVIEW script on a general desktop PC operating system environment that could not dedicate itself to execute the LabVIEW script alone, but to operate simultaneously other system software too. This could sometimes cause the switching time to be longer than what was expected that made the high-speed particle to sweep past the diversion region before the flow switching was established. A dedicated flow controller, i.e. a micro-controller based real-time flow controller, can be used to solve this problem.

To investigate the ability of the system to sort one type of particles from a mixture of two types of particles, we mixed two particle in equal proportion, fluorescent (10 μm) and non-fluorescent (4 μm), fed into the sample inlet and performed the sorting algorithm to sort out the fluorescent particles from the

149

mixture. In the experiment 30 and 40 mbar of pressure were applied to the sample and sheath inlets, respectively, and, video images for a region near the junction of the three channels was recorded. We observed that all the detected fluorescent particles were diverted to the sorted particle outlet. We also observed that some non-fluorescent particles went straight to the waste particle outlet because they were not detected by the PMT. In this experiment the sample concentration was low enough to ensure not more than a single particle was in one sorting volume. Further study needs to be done for quantitative results on sorting purity as a function of concentration, switching duration etc. As our goal is to sort a very rare population of cells (e.g. VSEL SCs from cord blood samples), sorting efficiency is very important as it ensures significant recovery of rare cells. Several sorting steps can be repeated for the enriched rare cells to finally obtain the desired purity of the rare cells).

7.7. Detection of non-fluorescent beads

As mentioned earlier, one of our initial motivations was to sort label-free cells. As a preliminary study toward achieving that goal, we tested our 2nd generation chip for its capability to detect unlabelled micro-particles. Initially, detection of non-fluorescent microspheres from its homogeneous aqueous solution was tested to see if the detection system could even see the beads without any labels. In this experiment, hydrodynamically focused non-fluorescent latex microspheres (9.6 μm in diameters) were flowed through the microchannel. Light from a 532-nm CW diode laser was focused into an optical fiber that coupled the light to the

central built-in waveguide of the chip that delivered the light to the detection region of the chip to interrogate the microspheres. The intensity of the side-scattered light off the microspheres was picked up by an optical fibre (core diameter 1 mm) placed right under the detection region and measured by a PMT. The experiments were conducted for different pressure settings for the sample and sheath inlets and we found that our system could detect the non-fluorescent beads based on the side-scattered light intensity. On the average, we got a PMT detection signal of about 2 V. However, to get a reasonably good detection signal, we had to increase the PMT gain by 100 compared to what was used for fluorescent microsphere detection (PMT gain was set at 10^5 for fluorescent bead detection and at 10^7 for non-fluorescent bead detection). This implies that the SNR for the detection of the untagged beads was reduced by a factor of 100 compared to that of fluorescent bead detection. From Table 6.1 of Chapter 6, we see that the average SNR for under-chip detection of fluorescent beads was 374. Thus, the predicted SNR for the untagged bead detection is about 3.7 which would result in the probabilities of about 11% false positive and missing positive (Assuming Gaussian distributions both for the signal and the noise levels). As we described in Chapter 6, the SNR could approximately be doubled if the waveguide detection system was implemented in this experiment instead of under-chip detection. In that case, the false/missing positive probabilities would be reduced to about 4%.

7.8. Labelled cells: feasibility of detection

To test the feasibility of detection of labelled biological cells, the fluorescence emission of labelled biological cells was measured and compared to that of the fluorescent beads under same illumination and detection conditions. The biological cells used for this test were the THP-1 cell line (human acute monocytic leukemia cell line). They are an established cell line of monocyte (a type of white blood cell) origin. The cells were labelled with fluorescent CellTracker™ Orange CMTMR probes (Invitrogen™, Molecular Probes®, absorption peak: 541 nm, emission peak: 565 nm). A fluorescence microscope view of the cells is shown in Figure 7.16. The cells were in the range of 8 to 25 μm in diameters.
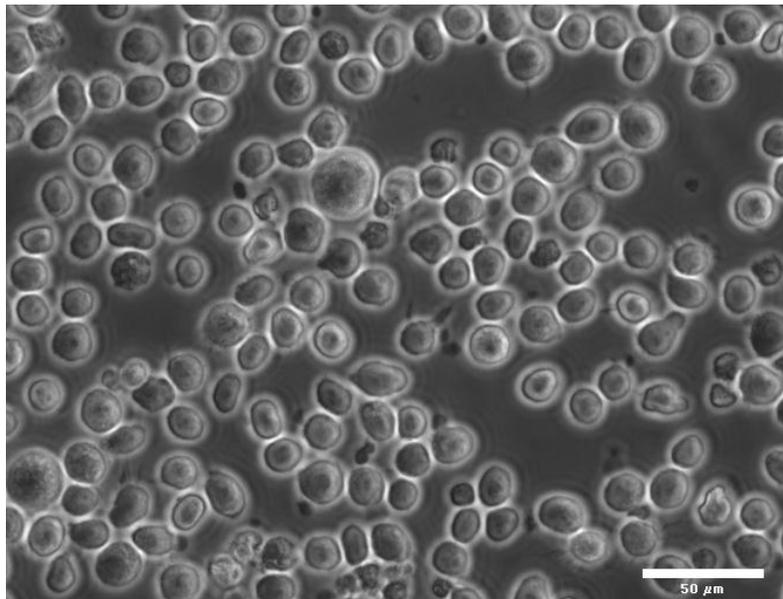
Figure 7.16: A fluorescence microscope view of the THP-1 cells
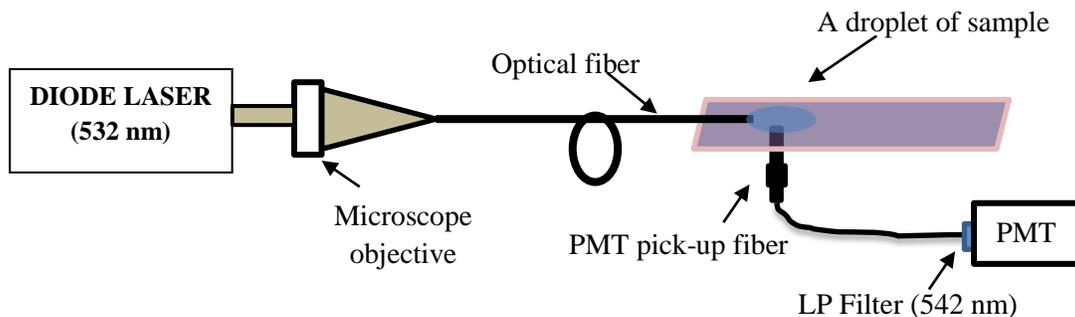
Figure 7.17: The experimental setup to measure fluorescence signal from the biological cell

The experimental setup to measure the emitted fluorescence is shown in Figure 7.17. In this experiment, first a drop of sample solution containing biological cells was placed on a microscope glass slide. Light from a 532-nm CW laser was focused into an optical fiber. The tip of the other end of the optical fiber was inserted into the drop of the sample solution and adjusted to shine a single cell inside the drop. A pick-up optical fibre (core diameter 1 mm) was placed under the microscope glass slide and adjusted right below the cell position touching the slide from underneath. The collected scattered green light (532 nm) was suppressed by an optical filter and the fluorescence signal was measured by a PMT. We have obtained an average PMT output of 2.3 V for a gain setting of 10^6. We repeated the test for the detection of a single fluorescent bead (10 μm in diameter) and obtained an average PMT output of 2.1 V for the same illumination and detection settings. We adjusted the fiber and detector alignment to maximize

the signal in each case. The signal values indicate that the detection of fluorescently labelled cells with our 2nd generation of microchip would result in the very similar average SNR value as that of fluorescent latex beads reported in Chapter 6.

7.9. Design consideration for improved sorter throughput

One of the important performance characteristics of a cell sorter system is the sorting throughput. Hydrodynamic response time, side-flow ON time and the response time of the external pump system are the main factors that limit the throughput of a cell sorter employing pressure-driven hydrodynamic side-flow switching. However, the hydrodynamic response time of water is very fast (response is instantaneous for ideal incompressible fluid), and as mentioned earlier, the maximum achievable throughput of the current sorter is limited by the response time of the external pump (MFCS) which is ~100 ms. Considering the fact that a much faster pressure actuator can potentially be built, the very fast hydrodynamic response time of the hydrodynamic side-flow switch can be exploited to achieve potentially much higher sorting throughput of a cell sorter system employing this sorting mechanism. Some of the chip design elements that affect the sorting speed are: length of the side-flow channel, and, distance between detection and sorting regions. A schematic diagram showing these design elements and conceptual sorting for a practical system is shown in Figure 7.18.
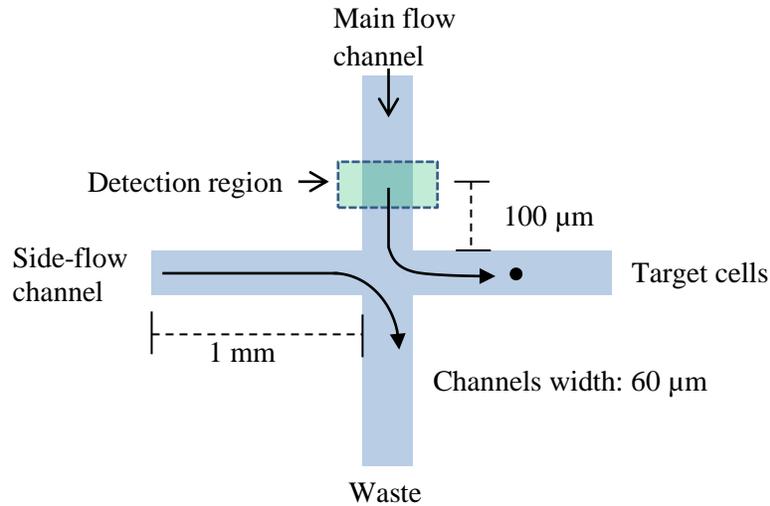
Figure 7.18: The schematic diagram showing the key design elements to estimate

the sorting speed of a practical sorter

The time-dependent Q3D model could potentially be used to find the
hydrodynamic flow switching time for a given chip design. But the current model
is based on Navier-Stokes formulation of flow equations for incompressible fluid
and so the response time it provides is instantaneous (speed of pressure flow is
infinity). So, a time-dependent compressible fluid flow model is needed to find
the hydrodynamic flow switching time for a given chip design. However,
generally it can be assumed that a pressure disturbance at a point in a fluidic
system travels at the speed of sound in that fluid. So the time required per mm
length of a flow switching channel of water is ~0.7 μs (sound of speed in pure
water is 1500 m/s). The distance between the detection region and the sorting
junction mainly depends on the combined response time of the pressure actuation
and the hydrodynamic side-flow switching (neglecting the very small time

requirement for the processing of optical and electronic data). For a practical system, let us assume that this combined response time is 1 ms. If the working maximum speed of flow is 10 cm/s, the distance between the detection region and the sorting junction could be kept at 100 μm. To ensure that all the cells between the maximum speed and half of the maximum speed (this would cover almost 100% cells, as can be seen from the Figure 7.6) are sorted out, the side-flow channel should be kept ON for ~ 2 ms. So, the average time required to sort a single cell is ~4 ms, providing a throughput of 250 cells/s. For the same chip design, the throughput can further be improved by designing a smart sorter system that would adjust its switching ON time depending on the speed of the cells. Also the throughput can further be improved by increasing the working speed of flow. Parallelization of multiple sorters can provide even much higher sorting throughput.

7.10. Estimation of throughput and sorting purity for the potential VSEL SC sorting application

The concentration of blood cells is about 4 to 6 million per microliter of the human peripheral blood sample, among which about 90% are the red blood cells (RBCs) and about 10% are the white blood cells (WBCs) and platelets [144]. Besides these cells, the human peripheral blood also contains a very small number of VSEL SCs, about 150-300 per ml in number [145]. We like to predict the approximate throughput and purity (or concentration enrichment) of the sorted

156

VSEL SCs in a single run of a human peripheral blood sample through the sorter design described in the section 7.9. Before the blood sample is fed to the sorter inlet, the RBCs are removed from it by lysis. At this stage, the remaining cell concentration would be about 500 million per ml, among which about 150-300 would be the VSEL SC. If the working maximum flow speed of the sample is 10 cm/s, the average sample flow rate would be about 0.17 microliter/s. This implies that we would require about 16 hours to sort 10 ml of the lysed blood sample, which would result in approximately 2,000 VSEL SC targets. As described in the previous section, the detection of a VSEL stem cell will initiate the opening of the side-flow channel and it is kept open for 2 ms for each sorting event. This corresponds to a sorting volume of 0.00034 microliter of lysed peripheral blood sample or about 170 blood cells including the single target VSEL SC. It means that 170 blood cells including the target VSEL SC will be diverted to the sorting bin each time a detection signal is identified. Thus, the concentration enrichment of the VSEL SCs for a single run would be about 15,000. The resulting sorted volume can be diluted and run through the sorter again to get the desired purity of the VSEL SCs. Note this is based on a single biomarker for VSEL SCs or a label free technique to discriminate VSEL SCs can be found. For the moment the isolation of VSEL SCs require up to 12 biomarkers [22] [146].

Chapter 8

Summary and Future Work Recommendations

8.1. Introduction

In this chapter, we summarize the work done in this thesis, i.e. the summary of contributions of this thesis, and put forward the recommendations for possible future directions of the research.

8.2. Summary of contributions

The foci of this thesis were two-fold: The development of a computationally efficient numerical Q3D model for laminar flows in planar microfluidic devices; Development, experimental characterization and numerical validation of the performance of an opto-microfluidic chip for flow cytometric applications. The miniaturization of bio-analytical devices utilizing microfluidics has gained

momentum in recent decades to take advantage of the benefits accompanying microfabrication and micro-scale analysis. However, currently there is no rigorous simulation-based verification of devices prior to fabrication; therefore, development of a microfluidic device is generally based on a fabrication-design-fabrication cycle resulting in a long and expensive product development phase. The main premise in these investigations is that the inherent advantages associated with efficient numerical modeling and microfabrication technologies can be exploited to predict the behaviour and increase the capabilities of this type of instrumentation. For general 3D fluid flow systems, different numerical techniques have been used for many years, and, a number of commercial software packages are currently available. However, these packages are designed to handle general and arbitrary boundary conditions and therefore require extensive computing resources and time for solving chip-scale problems. Again, many different integrated microfluidic flow cytometers design have been proposed in the literature and demonstrated their functionalities. However, very little design and functional evaluations have been reported, and, also there is room to improve the integration of optical functionality into the chip.

We have described the development of a novel technique for simulation of laminar flows in microfluidic devices fabricated using planar microfabrication topology, such as etching or embossing processes, which is the technology used for most of the present day microfluidic devices (Chapter 3). The development steps described in Chapter 3 are:

- Derivation of the Q3D model: 3D Navier-Stokes flow equations with 3D viscosity effects are reduced to a set of limited number of coupled 2D PDEs by a Fourier series decomposition of the velocity profile of an incompressible fluid in the direction normal to the planar layers of a microfluidic device.

- Verification: The model is then solved by a commercial PDE solver (General PDE Solver, COMSOL) for some test cases. The test results are compared with analytical solutions and numerical values obtained from a commercial 3D hydrodynamic solver. Accuracy comparable to the 3D commercial package is achieved while realizing significant decrease in computation time thus allowing detailed 3D modeling of microfluidic devices on desktop computers. The Q3D model is also validated with experimental results (Chapter 7). Some of the flow functionalities of a microfabricated cell sorter are characterized experimentally and it is found that they are in good agreement with the numerical predictions of the Q3D model.

- Extending the model to time-dependent boundary conditions: Steady-state Q3D model is extended to include the time-varying terms in it and the modified model is solved for a scaled-down version of a typical problem of a flow switching system that has potential application in hydrodynamic cell sorter system.

160

Two prototype versions of a first generation of a flow cytometer system were developed and tested for the proof-of-concept experiments (Chapter 4). Cheap materials and easier techniques were used to make those prototypes.

- Prototype I: Flow channels were inscribed in a transparency sheet, which was then bonded in between two microscope glass slides by using UV epoxy. Optical fibers were inserted from the sides of chip and were bonded by UV epoxy.

- Prototype II: Flow channels were inscribed in a new polymer material, Surlyn™ by using a steel template of the channel structures and then the bonding of the chip layers was achieved through a simple and inexpensive fusion bonding set-up without the use of a commercial bonder. Optical fibers were inserted from the sides of chip and were bonded by UV epoxy.

- Proof-of-concept tests: Detection and sorting functionalities of both of the miniaturized cytometer prototypes were tested by using fluorescent microspheres. The results of the detection and sorting experiments were analyzed and explained in light of the flow geometries and flow profiles of the two prototypes.

Design, fabrication and performance evaluation of the second generation of our flow cytometer chip fabricated using the state-of-the-art microfabrication

161

tools are presented (Chapter 5, Chapter 6 and Chapter 7). We fabricated an all-PMDS opto-microfluidic flow cytometer chip with monolithically integrated hydrodynamic focusing system, solid-core optical waveguides and hydrodynamic side-flow switching system in it (Chapter 5).

We have evaluated the optical characteristics of the developed cytometer chip (chapter 6). We have estimated the propagation losses of the waveguide for green (532 nm) and red light (633 nm) to be 1.6 and 1.5 dB/cm, respectively. We have also estimated the SNR of our detection system for two different detection set-ups: under-chip signal pick-up and waveguide signal pick-up. We found an average SNR of 765 for waveguide signal pick-up, whereas for the conventional way of under-chip pick-up, it was 374.

In addition to the characterization of the detection system, we have also evaluated/characterized the other four important aspects of the cell sorter: General flow, flow focusing and detection and sorting functionalities (Chapter 7). Volumetric flow metering and fluorescent particle visualization and particle tracking were used to investigate the general flow behaviour of the microfluidic chip. Volumetric flow metering gave much lower (~20% off) flow speed values than the numerical predictions given by the Q3D model. The average flow speed values obtained from the fluorescent particle visualization and tracking experiment match well with the Q3D calculations up to the sample inlet pressure value of 30 mbar. At higher pressure values, the experimental values are found to

be larger than the numerical predictions, presumably due to the lateral migration of particles away from the microchannel walls due to wall effect. However, the maximum flow speed values are found to agree well (within the experimental uncertainties) with the numerical predictions for the whole range of pressure values. The widths of the focused stream as a function of the strength of focusing (ratio of the sheath pressure to the sample pressure) are determined experimentally by FWHM method and they are found to be consistent with the Q3D calculated values within the experimental error limit. For example, the FWHM width of the focused stream at the sample and sheath pressure values of 50 and 65 mbar, respectively (strength of focusing is 1.3), is 26.7 ± 2.2 µm and the corresponding Q3D calculation is 25.7 µm. Velocity distributions of particles with and without hydrodynamic focusing were studied experimentally and it is found that average speed of particle increases and standard deviation decreases with the hydrodynamic focusing.

Detection of fluorescent particles experiments were carried out with and without hydrodynamic focusing and their ratio were compared to both the Q3D calculations and the circuit equivalency model calculations. The experimental results are found to agree well with the results of both the numerical models. The switching time of the hydrodynamic side-flow switching (the combined response time of the MFCS and the settling time of the side flow) system of our sorter was determined experimentally to be ~100 ms. So the maximum throughput achievable with this sorter system is limited to 600 cells per minute. The

investigation of the dynamic sorting of microparticles was performed by real-time monitoring of fluorescent particles through different channels and sorting efficiency of more than 90% was achieved for most of the experiments.

We achieved a lower sorting throughput with our sorter than that reported by most of the other groups mentioned in the literature review (Section 2.5). However, our sorter system achieves a higher sorting efficiency which is very crucial for significant recovery of very rare target cells (e.g. VSEL SCs from cord blood samples and circulating tumor cells from blood samples). The present system can be used to sort tagged stem cells from cord blood samples, to sort or detect tagged circulating tumor cells from blood samples or pathogens in water samples. The detection system of the device needs to be further refined and characterized before it can be used to detect and sort label-free stem cells.

8.3. Suggestions for future work

The major recommendations for continuation of research on our work are mentioned here.

8.3.1. Q3D model

- There are some important applications of microfluidics that make use of inertial effects of fluid flow to achieve their functionalities, e.g. mixer, inertial flow focuser. The current Q3D model neglects the inertial term of

the Navier-Stokes equation to simplify the derivation process to account for low Reynold's number flows only. However, the Fourier series decomposition is general and applicable in cases where inertial effects are important. So, it would be possible to derive a modified Q3D planar microfluidics model (system of 2D non-linear coupled PDEs) that could include inertial effect in it, thereby making the model much more general.

- Particle dynamics in micro-flow can be investigated. It could be incorporated into the Q3D model so that it would be capable of predicting particle distribution in the flow cross-section.

- Response time of the flow switching system is very important for dynamic sorting as it determines the maximum throughput of the system. The dynamics of the mechanical pump system can be studied and the Q3D model can be further studied for its possible modification to include the dynamics of the pump. It would allow us to predict the response time of a flow system to a pressure change.

8.3.2. Cell sorter system

- The cell sorter should be studied with real cells. This should be done to test the operating capabilities of the cell sorter and to make any change to the design or material or methods, if necessary.

- The cell sorter could be characterized for the detection of scattered light off the cells. It would allow us to study label-free cell sorting capability of the PDMS biochips.

- Current MFCS has very large response time ($\sim 100 ms$) that limits the maximum throughput of the cell sorter. Construction of a second generation pump system using Gas Jet valve is underway. The response time of the valve is on the order of few ms. Its cost is an order of magnitude lower than the current MFCS. Thus it is a much cheaper and faster alternative to the MFCS. This pump can be studied with the cell sorter system to characterize its flow functionalities. Also some of the experiments (e.g. the volumetric flow analysis of 7.3.2) mentioned in this thesis can be repeated for further verification.

- A better method of coupling light from optical fiber to the built-in waveguide and vice versa should be devised. Also the coupling losses should be characterized experimentally.

- Split-waveguide interrogation can be implemented in the detection region to simultaneously detect the particle and determine its speed. Interrogation and detection can also be implemented in the default waste channel and the sorted particle channel for automatic determination of sorting efficiency, sorting purity etc.

- The feasibility of incorporating a light source and detectors in chip design can be studied. This is very important for true miniaturization of the system.

166

8.4. Summary statements

The thesis has developed a novel quasi-3D model for efficient simulation of flows in planar microfluidic devices with low Reynolds numbers. The solution of the model provides comparable accuracy to the full 3D numerical solution by a commercial package with significant decrease in computation time, thus allowing microfluidic simulation and design optimization on a desktop computer similar to microelectronic device simulation. Also an opto-microfluidic flow cytometer system was developed, experimentally characterized for flows and fluorescent detection and sorting, and, the results were interpreted by numerical simulation. The results have paved the way to the development of low-cost micro-cytometer systems for the detection/sorting of fluorescently labelled very rare cells and should increase the potential for label-free cell sorting in the near future.

Bibliography

[1] H. H. Hou, Y. N. Wang, C. L. Chang, R. J. Yang and L. M. Fu, "Rapid glucose concentration detection utilizing disposable integrated microfluidic chip," *Microfluid. Nanofluid.,* vol. 11, pp. 479-487, 2011.

[2] X. Weng, C. H. Chon, H. Jiang and D. Li, "Rapid detection of formaldehyde concentration in food on a polydimethylsiloxane (PDMS) microfluidic chip," *Food Chemistry,* vol. 114, pp. 1079-1082, 2009.

[3] X. Weng, H. Jiang and D. Li, "Microfluidic DNA hybridization assays," *Microfluid. Nanofluid.,* vol. 11, pp. 367-383, 2012.

[4] H. Jiang, X. Weng and D. Li, "Microfluidic whole-blood immunoassays," *Microfluid. Nanofluid.,* vol. 10, pp. 941-964, 2011.

[5] H. W. Wu, R. C. Hsu, C. C. Lin, S. M. Hwang and G. B. Lee, "An integrated microfluidic system for isolation, counting, and sorting of hematopoietic stem cells," *Biomicrofluidics,* vol. 4, p. 024112, 2010.

[6] S. Senapati, A. R. Mahon, J. Gordon, C. Nowak, S. Sengupta, T. H. Q. Powell, J. Feder, D. M. Lodge and H. Chang, "Rapid on-chip genetic detection microfluidic platform for real world applications," *Biomicrofluidics,* vol. 3, p. 022407, 2009.

[7] J. C. Jokerst, J. M. Emory and C. S. Henry, "Advances in microfluidics for environmental analysis," *Analyst,* vol. 137, pp. 24-34, 2012.

[8] M. Wang and Q. Kang, "Electrochemomechanical energy conversion efficiency in silica nanochannels," *Microfluid. Nanofluid.,* vol. 9, pp. 181-190, 2010.

[9]   X. Su, S. E. Kirkwood, M. Gupta, L. Marquez-Curtis, Y. Qiu, A. Janowska-Wieczorek, W. Rozmus and Y. Y. Tsui, "Microscope-based label-free microfluidic cytometry," *Opt. Express,* vol. 19, pp. 387-398, 2011.

[10] S. Sharma, A. Moniz, I. Triantis, K. Michelakis, J. Trzebinski, A. Azarbadegan, B. Field, C. Toumazou, I. Eames and A. Cass, "An integrated silicon sensor with microfluidic chip for monitoring potassium and pH," *Microfluid. Nanofluid.,* vol. 10, pp. 1119-1125, 2011.

[11] C. H. Lin, J. H. Wang and L. M. Fu, "Improving the separation efficiency of DNA biosamples in capillary electrophoresis microchips using high-voltage pulsed DC electric fields," *Microfluid. Nanofluid,* vol. 5, pp. 403-410, 2008.

[12] E. Kjeang, N. Djilali and D. Sinton, "Microfluidic fuel cells: a review," *Power Sources,* vol. 186, pp. 353-369, 2009.

[13] J. Mairhofer, K. Roppert and P. Ertl, "Microfluidic systems for pathogen sensing: A review," *Sensors,* vol. 9, pp. 4804-4823, 2009.

[14] Y. Zhang and P. Ozdemir, "Microfluidic DNA amplification - a review," *Anal. Chim. Acta,* vol. 638, pp. 115-125, 2009.

[15] H. M. Shapiro, Practical Flow Cytometry, 3rd ed., New York: Willy-Liss, 1995.

[16] D. Erickson, "Towards numerical prototyping of labs-on-chip: Modeling for integrated microfluidic devices," *Microfluid. Nanofluid.,* vol. 1, pp. 301-318, 2005.

[17] M. Koch, A. G. R. Evans and A. Brunnschweiler, "Coupled FEM simulation for the characterization of the fluid flow within a micromachined cantilever valve," *Micromech. Microeng.,* vol. 6, pp. 112-114., 1996.

[18] M. Mimeault and S. K. Batra, "Concise review: Recent advances on the significance of stem cells in tissue regeneration and cancer therapies," *Stem Cells,* vol. 24, pp. 2319-2345, 2006.

[19] J. A. Cancelas and D. A. Williams, "Stem cell mobilization by β2-agonists," *Nature Medicine,* vol. 12, pp. 278-279, 2006.

[20] M. Z. Ratajczak, E. K. Zuba-Surma, M. Wysocznynski, J. Ratajczak and M. Kucia, "Very small embryonic-like stem cells: Characterization, developmental origin, and biological significance," *Experimental Hematology,* vol. 36, pp. 742-751, 2008.

[21] E. K. Zuba-Surma, M. Kucia, J. Ratajczak and M. Z. Ratajczak, "Small stem cells in adult tissues: Very small embryonic-like stem cells stand up!," *Cytometry,* vol. 75, no. 1, pp. 4-13, 2008.

[22] R. Danova-Alt, A. Heider, D. Egger, M. Cross and R. Alt, "Very Small Embryonic-Like Stem Cells Purified from Umbilical Cord Blood Lack Stem Cell Characteristics," *PLoS ONE,* vol. 7, no. 4, pp. e34899 (1-11), 2012.

[23] E. K. Zuba-Surma, I. Klich, N. Greco, M. J. Laughlin, J. Ratajczak and M. Z. Ratajczak, "Optimization of isolation and further characterization of umbilical cord blood-derived very small embryonic/ epiblast-like stem cells (VSELs)," *European Journal of Hematology,* vol. 84, no. 1, pp. 34-46, 2010.

[24] H. Ali and F. Al-Mulla, "Defining umbilical cord blood stem cells," *Stem Cell Discovery,* vol. 2, no. 1, pp. 15-23, 2012.

[25] L. Bużańska, E. K. Machaj, B. Zablocka, Z. Pojda and K. Domańska-Janik, "Human cord blood-derived cells attain neuronal and glial features in vitro," *J Cell Sci,* vol. 115, pp. 2131-2138, 2002.

[26] X. T. Su, C. Capjack, W. Rozmus and C. Backhouse, "2D light scattering patterns of mitochondria in single cells," *Opt Exp,* vol. 15, no. 17, pp. 10562-10575, 2007.

[27] X. T. Su, S. E. Kirkwood, M. Gupta, L. M. Curtis, Y. Qiu, A. J. Wieczorek, R. Rozmus and Y. Y. Tsui, "Microscope-based label-free microfluidic cytometry," *Opt Exp,* vol. 19, no. 1, pp. 387-398, 2011.

[28] X. T. Su, W. Rozmus and Y. Y. Tsui, "A fiber-coupled microfluidic cytometer for the obtaining of nanostructural mitochondria information in single cells," *Proc. of SPIE,* vol. 7573, pp. 75730K(1-8), 2010.

[29] X. T. Su, Y. Qiu, L. M. Curtis, M. Gupta, C. E. Capjack, W. Rozmus, A. J. Wieczorek and Y. Y. Tsui, "Label-free and noninvasive optical detection of the distribution of nanometer-size mitochondria in single cells," *J of Biomed. Opt.,* vol. 16, no. 6, pp. 067003(1-7), 2011.

[30] M. Z. Islam, X. T. Su, S. E. Kirkwood, K. Singh, J. N. McMullin, W. Rozmus, A. J. Wieczorek and Y. Y. Tsui, "Development of an opto-microfluidic flow cytometer for the sorting of stem cells from blood samples," *Proc. of SPIE,* vol. 7386, pp. 73860C(1-8), 2009.

[31] K. H. Han, A. Han and A. B. Frazier, "Microsystems for isolation and electrophysiological analysis of breast cancer cells from blood," *Biosensors and Bioelectronics,* vol. 21, pp. 1907-1914, 2006.

[32] P. Kiesel, J. Martini, M. Huck, M. Recht, M. Bern and N. Johnson, "Opto-fluidic detection platform for pathogen detection in water," in *CLEO*, Baltimore, MD, 2011.

[33] J. P. Brody, P. Yager, R. E. Goldstein and R. H. Austin, "Biotechnology at low Reynolds numbers," *Biophys.,* vol. 71, no. 12, pp. 3430-3441, 1996.

[34] H. Bruss, Theoretical Microfluidics, New York: Oxford University Press, 2008.

[35] D. Li, Electrokinetics in Microfluidics, San Diego: Elsevier Academic, 2004.

[36] P. Tabeling, Introduction to Microfluidics, New York: Oxford University Press, 2005.

[37] D. Sobek, A. M. Young, M. L. Gray and S. D. Senturia, "A microfabricated flow chamber for optical measurements in fluids," in *Micro Electro Mechanical Systems, 1993, MEMS '93, Proceedings of Investigation of Micro Structures, Sensors, Actuators, Machines and Systems. IEEE*, 1993.

[38] V. Gass, B. H. van der Schoot and N. F. de Rooij, "Nanofluid handling by micro-flow-sensor based on drag force measurements," in *Micro Electro Mechanical Systems, 1993, MEMS '93, Proceedings of Investigation of Micro Structures, Sensors, Actuators, Machines and Systems, IEEE*, 1993.

[39] A. Manz, Y. Miyahara, J. Miura, Y. Watanabe, H. Miyagi and K. Sato, "Design of an open-tubular column liquid chromatograph using silicon chip technology," *Sensors Actuators B: Chem.,* vol. 1, pp. 249-255, 1990.

[40] J. Tirén, L. Tenerz and B. Hök, "A batch-fabricated non-reverse valve with cantilever beam manufactured by micromachining of silicon," *Sensors and Actuators,* vol. 18, no. 7, pp. 389-396, 1989.

[41] T. Bourouina and J. P. Grandchamp, "Modeling micropumps with electrical equivalent networks," *Micromech. Microeng.,* vol. 6, pp. 398-404, 1996.

[42] F. J. Auerbach, G. Meiendres, R. Müller and G. J. E. Scheller, "Simulation of the thermal behaviour of thermal flow sensors by equivalent electrical circuits," *Sensors and Actuators A: Physical,* vol. 41, pp. 275-278, 1994.

[43] N. R. Swart and A. Nathan, "Flow-rate microsensor modelling and optimization using SPICE," *Sensors and Actuators A: Physical,* vol. 34, no. 8, pp. 109-122, 1992.

[44] J. Ulrich and R. Zengerle, "Static and dynamic flow simulation of a KOH-etched microvalve using the finite-element method," *Sensors and Actuators A: Physical,* vol. 53, no. 5, pp. 379-385, 1996.

[45] Y. Wang, Q. Lin and T. Mukherjee, "System-oriented dispersion models of general-shaped electrophoresis microchannels," *Lab on a Chip,* vol. 4, pp. 453-463, 2004.

[46] Y. Wang, Q. Q. Lin and T. Mukherjee, "A model for laminar diffusion-based complex electrokinetic passive micromixers," *Lab on a chip,* vol. 5, pp. 877-887, 2005.

[47] J. Zeng and T. Korsmeyer, "Principles of droplet electrohydrodynamics for lab-on-achip," *Lab on a Chip,* vol. 4, pp. 265-277, 2004.

[48] M. Horner, "Computational analysis of on-line coupled ITP-CE," in *Technical Proceedings of the 2005 NSTI Nanotechnology Conference and Trade Show (NanoTech 2005),* Anaheim, CA, 2005.

[49] T. Q. Truong and N. T. Nguyen, "Simulation and optimization of tesla valves," in *Technical Proceedings of the 2003 Nanotechnology Conference and Trade Show (NanoTech 2003),* San Francisco, CA, 2003.

[50] S. Krishnamoorthy and M. G. Giridharan, "Analysis of sample injection and band-broadening in capillary electrophoresis microchips," in *Technical Proceedings of the 2000 International Conference on Modeling and Simulation of Microsystems*, San Diego, CA, 2000.

[51] M. Turowski, Z. J. Chen and A. Przekwas, "Automated generation of compact models for fluidic microsystems," *Analog Integrated Circuits and Signal Processing,* vol. 29, pp. 27-36, 2001.

[52] J. Q. Lu, P. Yang and X. H. Hu, "Simulations of light scattering from a biconcave red blood cell using the finite-difference time-domain method," *Biomed. Opt.,* vol. 10, pp. 024022(1)-024022(2-10), 2005.

[53] V. Ost, J. Neukammer and H. Rinneberg, "Flow cytometric differentiation of erythrocytes and leukocytes in dilute whole blood by light scattering," *Cytometry,* vol. 32, pp. 191-197, 1998.

[54] M. J. Madou, Fundamentals of Microfabrication: The Science of Miniaturization, Boca Raton, Fl: CRC, 2002.

[55] H. C. Sung, J. M. Godin, C. Chen, W. Qiao, H. Lee and Y. Lo, "Review Article: Recent advancements in optofluidic flow cytometer," *Biomicrofluidics,* vol. 4, p. 043001 (23 pp.), 2010.

[56] S. Kim, S. Jeon, G. Yi, C. Heo, J. H. Choi and S. Yang, "Optofluidic assembly of colloidal photonic crystals with controlled sizes, shapes, and structures," *Adv Mater,* vol. 20, pp. 1649-1655, 2008.

[57] S. Azmayesh-Fard, E. Flaim and J. N. McMullin, "PDMS biochips with integrated waveguides," *Micromech. Microeng.,* vol. 20, p. 087002 (5 pp), 2010.

[58] H. Hosseinkhannazer, L. Kostiuk and J. N. McMullin, "Multilayer biochips with integrated optics replicated in PMMA and PDMS," *Proceedings of the SPIE,* vol. 6796, p. 67960B, 2007.

[59] C. L. Bliss, J. N. McMullin and C. J. Backhouse, "Integrated wavelength-selective optical waveguides for microfluidic-based laser-induced fluorescence detection," *Lab Chip,* vol. 8, p. 143–151, 2008.

[60] K. B. Mogensen, J. El-Ali, A. Wolff and J. P. Kutter, "Integration of polymer waveguides for optical detection in microfabricated chemical analysis systems," *Appl. Opt.,* vol. 42, p. 4072–4079, 2003.

[61] M. Fleger, D. Siepe and A. Neyer, "Microfabricated polymer analysis chip for optical detection," *IEEE Proc. Nanobiotechnol.,* vol. 151, p. 159–61, 2004.

[62] S. H. Huang and F. G. Tseng, "Development of a monolithic total internal reflection-based biochip utilizing a microprism array for fluorescence sensing," *Micromech. Microeng.,* vol. 15, p. 2235–2242 , 2005.

[63] S. Balslev, A. M. Jorgensen, B. Bilenberg, K. B. Mogensen, D. Snakenborg, K. J. P. Geschke O and A. Kristensen, "Lab-on-a-chip with integrated optical transducers," *Lab Chip,* vol. 6, p. 213–217, 2006.

[64] C. L. Bliss, C. J. Backhouse and J. N. McMullin, "Two-colour microparticle detection in PDMS biochips with integrated optics," *Proc. SPIE,* vol. 6796, p. 67960A, 2007.

[65] C. L. Bliss, J. N. McMullin and C. J. Backhouse, "Rapid fabrication of a microfluidic device with integrated optical waveguides for DNA fragment analysis," *Lab Chip,* vol. 7, p. 1280–1287, 2007.

[66] H. Hosseinkhannazer, L. W. Kostiuk and J. N. McMullin, "Two-species microparticle etection in optofluidic biochips with polymeric waveguides," *Proc. SPIE,* vol. 7099, p. 70990H1–H6, 2008.

[67] C. M. Klapperich, "Microfluidic diagnostics: time for industry standards," *Rev. Med. Devices,* vol. 6, p. 211–3, 2009.

[68] J. K. Taylor, "The Design and Evaluation of a Microfluidic Cell Sorting Chip," University of Waterloo, Waterloo, ON, 2007.

[69] T. Vilkner, D. Janasek and A. Manz, "Micro Total Analysis Systems. Recent Developments," *Analytical Chemistry,* vol. 76, pp. 3373-3386, 2004.

[70] D. Erickson and D. Li, "Integrated Microfluidic Devices," *Analytica Chimica Acta,* vol. 507, pp. 11-26, 2004.

[71] P. C. H. Li, Microfluidic Lab-on-a-Chip for Chemical and Biological Analysis and Discovery, Boca Raton, FL: Taylor & Francis Group, 2006.

[72] H. Andersson and A. van den Berg, "Microfluidic devices for cellomics: a review," *Sens. and Act. B,* vol. 92, pp. 315-325, 2003.

[73] Z. Wang, J. El-Ali, M. Engelund, T. Gotsaed, I. R. Perch-Nielsen, K. B. Mogensen, D. Snakenborg, J. P. Kutter and A. Wolff, "Measurement of scattered light on a microchip flow cytometer with integrated polymer based optical elements," *Lab Chip,* vol. 4, pp. 372-377, 2004.

[74] R. Yang, D. L. Feeback and W. Wang, "Microfabrication and test of a three-dimensional polymer hydro-focusing unit for flow cytometry applications," *Sens. and Act. A,* vol. 118, pp. 259-267, 2005.

[75] R. Miyake, H. Ohki, I. Yamazaki and T. Takagi, "Investigation of sheath flow chambers for flow cytometers: micromachined flow chamber with low pressure loss," *JSME Int. J. B.,* vol. 40, pp. 106-113, 1997.

[76] G. B. Lee, C. H. Lin and G. L. Chang, "Micro flow cytometers with buried SU-8/SOG optical waveguides," *Sens. and Act. A,* vol. 103, pp. 165-170, 2003.

[77] J. Goddin, V. Lien and Y. H. Lo, "Demonstration of two-dimensional fluidic lens for integration into microfluidic flow cytometers," *Appl. Phys. Lett.,* vol. 89, pp. 061106(1)-061106(2-3), 2006.

[78] J. Goddin and Y. H. Lo, "Microfluidic flow cytometer with on-chip lens systems for improved signal resolution," *Proc. IEEE Sensors,* pp. 466-469.

[79] S. C. Jacobson and J. M. Ramsey, "Electrokinetic focusing in microfabricated channel structures," *Anal. Chem.,* vol. 69, pp. 3212-3217, 1997.

[80] D. P. Schrum, C. T. Culbertson, S. C. Jacobson and J. M. Ramsey, "Microchip flow cytometry using electrokinetic focusing," *Anal. Chem.,* vol. 71, pp. 4173-4177, 1999.

[81] G. Medoro, N. Manaresi, L. Leonardi, L. Altomare, M. Tartagni and R. Guerrieri, "A lab-on-a-chip for cell detection and manipulation," *IEEE Sens.,* vol. 3, pp. 317-325, 2003.

[82] A. Y. Fu, H. Chou, C. Spence, F. H. Arnold and S. R. Quake, "An Integrated Microfabricated Cell Sorter," *Anal. Chem.,* vol. 74, pp. 2451-2457, 2002.

[83] M. Rieseberg, C. Kasper, K. F. Reardon and T. Scheper, "Flow Cytometry in Biotechnology," *Appl. Micro. and Biotech.,* vol. 56, pp. 350-360, 2001.

[84] B. S. Cho, T. G. Schuster, X. Zhu, D. Chang, G. D. Smith and S. Takayama, "Passively Driven Integrated Microfluidic System for Separation of Motile Sperm," *Analytical Chemistry,* vol. 75, pp. 1671-1675, 2003.

[85] M. R. Melamed, T. Lindmo and M. L. Mendelsohn, Flow Cytometry and Sorting, New York, NY: John Wiley & Sons, 1990.

[86] W. Zhang, B. Zhang, Y. L. Zhang, D. Han and Y. L. Zhou, "Trapping yeast cells on pdms micropillar array," *Advanced materials research,* Vols. 476-478, pp. 2096-2099, 2012.

[87] B. E. Layton, B. Lynch, T. Peter and B. Jamieson, "Red blood cell sorting with a multi-bed microfabricated filter," *Micromech. Microeng.,* vol. 22, p. 025009, 2012.

[88] R. Carlson, C. Gabel, S. Chan and R. Austin, "Self-sorting of white blood cells in a lattice," *Phys. Rev. Lett.,* vol. 79, p. 2149–2152, 1997.

[89] O. Bakajin, R. Carlons, C. Chou, S. Chan, C. Gabel, J. Knight, T. Cox and R. Austin, "Sizing, Fractionation and Mixing of Biological Objects via Microfabricated Devices," *microTAS,* p. 193–198, 1998.

[90] P. Wilding, L. J. Kricka, J. Cheng, G. Hvichia, M. A. Shoffner and P. Fortina, "Integrated cell isolation and polymerase chain reaction analysis using silicon microfilter chambers," *Anal. Biochem.,* vol. 257, p. 95–100, 1998.

[91] H. Andersson, W. van der Wijngaart, P. Enoksson and G. Stemme, "Micromachined flow-through filter-chamber for chemical reactions on beads," *Sens. Actuators,* vol. 67, p. 203–208, 2000.

[92] J. Harrison, P. Li, T. Tang and W. Lee, "Manipulation of Biological Cells and DNA on Chip," *microTAS,* p. 82–84, 1996.

[93] A. Manz, C. Effenhauser, N. Bruggraf, J. Harrison, K. Seiler and K. Fluri, "Electroosmotic pumping and electrophoretic separations for miniaturized chemical analysis systems," *Micromech. Microeng.,* vol. 4, p. 257–265, 1994.

[94] M. Ramsey, S. Jacobson and M. Knapp, "Microfabricated chemical measurement systems," *Nat. Med.,* vol. 1, p. 1093–1095, 1995.

[95] A. Fu, C. Spence, A. Scherer, F. Arnold and S. Quake, "A microfabricated fluorescence-activated cell sorter," *Nat. Biotechnol.,* vol. 17, p. 1109– 1111, 1999.

[96] P. Li and J. Harrison, "Transport, manipulation, and reaction of biological cells on-chip using electrokinetic effects," *Anal. Chem.,* vol. 69, p. 1564– 1568, 1997.

[97] S. Fiedler, S. Shirley, T. Schnelle and G. Fuhr, "Dielectrophoretic sorting of particles and cells in a microsystem," *Anal. Chem,* vol. 70, p. 1909–1915, 1998.

[98] G. Markx, Y. Huang, X. Zhou and R. Pethig, "Dielectrophoretic characterization and separation of microorganisms," *Microbiology,* vol. 140, p. 585–591, 1994.

[99] J. Cheng, E. Sheldon, L. Wu, A. Uribe, L. Gerrue, J. Carrino, M. Heller and J. O'Connell, "Preparation and hybridization analysis of DNA/RNA from E. coli on microfabricated bioelectronic chips," *Nat. Biotechnol,* vol. 70, p. 2321–2326, 1998.

[100] F. Becker, X. Wang, Y. Huang, R. Pethig, J. Vykoukal and P. Gascoyne, "Separation of human breast cancer cells from blood by differential dielectric affinity," *Proc. Natl. Acad. Sci.,* vol. 92, p. 860–864, 1995.

[101] X. Wang, J. Yang, Y. Huang, J. Vykoukal, F. Becker and P. Gascoyne, "Cell separation by dielectrophoretic field-flow-fractionation," *Anal. Chem.,* vol. 72, p. 832–839, 2000.

[102] Y. Huang, S. Joo, M. Duhon, M. Heller, B. Wallace and X. Xu, "Dielectrophoretic cell separation and gene expression profiling on microelectronic chip arrays," *Anal. Chem.,* vol. 74, p. 3362–3371, 2002.

[103] J. Voldman, M. Gray, M. Toner and M. Schmidt, "A microfabrication-based dynamic array cytometer," *Anal. Chem.,* vol. 74, p. 3984–3990, 2002.

[104] Y. Huang, K. Ewalt, M. Tirado, R. Haigis, A. Forster, D. Ackley, M. Heller, J. O'Connell and M. Krihak, "Electric manipulation of bioparticles and macromolecules on microfabricated electrodes," *Anal. Chem.,* vol. 73, p. 1549–1559, 2001.

[105] S. Miltenyi, W. Müller, W. Weichel and A. Radbruch, "High gradient magnetic cell separation with MACS," *Cytometry Part A,* vol. 11, no. 2, pp. 231-238, 1990.

[106] N. Pamme and A. Manz, "On-chip free-flow magnetophoresis: continuous flow separation of magnetic particles and agglomerates," *anal. chem.,* vol. 76, no. 24, pp. 7250-6, 2004.

[107] A. Ashkin, J. M. Dziedzic and T. Yamane, "Optical Trapping and Manipulation of Single Cells using Infrared Laser Beams," *Nature,* vol. 330, pp. 769-771, 1987.

[108] M. W. Wang, E. Tu, D. E. Raymond, J. M. Yang, H. Zhang, N. Hagen, B. Dees, E. M. Mercer, A. H. Forster, I. Kariv, P. J. Marchand and W. F. Butler, "Microfluidic Sorting of Mammalian Cells by Optical Force Switching," *Nat. Biotec.,* vol. 23, pp. 83-8, 2005.

[109] L. Johansson, F. Nikolajeff, S. Johansson and S. Thorslund, "On-chip fluorescence-activated cell sorting by an integrated miniaturized ultrasonic transducer," *Anal. Chem.,* vol. 81, p. 5188–5196, 2009.

[110] O. Jakobsson, C. Grenvall and T. Laurell, "Acoustic actuated fluorescence activated cell sorting," in *CYTO 2012*, Leipzig, Germany, 2012.

[111] M. E. Piyasena, P. P. A. Suthanthiraraj, R. W. Applegate, A. M. Goumas, T. A. Woods, G. P. López and S. W. Graves, "Multinode acoustic focusing for parallel flow cytometry," *Anal. Chem.,* vol. 84, p. 1831−1839, 2012.

[112] S. Y. Yang, S. K. Hsuing, Y. C. Hung, C. M. Chang, T. L. Liao and G. B. Lee, "A Cell Counting/Sorting System Incorporated with a Microfabricated Flow Cytometer Chip," *Meas. Sc. and Technol.,* vol. 17, pp. 2001-2009, 2006.

[113] J. N. McMullin, "Propagating Beam Method Simulation of Planar Multimode Optical Waveguides," in *Proc. of SPIE*, Boston, 1991.

[114] A. J. Smits, Fluid Mechanics, New York, NY: John Wiley & Sons, Inc., 2000.

[115] L. Bocquet and J. L. Barrat, "Hydrodynamic boundary conditions and correlation functions of confined fluids," *Phys. Rev. Lett.,* vol. 70, no. 18, pp. 2726-2729, 1993.

[116] H. Amini, E. Sollier, W. M. Weaver and D. D. Carlo, "Intrinsic particle-induced lateral transport in microchannels," *PNAS,* vol. 109, no. 29, p. 11593–11598, 2012.

[117] K. K. Gupta and J. L. Meek, "A brief history of the beginning of the finite element method," *Numer. Meth. Engng.,* vol. 39, pp. 3761-3774, 1996.

[118] G. Pelosi, "The finite-element method, Part I: R. L. Courant [Historical Corner]," *IEEE Ant. and Prop.,* vol. 49, pp. 180-182, 2007.

[119] F. Chorlton, Textbook of Fluid Dynamics, London: D. Van Nostrand Company Limited, 1967.

[120] Y. Wang, "Modeling and simulation of lab-on-a-chip systems," PhD Thesis, Carnegie Melon University, USA, 2005.

[121] D. A. Ateya, J. S. Erickson, P. B. Howell, L. R. Hilliard, J. P. Golden and F. S. Ligler, "The good, the bad, and the tiny: A review of microflow cytometry," *Anal. Bioanal. Chem.,* vol. 391, p. 1485–1498, 2008.

[122] T. F. Hong, W. J. Ju, M. C. Wu, C. H. Tai, C. H. Tsai and L. M. Fu, "Rapid prototyping of PMMA microfluidic chips utilizing a CO2 laser," *Microfluid. Nanofluid.,* vol. 9, p. 1125–1133, 2010.

[123] H. Klank, J. P. Kutter and O. Geschke, "CO2-laser micromachining and back-end processing for rapid production of PMMA-based microfluidic systems," *Lab Chip,* vol. 2, p. 242–246, 2002.

[124] M. Bowden, O. Geschke, J. P. Kutter and D. Diamond, "CO2 laser microfabrication of an integrated polymer microfluidic manifold for the determination of phosphorus," *Lab Chip,* vol. 3, p. 221–223, 2003.

[125] M. F. Jensen, J. E. McCormack, B. Helbo, L. H. Christensen, T. R. Christensen and O. Geschke, "Rapid prototyping of polymer microsystems via excimer laser ablation on polymeric moulds," *Lab Chip,* vol. 4, p. 391–395, 2004.

[126] F. Bundgaard, G. Perozziello and O. Geschke, "Rapid prototyping tools and methods for all- Topasw cyclic olefin copolymer fluidic Microsystems," *Proc. Inst. Mech. Eng. C.-J. Mech. E.,* vol. 220, p. 1625–1632, 2006.

[127] N. Kim, M. C. Murphy, S. A. Soper and D. E. Nikitopoulos, "Liquid-liquid segmented flows in polymer microfluidic channels," in *Proc. ICNMM*, Pohang, South Korea, 2009.

[128] P. K. Yuen and V. N. Goral, "Low-cost rapid prototyping of flexible microfluidic devices using a desktop digital craft cutter," *Lab Chip,* vol. 10, p. 384–387, 2010.

[129] G. M. Whitesides, "The origins and the future of microfluidics," *Nature,* vol. 442, no. 7101, pp. 368-373, 2006.

[130] K. B. Mogensen, H. Klank and J. P. Kutter, "Recent developments in detection for microfluidic systems," *Electrophoresis,* vol. 25, p. 3498–3512, 2004.

[131] E. Verpoorte, "Beads and chips: new recipes for analysis," *Lab chip,* vol. 3, p. 60N–68N, 2003.

[132] V. Lien, K. Zhao, Y. Berdichevsky and Y. H. Lo, "High-sensitivity cytometric detection using fluidic-photonic integrated circuits with array waveguides," *IEEE Sel. Top. Quan. Electron.,* vol. 11, no. 4, pp. 827-834, 2005.

[133] O. Leistiko and P. F. Jensen, "Integrated bio/chemical microsystems employing optical detection: The clip-on," *Micromech. Microeng.,* vol. 8, p. 148–150, 1998.

[134] L. Cui, T. Zhang and H. Morgan, "Optical particle detection integrated in a dielectrophoretic lab-on-a-chip," *Micromech. Microeng.,* vol. 12, p. 7–12, 2002.

[135] O. J. A. Schueller, X. M. Zhao, G. M. Whitesides, S. P. Smith and M. Prentiss, "Fabrication of liquid-core waveguides by soft lithography," *Adv. Mat.,* vol. 11, p. 37–41, 1999.

[136] V. Lien, Y. Berdichevski and Y. H. Lo, "A prealigned process of integrating optical waveguides with microfluidic devices," *IEEE Phot. Tech. Lett.,* vol. 16, no. 6, pp. 1525-1527, 2004.

[137] M. J. Walker, "Comparison of Bosch and cryogenic processes for patterning high aspect ratio features in silicon," *Proc. of SPIE,* vol. 4407, pp. 89-99, 2001.

[138] R. Dussart, M. Boufnichel, G. Marcos, P. Lefaucheux, A. Basillais, R. Benoit, T. Tillocher, X. Mellhaoui, H. Estrade-Szwarckopf and P. Ranson, "Passivation mechanisms in cryogenic SF6/O2 etching process," *Micromech. Microeng.,* vol. 14, no. 2, p. 190, 2004.

[139] T. Defforge, X. Song, G. Gautier, T. Tillocher, R. Dussart, S. Kouass and F. Tran-Van, "Scalloping removal on DRIE via using low concentrated alkaline solutions at low temperature," *Sensors and Actuators A: Physical,* vol. 170, pp. 114-120, 2011.

[140] Micralyne, "Microfluidic tool kit operating manual v3.30.00," Edmonton, AB, 2002.

[141] Y. W. Kim and J. Y. Yoo, "Transport ofsolid particles in microfluidic channels," *Optics and Lasers in Engineering,* vol. 50, p. 87–98, 2012.

[142] J. S. Park, S. H. Song and J. H. I, "Continuous focusing of microparticles using inertial lift force and vorticity via multi-orifice microfluidic channels," *Lab on a Chip,* vol. 9, p. 939–948, 2009.

[143] H. Amini, E. Sollier, W. M. Weaver and D. D. Carlo, "Intrinsic particle-induced lateral transport in microchannels," *PNAS,* pp. 1207550109(1-6), 2012.

[144] W. F. Ganong, Review of Medical Physiology, New York: Lange Medical Books/McGraw-Hill, 2003.

[145] E. K. Surma and M. Z. Ratajczak, Current Protocols in Cytometry, Chapter 9, Unit 9.29.

[146] M. Z. Ratajczak, R. Liu, W. Marlicz, W. Blogowski, T. Starzynska, W. Wojakowski and E. Zuba-Surma, *Method in Cell Biology,* vol. 103, pp. 31-54, 2011.

Appendix A

Circuit Equivalency Model of Microfluidics

The simplified circuit equivalency model of microfluidics was applied to find the particle count ratio (ratio of particle count with hydrodynamic focusing to the particle count without hydrodynamic focusing) in the section 7.5.2. The schematic structure and the equivalent circuit of the chip used in that experiment is shown in Figure A.1 and A.2, respectively.
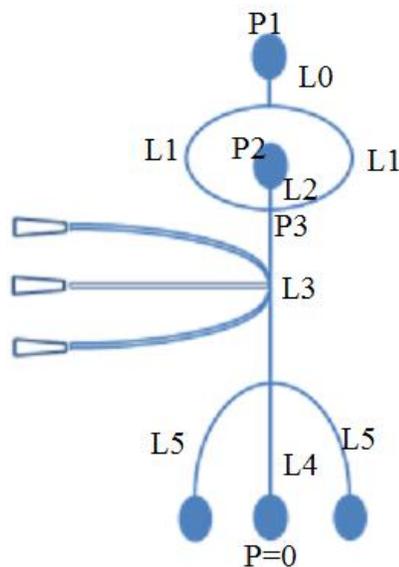
Figure A.1: Schematic layout with lengths of the different sections of the chip
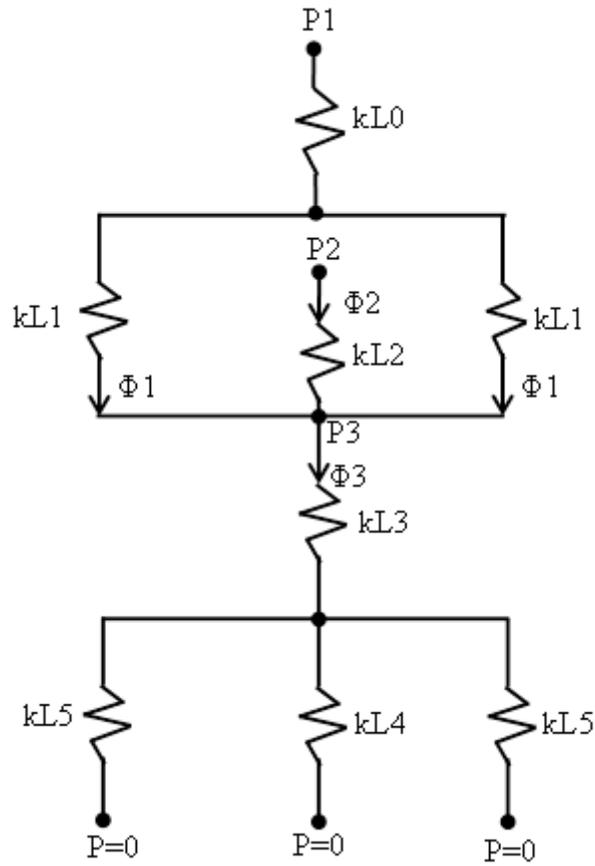
Figure A.2: Equivalent circuit model of the chip layout shown in Figure A.1

The resistances of the channel sections in the equivalent circuit are proportional to the length of each section, as the channel cross-sections are same for the whole chip. The flow rate, Φ, (similar to current in an electrical circuit, I) in each branch can be found by applying the following law similar to the Ohm's law at that branch:

$$\Phi = \frac{P}{R_h} \tag{A.1}$$

Here, R_h is the equivalent hydraulic resistance of the channel to the flow, Φ is the flow rate and P is the pressure drop in that channel branch.

Applying KCL at the flow focusing junction gives,

$$\Phi_3 = \Phi_1 + \Phi_2 \tag{A.2}$$

Substituting Equation (A.1) into Equation (A.2) gives,

$$\frac{P3}{k.L3'} = \frac{P1-P3}{k.L1'} + \frac{P2-P3}{k.L2} \tag{A.3}$$

Where,

$$L1' = L0 + \frac{L1}{2} \tag{A.4}$$

and

$$L3' = L3 + L4 \parallel \frac{L5}{2} = L3 + \frac{L4.L5}{2L4+L5} \tag{A.5}$$

From the Equation (A.3):

$$P3 = \frac{\left(\dfrac{P1}{L1'} + \dfrac{P2}{L2}\right)}{\left(\dfrac{1}{L1'} + \dfrac{1}{L2} + \dfrac{1}{L3'}\right)} \tag{A.6}$$

The flow rate in the sample channel with the hydrodynamic focusing, $\Phi_2(foc)$, can be found by,

$$\Phi2(foc) = \frac{P2-P3}{k.L2} = \frac{1}{k.L2}\left(P2 - \frac{\left(\dfrac{P1}{L1'} + \dfrac{P2}{L2}\right)}{\left(\dfrac{1}{L1'} + \dfrac{1}{L2} + \dfrac{1}{L3'}\right)}\right) \tag{A.7}$$

And, the flow rate in the sample channel without hydrodynamic focusing, $\Phi_2(no\text{-}foc)$, is:

$$\Phi 2(no - foc) = \frac{1}{k.L2}\left(P2 - \frac{\dfrac{P2}{L2}}{\left(+\dfrac{1}{L2} + \dfrac{1}{L3'} \right)} \right) \tag{A.8}$$

The ratio of the flow rates, which is also the ratio of particle dispensing rate (considering same particle concentration in both cases), can be found by dividing the Equation (A.7) by the Equation (A.8)

$$Particle - ratio = \frac{\Phi_2(foc)}{\Phi_2(no - foc)} = \frac{P2 - \dfrac{\dfrac{P1}{L1'} + \dfrac{P2}{L2}}{\dfrac{1}{L1'} + \dfrac{1}{L2} + \dfrac{1}{L3'}}}{P2 - \dfrac{\dfrac{P2}{L2}}{\dfrac{1}{L2} + \dfrac{1}{L3'}}} \tag{A.9}$$

Equation (A.9) can be used to calculate the *particle-ratio* for the known pressure values of the sample and sheath inlet. The equivalent length values can be calculated according to the experimental conditions at the inlets and outlets.

Appendix B

Numerical solution of the Q3D model using COMSOL general PDE mode

The PDE Application Mode (General form) of the COMSOL multiphysics

software developed by COMSOL, Inc, was used for solving the 2D coupled PDEs

of the Q3D model. We also used the COMSOL Fluid Dynamics (Incompressible

Navier-Stokes) Application Mode for full-3D simulation of some flow problems.

The step-by-step implementation procedures of the Q3D model in the COMSOL

PDE Application Mode (General Form) are stated below.

Model Navigator:
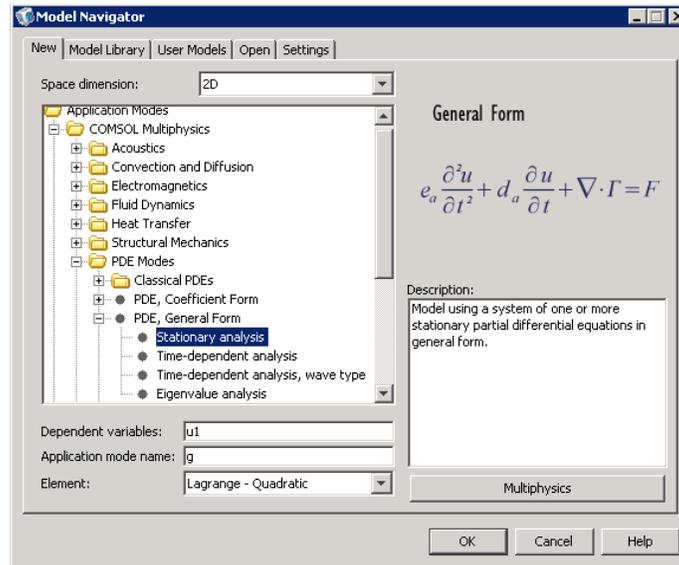
Figure B.1: COMSOL Model Navigator window

1) Go to *Model Navigator* of the COMSOL Multiphysics and select 2D from the *space dimension* list.

2) From the list of *Application Modes*, select *COMSOL Multiphysics>PDE Modes>PDE, General Form* folder. Then select *Stationary analysis*.

3) Write the names of the dependent variable in the *Dependent variables* field and click OK. This will bring the window shown in Figure B.2 and provide the option to insert only one PDE into the system.
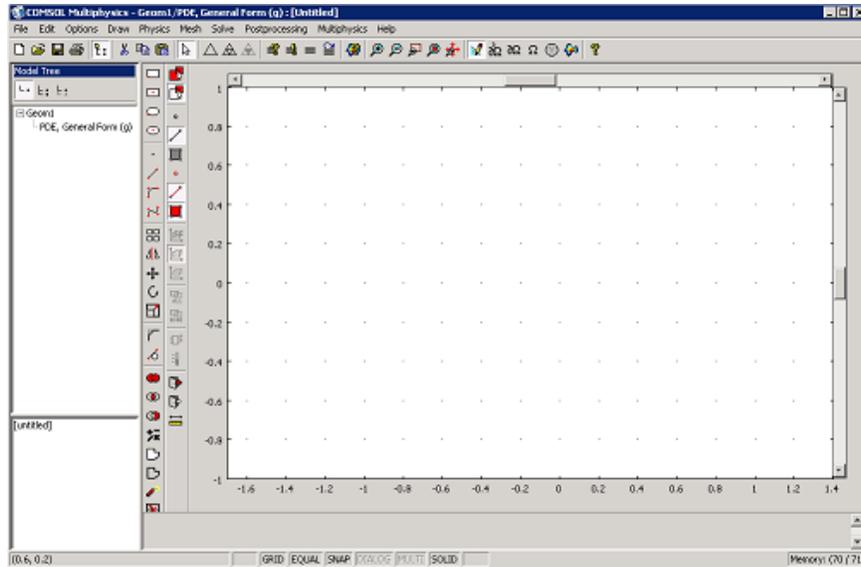
Figure B.2: COMSOL workplace window

4) Go to *Multiphysics* menu and choose *Model Navigator* to keep on adding more dependent variables. For example, for the Q3D model with 4 Fourier terms, we need to add 9 variables (hence 9 PDEs).

Options and Settings:

1) To parameterize the model, go to the *options* menu and choose *constants*

2) Insert the following entries in the *Constants* dialog box to represent fluid and geometry parameters.
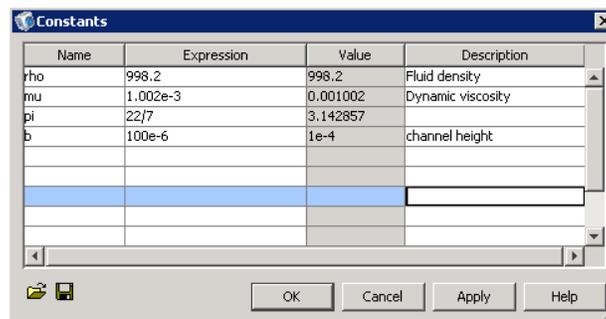
Figure B.3: Constants dialog box to enter parameter values used in the PDEs

189

Geometry modeling:

Draw the computational geometry (e.g. the mid-slice of a T-cell) by using the built-in CAD drawing tools of COMSOL. It is also possible to import different types of CAD drawings to the COMSOL environment. For details of geometry modeling in COMSOL, please refer to the COMSOL Multiphysics User's Guide. After the drawing, the geometry looks like the following.
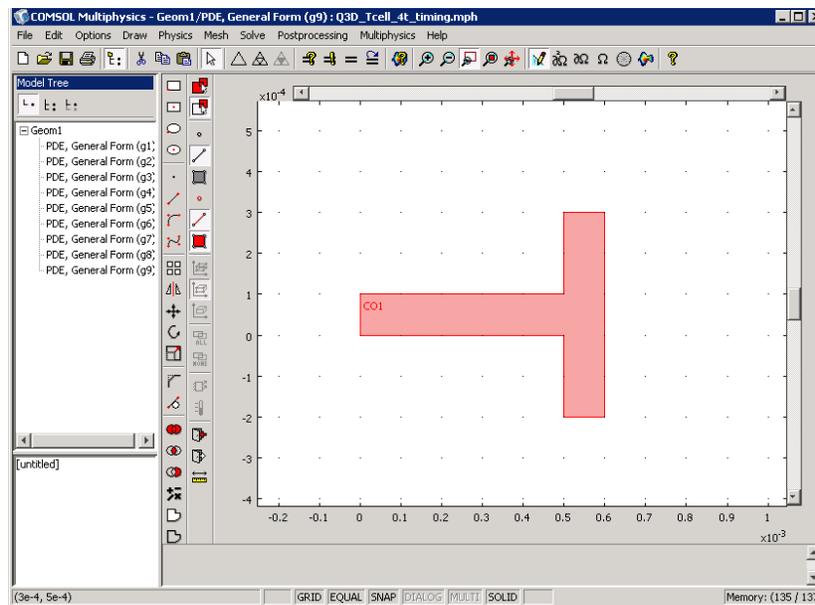
Figure B.4: Computational geometry is drawn by built-in CAD tools

Physics settings: Subdomain

1) Choose the first *PDE, General Form* from *Multiphysics* menu.

2) From the *Physics* menu choose *Subdomain Settings* to launch the *Subdomain Settings* dialog box.

3) Select *Subdomain 1*. There may be more than one subdomain depending on the drawing mode of the geometry.

4) Extract *Flux vector* and *Source term* from PDE 1 and insert them in the corresponding fields.
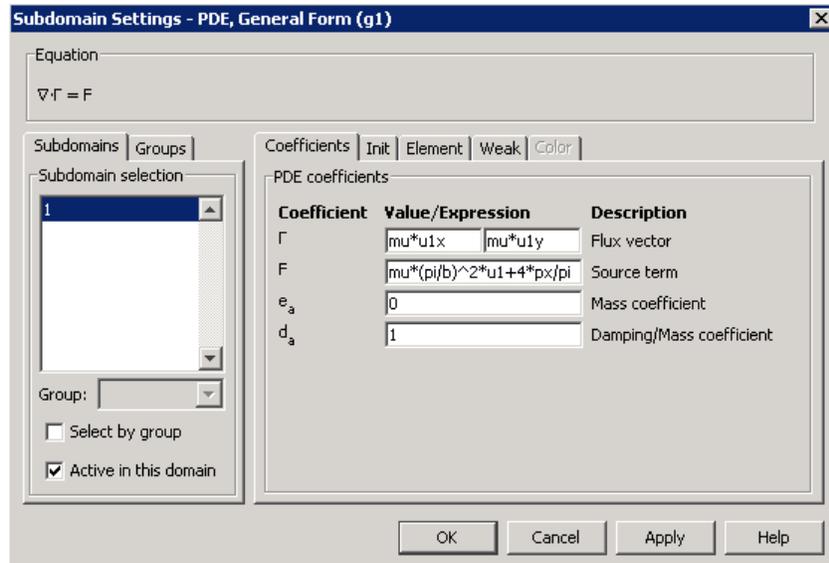
Figure B.5: Subdomain Settings dialog box

5) Depending on the solver settings, you might need to enter an initial value of the depending variable of this PDE in the *init* tab of the *Subdomain Settings* dialog box. For low Reynolds number flow problem often a simple constant value is sufficient.

6) Click OK.

7) Select the next *PDE, General form* from the *Multiphysics* menu. Follow the steps from 2-6. Repeat steps 2-6 for every other *PDE, General form* entry in the *Multiphysics* menu.

Physics settings: Boundary conditions

1) Depending on the variable of the selected PDE and the boundary, the boundary
   conditions fall into one of the following three cases: no-slip (flow speed),
   constant value or expression (flow speed, pressure) or unknown (flow speed,
   pressure). For the first two cases *Dirichlet boundary condition* is selected and
   corresponding *coefficient value/expression* are entered. For example, in
   boundary 1, a constant value is set for the pressure variable (Shown in Figure
   B.6) by selecting *Dirichlet boundary condition* and setting the coefficient *R* to
   $-p+1$.
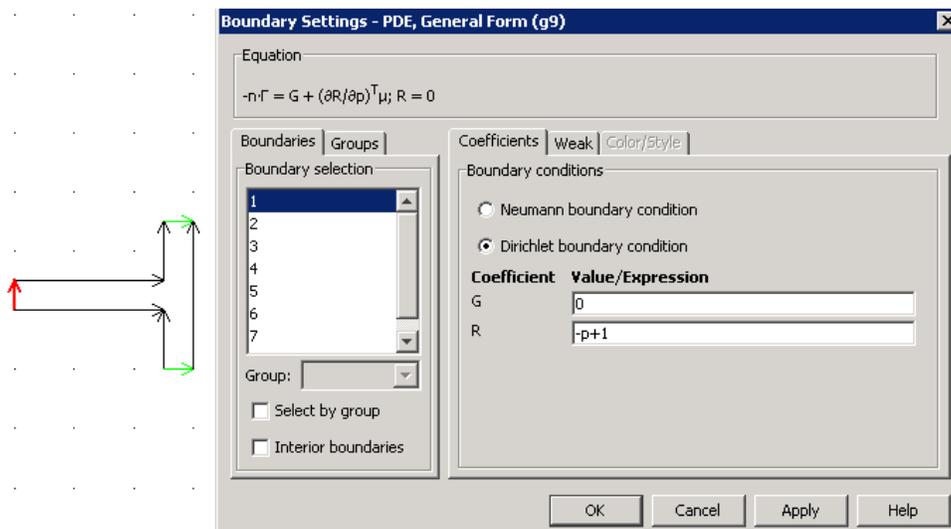
Figure B.6: Setting up Dirichlet boundary condition for pressure on boundary 1

2) For all other variables and boundaries, corresponding *PDE, General form* is
   selected from the *Multiphysics* menu and appropriate boundary conditions are
   set following the rules mentioned in step 1.

Mesh generation:

Navier-Stokes equations are computationally difficult, so it is important to use an appropriate mesh. If the mesh is too coarse, the solution might not converge, or error might be large if converged. Conversely, if the mesh is too fine, the solution time for the nonlinear system of equations might be unnecessary long. There are many ways to generate mesh for the computational geometry. The most commonly used technique of using the free mesh parameter is described here.

1) From the *mesh* menu choose *free mesh parameters*.

2) In the *Free Mesh Parameters* dialog box, select the *Boundary* tab.

3) Select all the boundaries and specify the *Maximum element size* and *Element growth rate* (example shown in Figure B.7).
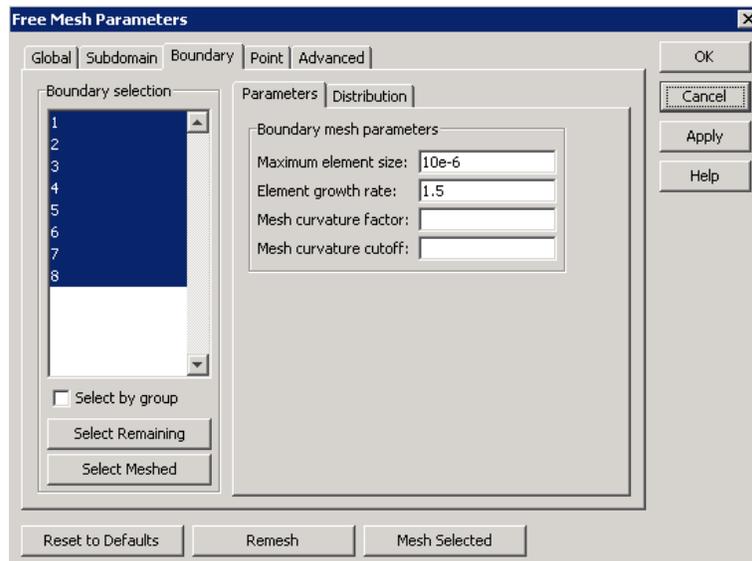
Figure B.7: Setting up Free Mesh Parameters

4) Click Remesh and then OK.

Solver settings:

1) From the *Solve* menu, select *Solver Parameters*.

2) Select the *Stationary* from the Solver list.

3) In the *General* tab, select a direct solver first (e.g. *Direct (UMFPACK)*)

4) Also select the appropriate *tolerance* conditions and other settings specific to

   the solver type.

5) If this specific solver cannot solve because of memory limitation, select some

   indirect solver that would require less memory but longer time to solve the

   problem.

Solving the problem:

Click the *Solve* button on the main toolbar to start the simulation. The progress of

simulation will be displayed on a status window.

Postprocessing and Visualization:

The default visualization displays the dependent variable of the first PDE. For

customized visualization, choose *Plot Parameters/Cross-Section Plot

Parameters/Domain Plot Parameters* etc from the *Postprocessing* menu for a

range of different options of visualization and variables plots.
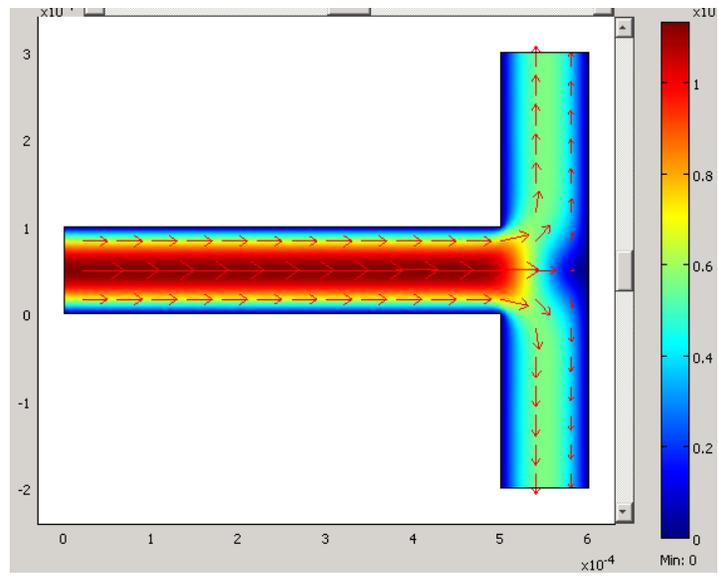
Figure B.8: Surface and Arrow plots of the velocity fields